Performance modeling of Power Recovery Turbines with combined 1D - CFD methods

Girish Venkatachalapathy

Master of Science Thesis

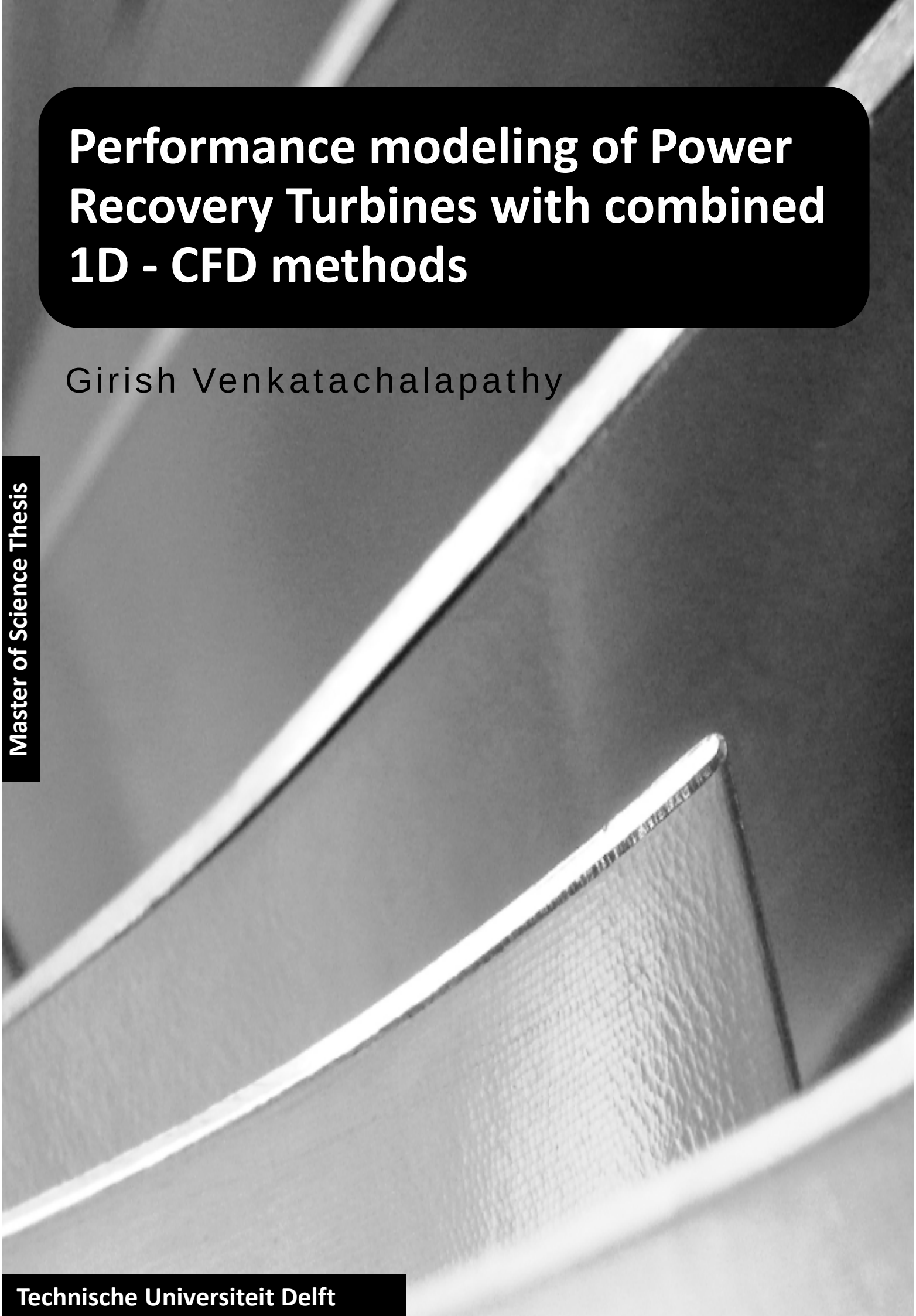

Technische Universiteit Delft

Performance modeling of Power Recovery Turbines with combined 1D-CFD methods

MASTER OF SCIENCE THESIS

to obtain the degree of Master of Science
at Delft University of Technology

Girish Venkatachalapathy

November 18, 2016

Supervisors : Prof. dr. ir. Sikke Klein, TU Delft
Ir. M.S. van der Schoot, Flowserve

Committee : Dr. ir. Rene Pecnik, TU Delft
Dr. ir. M.J.B.M. Pourquie, TU Delft
Ir. G. J. Otero Rodriguez, TU Delft

Department of Process & Energy,
Faculty of Mechanical, Maritime and Materials Engineering.

Delft University of Technology
Department of Process and Energy

The undersigned hereby certify that they have read and recommend to the Faculty of Mechanical, Maritime and Materials Engineering (3mE), for acceptance of the Master Thesis entitled

Performance Analysis of Power Recovery Turbines with combined 1D-CFD Modeling

by

Girish Venkatachalapathy

in partial fulfillment of the requirements for the degree of

Master of Science in Mechanical Engineering

Dated : November 18, 2016

Supervisors :

_____

Prof. dr. ir. Sikke Klein

_____

Ir. M.S. van der Schoot (Flowserve)

Committee :

_____

Dr. ir. Rene Pecnik

_____

Dr. ir. M.J.B.M. Pourquie

_____

Ir. G. J. Otero Rodriguez

Abstract

Industrial practices are beginning to place a strong emphasis on reusable energy. Conventional turbines, which have been traditionally used for recovering energy from fluids, have disadvantages of large sizes and high overhead costs. Hence, research is being done on alternatives that have similar capabilities. Power Recovery Turbines (PRTs) are an interesting concept of reverse running pumps that can provide energy-recuperation benefits.

This thesis is focused on the application of PRTs in the process industry. Centrifugal pumps are the most widely used hydraulic turbomachines due to their low cost, small size and easy maintenance. They move fluids for different processes in applications such as hydrocarbon processing and synthetic ammonia manufacturing. The motivation for using PRTs here is that the pressure energy of the pumped fluid is generally wasted or unused after the process, as it is made to pass through a pressure-reducer or a throttle valve. With centrifugal pumps in their PRT mode, the available head or energy of the fluid stream can be recovered downstream of the process with a lower investment compared to a conventional turbine. The power thus obtained could be stored or used to power the pump itself, reducing energy costs and consumption. Thus PRTs prove to be an economical and sustainable solution to energy recovery. It is therefore important to study the performance of the PRT to assess the cost-effectiveness and efficiency of the process, compared to using a conventional turbine.

The objective of this thesis is to derive a one-dimensional model to determine the performance of a multistage PRT. The performance curves are estimated from the input parameters, which are the PRT geometry, the fluid properties, the flow rate and the shaft rotation speed. The curves would determine the performance of the PRT over a range of flow rates. Each stage of a multistage PRT contains a crossover, volute and a runner. 1D sub-models are derived for each of these components, within a single stage. But 1D methods are not sufficient to represent the diverse 3D flow phenomena across the PRT domain. Hence CFD simulations are used to represent such complicated flow regions. They are combined with the results from the 1D sub-models for the performance estimation of a single stage. The challenge in modeling multistage pumps is that there are a lot of leak flows between the components. Hence, analytical iterative schemes are used to estimate the leaks, as they have a significant impact on the performance. The stage 1D models along with the leak flows, are put together for the multiple stages to complete the 1D tool for predicting the PRT performance. The results obtained from the tool are validated against the test results.

The 1D tool gives a good estimate of the PRT performance curves, from available input conditions. The results in 1D are well within 7-8% of the test results, and prove to be a simple and effective tool to be used for further research. Since the cost and time involved in testing a PRT are high, it would be beneficial to derive the performance of the PRT from known pump performance. So a brief attempt has also been made to derive empirical relations between pump and PRT performance parameters.

Girish Venkatachalapathy

Acknowledgements

Firstly, I would like to express my sincere gratitude to my supervisor, Prof.Dr.ir.Sikke Klein, for his constant support and motivation in this thesis work, during the writing of this thesis. His cooperation in the numerous administrative activities, from getting things in place, guiding me with his ideas and supervision, to the funny interactions with him are really invaluable, and it has been a memorable experience.

My sincere thanks goes to Ir.Martijn van der Schoot, for providing me the opportunity to join their team at Flowserve as a thesis student. His patient support as supervisor, was invaluable through the period of the thesis work. I have learnt a thing or two from his composure and way of guidance.

I would like to thank Ir.Gustavo, who was there whenever I needed assistance with the concepts, and for patiently correcting and commenting on my thesis. I also extend my thanks to Kevin Bruurs, from Flowserve, for his support and time, in the discussion of my methods, results and the report writing.

I would like to thank the rest of my thesis committee: Prof.Rene Pecnik, and Dr.Mathieu Pourquie, for their time in evaluating my thesis and giving me critical and useful comments.

Last but not the least, I would like to thank my parents and family, for their financial assistance in keeping me going, in successfully finishing my course. And of course, the biggest of thanks to my dear friends, who have kept me spirited and engaged, in running this lap of my Masters, as my family away from home !

Contents

List of Figures

List of Tables

List of Symbols

$\bar{r}$	Non dimensional radius	-
Δz	Elevation Head	m
δ_R	Thickness of rotor boundary layer	m
δ_S	Thickness of stator boundary layer	m
$\dot{m}$	Mass flow	$m^3 s^{-1}$
ϵ/D	Relative roughness	-
η_{ht}	Hydraulic Efficiency	-
η_{mt}	Mechanical Efficiency	-
η_t	Overall Efficiency	-
η_{vt}	Volumetric Efficiency	-
λ_R	Resistance coefficient of the rotor	-
λ_S	Resistance coefficient of the stator	-
λ_{seal}	Friction coefficient of axial seal	-
ν	Kinematic viscosity of the fluid	$m^2 s^{-1}$
Ω	Speed of runner	rpm
Ω_s	Specific Speed	-
Φ	Flow Coefficient	-
Ψ	Head Coefficient	-
ρ	Density of fluid	$\mathrm{kg\,m^{-3}}$
τ	Torque	N m
θ	Angle of bend	deg
φ_g	Dimensionless leak flow rate	-
A	Area of cross-section	$\mathrm{m^2}$
C	Absolute Velocity	$\mathrm{m\,s^{-1}}$
C_d	Discharge coefficient	-
C_m	Meridional velocity	$\mathrm{m\,s^{-1}}$
C_u	Tangential velocity	$\mathrm{m\,s^{-1}}$
C_z	Velocity in z direction(axial)	$\mathrm{m\,s^{-1}}$
C_{rf}	Radial velocity across side chamber	$\mathrm{m\,s^{-1}}$
C_{uf}	Tangential velocity across side chamber	$\mathrm{m\,s^{-1}}$

C_{uth}	Absolute velocity at the end of throat	$\mathrm{m\,s^{-1}}$
D	Diameter of runner	m
D_e	Effective cross-section diameter	m
D_h	Equivalent Diameter	m
e	Thickness of cutwater	m
f_s	Moody friction factor	-
g	Acceleration due to gravity	$\mathrm{m\,s^{-2}}$
H	Head	m
h	Enthalpy	J
h_0	Total Enthalpy	J
H_E	Euler Head	m
H_{3V}	Head drop across the 3-vane stage	m
H_{5V}	Head drop across the 5-vane stage	m
H_{curv}	Head drop across curved sections	m
H_L	Head drop across the last stage	m
H_{nozz}	Head drop across nozzle-like sections	m
$H_{sc,inlet}$	Side chamber inlet head loss	m
H_{seal}	Axial seal head loss	m
H_{set1}	Head drop across stages 1-5	m
H_{set2}	Head drop across stages 6-11, and the last stage	m
k_b	Bend loss coefficient	-
k_e	Entrance loss coefficient	-
k_f	Core rotation coefficient	-
k_{ens}	Seal entry friction coefficient	-
k_{exs}	Seal exit friction coefficient	-
k_{f0}	Entrance rotation coefficient	-
l_1	Side chamber entry gap	m
L_s	Length of the seal	m
P	Perimeter of section	m
p	Static Pressure	Pa
p_0	Total Pressure	Pa
P_p	Power delivered by the fluid	W
P_{fluid}	Power delivered by fluid	W
P_{runner}	Power from runner	W

P_{shaft}	Power from shaft	W
Q	Total Flow Rate through PRT	$m^3 s^{-1}$
q_f	Leak flow through side chamber and wear-ring	$m^3 s^{-1}$
Q_{runner}	Actual flow through runner	$m^3 s^{-1}$
r	Radius of runner	m
R_b	Radius of bend	m
r_z	Volute inner radius	m
r_{wf}	Radius of wear ring	m
$r_{z,eff}$	Effective throat radius	m
Re	Reynolds number	-
Re_ϕ	Circumferential Reynolds number	-
Re_Ω	Rotational Reynolds number	-
Re_{ax}	Axial Reynolds number	-
s	Seal clearance	m
t_f	Axial side chamber width	m
TDH	Total Differential Head	m
U	Velocity of runner	$m\,s^{-1}$
u	Mean velocity of flow	$m\,s^{-1}$
u_τ	Friction velocity	$m\,s^{-1}$
V_s	Axial velocity through seal	$m\,s^{-1}$
V_{sc}	Side chamber inlet velocity	$m\,s^{-1}$
W	Relative velocity	$m\,s^{-1}$
W_{shaft}	Specific work from shaft	$W\,s\,m^{-3}$
Z	Number of rotor vanes	-
z	Elevation	m

1

Introduction

The fast accelerating energy consumption defines today's global scenario. To meet the growing energy demands, the world is on the lookout for promising, alternative solutions. Renewability and reusability of resources are being looked upon more and more every day in energy research. Customers are also moving towards greener and more sustainable forms of energy installments. One among these sustainable methods is energy recovery. It can be explained as the reduction of the input energy given to a system by exchanging the energy produced by one sub-system within the entire system with another. Energy recovery applies to a wide range of systems that are used to create mechanical power, electricity, heat etc., When energy recovery is applied to mechanical systems that consume and produce power, it is known as power recovery.

1.1. Hydraulic Power Recovery

The concept of power recovery attracted interest in hydro power 50 years ago, when several pump manufacturers and energy economists, through experiments, systematically investigated the possibilities of using centrifugal pumps as turbine generators [1]. Since then, the high head produced in the water pumping systems and hydraulic turbomachines are being monitored closely and methods of energy recovery are being investigated.

A Hydraulic Power Recovery Turbine (HPRT), is a device designed for the space effective, on-site transfer of liquid, such that it can operate in two modes, as a pump and a turbine. HPRTs can be either pumps running in reverse or the special types such as Francis (radial inflow - axial outflow) or Kaplan Turbines (axial in and outflow).

Centrifugal pumps are one of the most commonly used hydraulic machines. They are used in liquid transportation, heating and cooling systems, and are easily available at all places. They have a wide operating head range of $3-2300m$ [2] with low viscous liquids. The maintenance and installation costs of centrifugal pumps are lower compared to other rotary pumps used in the same range of operation. Hence, a reverse mode operation of a centrifugal pump is an effective and economical way of power recovery.

Advantages of Pumps as Turbines

- Pumps are more flexible in construction and are less complex than conventional turbine constructions.
- Small size, space effective less capital costs.
- Ready availability of spare parts and shorter production lead times than conventional turbines.
- Attainability of high efficiencies, similar to conventional turbines.

Centrifugal pumps are used to move fluid for a wide range of applications. In their turbine mode (referred to as PRT), centrifugal pumps are used in hydropower storage, for two-way operation and in the process industry, to extract or recover energy from the pressurized fluids used for the various processes. In the process industry, the pressure energy of the pumped fluid is generally wasted or unused after the process, by making it flow through a pressure-reducer or a throttle valve. In places where the energy is recovered, it is done using conventional turbines. Using PRTs, the available head or energy of the fluid stream, can be recovered downstream of the process, with a lower investment compared to a conventional turbine. The power thus obtained could be stored, or used to power the pump itself, reducing energy costs and consumption. The PRTs find their application in areas such as hydrocarbon processing, scrubbing of natural gas, synthetic ammonia manufacturing and also in reverse osmosis desalination plants. It is therefore important to study the performance of the PRT, to assess the cost-effectiveness and efficiency of the process compared to using a conventional turbine.

Computational Fluid Dynamics in Turbomachinery

Computational Fluid Dynamics (CFD) is a powerful tool to study and analyze complex flow phenomena. Turbomachinery is one of the most complicated fields for analysis, due to the complex 3D flows existing in the system. CFD facilitates the research process as a very promising tool to study turbomachines. In the pump industry, it is used effectively in the prediction of part load performance, cavitation behavior etc., It provides us with a deeper insight and understanding of the fluid flow, which would aid the modifications in the design and optimization processes.

1.2. Motivation

With increasing energy awareness, customers nowadays, prefer more energy-effective setups and installments. Hence the pump industry is giving importance to research on the reverse mode operation of the centrifugal pump. The thesis has been written in collaboration with Flowserve, Etten Leur, The Netherlands. Flowserve is a global industrial leader in manufacturing pumps, mechanical seals and valves. The Etten-Leur division builds, develops, designs, manufactures and tests high pressure, high energy low-specific speed multistage pumps for the chemical, energy, and oil and gas market. The manufacturing is driven by customer requirements and specifications. Flowserve also concentrates on building PRTs for its customers. A typical multistage pump is shown in figure 1.1.

When recovery methods gained interests in using centrifugal pumps as turbines 50 years ago, investigations were only experimental, yielding empirical relations between the two modes of operation. Several researchers have performed experimental studies to analyze pumps working in the reverse mode. These empirical relations were based on the pump efficiency and specific speed [4], which will be discussed in chapter

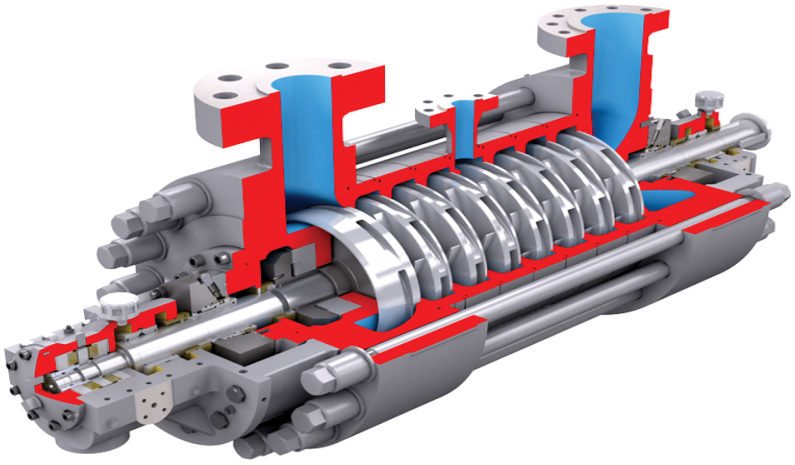

Figure 1.1: Model of a multistage pump [3]

2. Nelik and Cooper [5] performed experiments on the reverse mode operation of a low specific speed two-stage pump and compared the performance with that of a conventional radial turbine. They found that the working of a pump as a turbine is better than a turbine running in reverse mode as a pump. Gopalakrishnan [6] derives empirical relations between the pump and turbine mode of operation based on operational test data. Based on empirical relations from Stepanoff [7], he compares the head per stage and the efficiencies of the pump and the turbine modes, for different specific speeds. He states that empirical prediction of turbine mode performance from known pump mode performance can lead to significant errors. He also highlights the effect of gas evolution on the performance, verified from experiments, though it is beyond the scope of this thesis. After some incomplete attempts by researchers to find a theoretical background to these empirical relations, Baines et.al [1] first performed preliminary CFD simulations on single stage machine in two modes. They were able to compare both a turbine working as a pump, and the reverse. They were able to prove through CFD that the working of a turbine as a pump is indeed more challenging, than making a pump work as a turbine. This is because, the diffusing flow through a pump, might separate and stall more than the accelerating flow happening in a turbine. This was well in accordance with the conclusions of Nelik and Cooper [5]. Baines et.al also compared the results from CFD with the experiments, considering only the leak flows that happened through the wear-rings. Nautiyal et.al [4] performed experiments on a single stage centrifugal pump, to derive the correlation between the pump and the turbine mode. The focus of this thesis is the development of a one-dimensional model for the performance prediction of the multistage PRT. This involves estimating the runner performance based on existing 1D methods, and comprehensively predicting the leak flows in rotor-stator cavities, along with the wear-rings.

1.3. Objective and Outline

The objective of this study is to investigate and develop a one-dimensional tool, which would predict the performance of a multistage PRT, from the available pump geometry information, fluid properties and flow input parameters. Since the flow through the PRT cannot be modeled exclusively using 1D methods, CFD simulations are used to represent the complicated flow regions, characterized by 3D flow phenomena. Thereby, we aim to derive the overall performance curves which are conventional ways of representing the

hydromachine performance in the pump industry. The results of the PRT model are validated against the test results obtained from Flowserve.

The thesis is structured as follows :

Chapter 2 presents the theoretical background and the concepts that have been used sequentially in developing the 1D model.

Chapter 3 describes the setup and the settings of the CFD simulations that have been performed. Details about the mesh sensitivity and grid independence, and the test results against which the results are validated, are also discussed here.

Chapter 4 discusses the results that have been obtained from the 1D model and the CFD simulations for the different configurations of the setup. The methodology of the analytical schemes used as part of the 1D model are also explained.

Chapter 5 contains the results of the combined 1D-CFD model, their validation against the test results, and the discussion of the final results.

Chapter 6 summarizes the conclusions of the thesis work and recommendations for future work.

2

Theoretical Background

Power Recovery Turbines (PRTs) in hydraulic pumping applications are the reversed pumps, which provide energy-recuperation benefits, when used as turbines [8]. In areas where large amounts of energy is lost in throttling devices and valves, PRTs find their place. Centrifugal pumps add continuous energy to the flow. When operated in reverse, a single stage of the pump behaves like a radial turbine stage.

This chapter throws light on the setup of a PRT, its performance estimation, and the theoretical background to this thesis work. Section 2.1 explains about the components in a PRT and how the working differs from that of the pump. In Section 2.2, the non-dimensional numbers and the parameters that determine the performance of a PRT are discussed. Section 2.3 elaborates on the theoretical aspects and the governing equations for the study of the flow in a PRT. The methodology to estimate the crossover flow, the interface, runner, and leak flow is discussed in the remaining sections of this chapter.

2.1. Components of a PRT

Centrifugal pumps are machines that are driven by a motor. The pumps increase the pressure energy of the fluid for a process. The PRT is used to extract energy from the fluid, that is coming out of the process. The pumped fluid is passed through a PRT, thereby rotating the runner ('impeller' in pump configuration). The pressure energy of the fluid is thus converted into kinetic energy to rotate the shaft, which thereby supplies load to the motor or generator. A clutch and gearbox arrangement is generally used to couple the PRT to the motor. A typical example of where a PRT is placed in an industrial application is shown in figure 2.1.

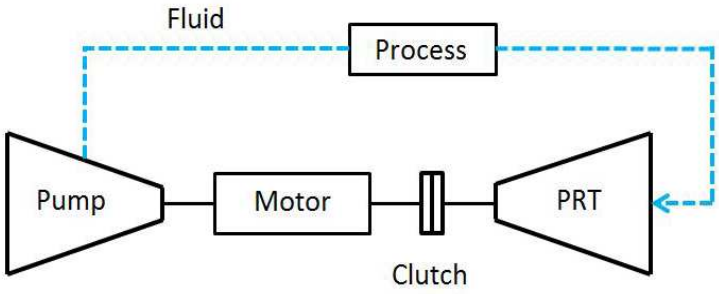

Figure 2.1: Flow Setup - PRT Installation

The PRT studied in this thesis is the turbine mode of a multistage volute centrifugal pump whose construction is discussed further in this chapter. The multistage pump is made up of two series stages, each containing 5 or 6 individual stages. For a single stage, the inflow is in the axial direction. The fluid that is taken through the crossover, enters the runner in the radial and tangential direction through the volute. The flow exits the runner axially, and is passed to the next stage. A simple configuration of the PRT is shown in Figure 2.2.

2.1.1. Runner

The impeller of a centrifugal pump, termed as the runner in the turbine mode [8], has a radial inflow into it. Radial impellers in a pump are generally used when a high head is to be developed at relatively low flow rates. The runners are generally classified into open and enclosed types. The enclosed types consist of a hub and a shroud, within which the runner vanes are placed. The runners considered in the multistage pumps in this thesis are all enclosed types. The blades are attached to a hub at the rear, and a shroud at the front, which form the enclosure.

The runner vanes used in the PRTs are backward curved vanes in the pump. In the case of a PRT, the flow impinges on the trailing edge, and the fluid pushes the vane at the original pressure side of a pump vane. The fluid leaves at the leading edge and is carried towards the next stage.

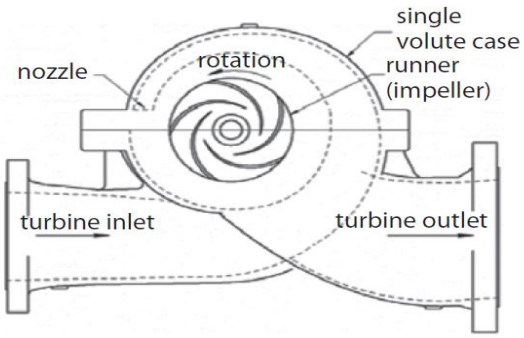

Figure 2.2: PRT - Simple Configuration [8]

2.1.2. Volute

Before entering the runner, the fluid passes through a collector area. This is called the collector, because it collects the fluid, that goes out of the impeller in the pump mode. There are two types of collectors, one is the

volute, and the other, the diffuser. The PRT studied in this thesis is the turbine mode of a multistage volute pump. The volute has an increasing cross-sectional area, which is used to decelerate the flow in the case of a pump. It thereby increases the static pressure of the fluid, as it is led through the crossovers to be passed to the next stage. Hence in a PRT, the flow is accelerated through the volute, thereby decreasing the pressure. The fluid from the crossover is guided into the volute using a tongue or cutwater as shown in figure 2.3. The tongue is an edge which is located at the end of the volute. The design of the tongue plays a very critical role, because it determines the volute inflow velocity as well as the inflow velocity into the runner. The PRTs studied for the thesis are made of twin volutes, which possess the advantage of reducing the radial forces [8]. In a twin volute, as shown in figure 2.3, the flow through each throat is half of the entire flow coming into the PRT. The total throat areas of the two volutes in the twin volute design are generally comparable to the single volute throat area.

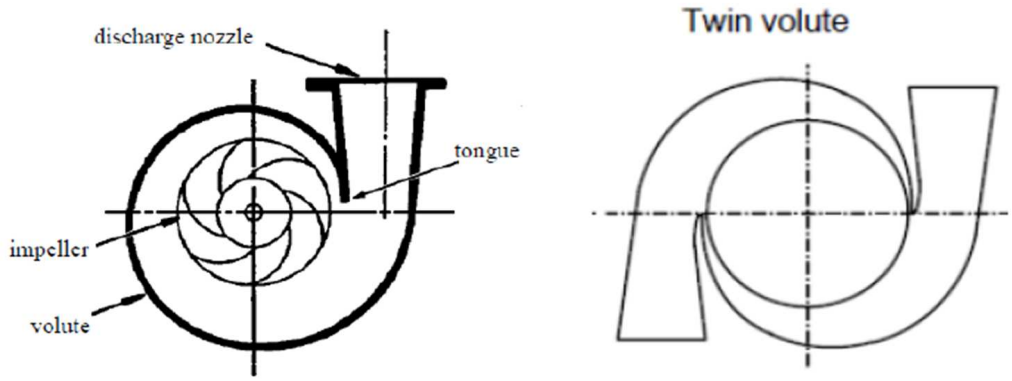

Figure 2.3: Single and Twin Volute configurations

2.1.3. Crossover

The crossover is the section that connects one stage of the pump to the other. The long crossover is used to connect the series stages, when the multistage PRT is made of opposed runners in the two series stages. This will be explained in figure 4.25. The crossover of a PRT in the reversed flow direction is converging and accelerates the fluid.

2.2. Performance Parameters

Similar to pumps, the PRT is designed for rated conditions specified by the customer. The performance of hydraulic turbomachines are determined based on different flow characteristics. These are the flow rate (Q), head (H), power (P) and efficiency (η). The dimensionless numbers are important parameters in turbine analysis for scaling and prototyping, and in deciding the type of turbine based on the application.

2.2.1. Dimensionless Numbers

Dimensional numbers in turbomachinery give the designer preliminary information, as to which would be the best type of machine for a specific application. They also aid in the selection of an optimum speed for a turbine or a pump, and determine the parameters that help to decide the size of the machine [9]. For two similar machines with similar flow conditions, the dimensionless numbers are equal. In both pumps and

turbines, the flow coefficient(Φ) and the head coefficient(Ψ) are used to determine the performance. They are normalized with the rotor blade speed, and can be expressed as,

$$\Phi = \frac{Q}{UD^2(\pi/4)}, \tag{2.1}$$

$$\Psi = \frac{H}{U^2/(2g)}, \tag{2.2}$$

where U is the velocity of the runner in m/s and D is the outer diameter of the runner in m.

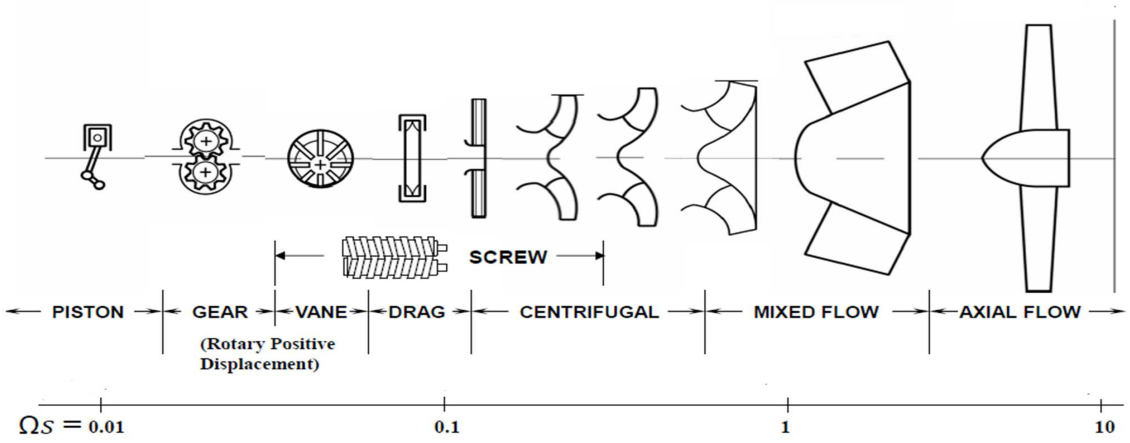

Figure 2.4: PRT - Classification of pumps used as PRTs based on specific speed [10].

Using equations 2.1 and 2.2, the important dimensionless coefficient called the specific speed is derived (Ω_s). It is given as :

$$\Omega_s = \frac{\Omega Q^{1/2}}{(gH)^{3/4}}. \tag{2.3}$$

A pump or a hydraulic turbine designer only obtains preliminary design data such as the head (H), flow rate (Q) and the rotational speed (Ω). The specific speed is an important parameter in selection of a hydraulic turbomachine for a specific type of application, that will provide the highest efficiency at the design condition [11]. It is used to classify different rotor geometry, based on head, flowrate and speed [12]. Figure 2.4 shows the type of turbines, classified based on their specific speed. The dimensionless specific speed, Ω_s of pumps which are studied as PRTs in this thesis are in the range of 0.17-0.25 for every single stage.

2.2.2. Performance Curves

The performance of the Power Recovery Turbines are determined in terms of the head (H) and efficiency(η) plotted against the flow rate(Q). They are shown as characteristic curves for the same rotational speed of the runner. The optimal operating point of the PRT is the Best Efficiency Point(BEP). The BEP is that operating point of the PRT at which the efficiency is the highest. The characteristic curves of a PRT are shown in figure 2.5.

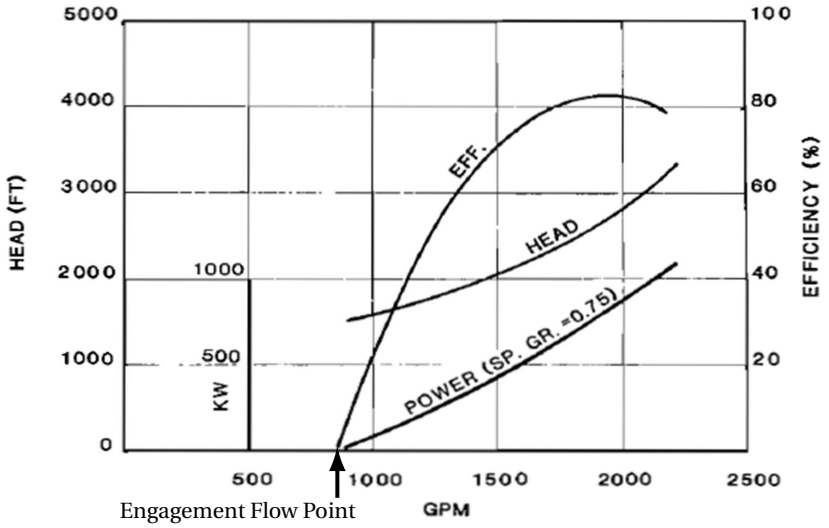

Figure 2.5: Typical Turbine Characteristic Curves [6]

The BEP for the PRT occurs at a higher flow rate than that of the pump mode [6]. The head breakdown is found to be consistently increasing with an increase in flow rate. The efficiency of the PRT shows a similar behavior to that of the pump, except that it flattens out to some extent beyond the BEP. The efficiency is zero at the engagement flow point at which the flow engages the runner into rotation, starting to produce shaft power. This gives the turbine mode a better range of operating points, in case of higher head breakdown requirements, without a major impact on the efficiency. The performance curves are therefore important for easier selection of PRT design based on operating conditions. The time and cost involved with CFD and experiments are high. Due to this, the derivation of a simple 1D model to determine and estimate the performance becomes essential.

2.3. One Dimensional Analysis

The flow exhibited in a PRT is highly unsteady and three dimensional. Though it is impossible to capture the complete 3D effects, simplified 1D methods are always derived to approximate them. This is because the study is always interested in the region around the BEP, and 1D methods predict the performance well, close to the BEP. The one-dimensional flow is based on the assumption that there is only a variation of pressure and velocity in the direction of the flow. This section explains briefly about the steps involved in building the 1D model over the course of this thesis work.

The flow analysis is carried out from the inlet of the PRT to the outlet considering only a single stage initially. The flow paths are the crossover, the runner and the leak paths. The one dimensional analysis is done according to the schematic shown in figure 2.6 in the following sequence:

- Crossover flow modeling using pipe flow equations.
- Modeling of the volute-cutwater region to determine inlet properties to the runner.
- 1D modeling of the runner using velocity triangles and Euler equations.
- Leak flow modeling through the side chambers and axial seals.
- Combining all the models and deriving the performance curves.

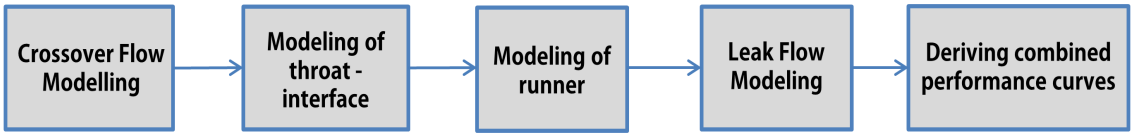

Figure 2.6: Schematic - 1D model

2.3.1. Input and Output Parameters

In the analysis of hydraulic turbomachines, the most important parameters to be analyzed are the head and the efficiency, in terms of which the performance curves are derived. Hence the 1D model is setup, based on the following parameters.

Input Parameters	Flow Rate (m^3/hr), Speed(rpm), Geometry, Fluid Properties
Output Parameters	Head (m), Efficiency(%)

Table 2.1: Parameters for the study

2.3.2. Head of a PRT

The head of a PRT is observed as the height to which the fluid at high pressure can be lowered. It is given in equation 2.4, as the total pressure difference ($\Delta p_0 = p_{0in} - p_{0out}$) between the inlet and the outlet, divided by the density (ρ) and the gravity (g).

$$H = \frac{\Delta p_0}{\rho g} + \Delta z. \tag{2.4}$$

Δz, which is the elevation head, is the difference in elevation between the inlet and the outlet of the PRT. It is neglected in the calculation, because in the horizontal multistage pump analyzed in this thesis, the stages are mounted on the same shaft, and the inlet and the outlet are at the same height from the pump centreline. The total pressure is defined as the sum of the static and the dynamic pressures and is calculated as

$$p_0 = p + \frac{1}{2}\rho C^2, \tag{2.5}$$

where C is the absolute velocity.

2.3.3. Efficiencies

There are different types of losses occurring at various parts of the PRT. The efficiencies associated with these losses are given by :

- Hydraulic efficiency - It is the ratio of the actual head drop across the PRT(H_{actual}) to the ideal head drop(H_{ideal}).

$$\eta_{ht} = \frac{H_{actual}}{H_{ideal}}. \tag{2.6}$$

- Volumetric efficiency - It is obtained by estimating the leak flows occurRing through the side chambers, which will be discussed later. The volumetric efficiencies are calculated for each single stage accounting for the leaks. It is the ratio of the flow rate through the runner impeller(Q_{runner}) to the total flow through the stage(Q).

$$\eta_{vt} = \frac{Q_{runner}}{Q}. \tag{2.7}$$

- Mechanical efficiency - It determines the effect of the mechanical components such as bearings, seals etc., It is the ratio of the power from the shaft(P_{shaft}) to the power from the runner(P_{runner}).

$$\eta_{mt} = \frac{P_{shaft}}{P_{runner}}. \tag{2.8}$$

- Overall efficiency

$$\eta_t = \frac{P_{shaft}}{P_{fluid}} = \eta_{ht} \times \eta_{vt} \times \eta_{mt}, \tag{2.9}$$

where P_{fluid} is the power delivered by the fluid.

2.4. Crossover Flow Modeling

The crossover connects the outflow from one runner to the runner in the next stage. This section highlights the methods that have been adopted for predicting the behavior of the flows in the crossover sections. The flow through the crossover has been modeled using the governing equations for flow through curved pipes and nozzles considering the converging sections, and also combining them with known relations from literature [13]. The idea behind modeling the crossover was to emulate the existing geometry by dividing the entire domain into simpler sections and represent them with suitable models. The eventual model for the entire crossover would be a linear combination of all the simpler models. Hence the crossover geometry is modeled by the curved pipe and nozzle equations. The methodology has been discussed here along with the reasoning and the considerations, while the results and the behavior of these flows will be discussed in the chapter 4.

2.4.1. Flow through curved pipes

The modeling of the curved sections is done based on the pressure drop observed from the results of the CFD, across the section we consider. The head drop for the curved pipe can be expressed as the sum of :

- the head drop due to friction in a straight pipe of equivalent length. It depends on the Reynolds number and the pipe roughness.

- the head drop resulting from losses due to change of direction which depends on the angle of the bend (θ) and the radius of the bend (R_b) [14].

The head drop can be estimated [8] using the equation :

$$H_{curv} = \frac{1}{2g} f_s u^2 \pi \frac{R_b}{D_e} \frac{\theta}{180^\circ} + \frac{1}{2} k_b \rho u^2. \tag{2.10}$$

Here, u is the mean velocity of the flow, obtained from the geometry, $D_e = \frac{1}{2}(r_{out} - r_{in})$ is the tube diameter through which the flow occurs, and k_b, the bend loss coefficients proposed by [15] at various R_b/D_e. f_s is the Moody friction factor in a straight pipe obtained from the Moody diagram [9] or using the Colebrook-White equation for turbulent flow regime, given according to [16] as :

$$\frac{1}{\sqrt{f_s}} = -2\log_{10}\left[\frac{(\epsilon/D)}{3.7} + \frac{2.51}{Re\sqrt{f_s}}\right], \tag{2.11}$$

where ϵ/D is the relative roughness of the surface. The equation is solved iteratively to obtain the friction factor. The solved equation is shown in the form of a Moody chart which is discussed in Appendix B. The loss coefficients and equations also consider the inlet losses which need to be taken into account in pipe flows.

2.4.2. Flow through nozzles

The diffusing section in the case of a pump which characterizes the crossover flow path becomes a converging section in the turbine mode. The fluid is accelerated in these sections. Hence an attempt has been made to model these sections using the 1D nozzle equations. According to this, the head drop across the nozzle-like sections are modeled [17] by:

$$H_{nozz} = k_e \frac{1}{2g}(1-\beta^4)\left(\frac{Q}{C_d A_1}\right)^2. \tag{2.12}$$

where k_e is the entrance loss coefficient based on the geometry, and β is the ratio of the pipe diameters at the two ends of the nozzle section ($\frac{D_1}{D_2}$). C_d is the discharge coefficient [17], which is dimensionless, used to characterize the flow and pressure loss behaviour in fluid systems like nozzles and orifices. It is calculated using the expression,

$$C_d = 0.9965 - 6.53\sqrt{\frac{\beta}{Re}}. \tag{2.13}$$

Re is the Reynolds number for the specified flow calculated using

$$Re = \frac{uD_h}{\nu}, \tag{2.14}$$

where

$$D_h = \frac{4A}{P}, \tag{2.15}$$

is the equivalent diameter calculated for rectangular cross sections, with P as the perimeter of the section.

2.5. Volute Casing Calculation

The fluid entering into the runner from the volute has a swirl component, C_{u2}, which depends on the position and dimensions of the cutwater. The angle of the volute is therefore determined from the hydraulic

drawing, and the velocity components of the fluid are determined from the volute angle. This ultimately leads to the velocity triangles at the inlet of the impeller. This section explains briefly the calculations involved for the volute casing.

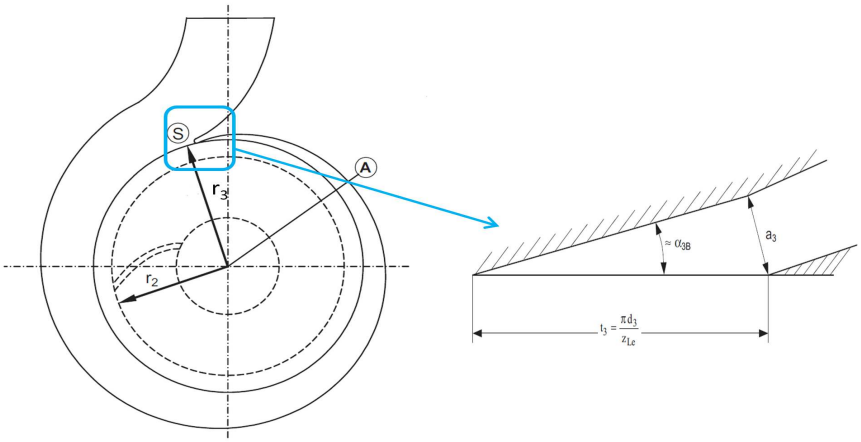

Figure 2.7: Volute Casing [2]

The volute-cutwater angle (α_3) is calculated from the hydraulic drawing. The absolute velocity at the cutwater is calculated as $C_{th} = Q/A_{th}$, where A_{th} is the throat area. The tangential velocity imparted to the flow by the volute is given from figure 2.7 by,

$$C_{uth} = C_{th} cos\alpha_3. \tag{2.16}$$

The casing surface which creates the angle α_3 with the horizontal line (parallel to the pump centreline) is not always straight. It is assumed to be straight, because the angle α_3 is extremely small. Since the fluid coming out of the impeller has a lot of pulsations, the pump has a small gap or clearance between the impeller outer diameter and the cutwater. This clearance has to be taken into account in our calculations for the runner inlet conditions. Figure 2.7 shows the clearance between the runner outlet diameter, r_2 and the inner radius of the volute, r_3 . We calculate an effective radius given by,

$$r_{z,eff} = r_z + e + (k_t \times a_3), \tag{2.17}$$

where a_3 is the height of the throat and $r_z = r_3$. $k_t = 0.25$ is an empirical factor [2] and e is the thickness of the cutwater obtained from the dimensional diagram. The tangential velocity component at the interface can therefore be calculated as,

$$C_{u2} = \frac{C_{uth} r_{z,eff}}{r_2}. \tag{2.18}$$

The meridional component of the velocity of the fluid going into the runner can be calculated as,

$$C_{m2} = \frac{Q}{A_2}. \tag{2.19}$$

A_2 is the area at the inlet of the runner given as,

$$A_2 = \left(\pi D_2 - \left(\frac{z \times t_2}{sin\beta_2}\right)\right) b_2, \tag{2.20}$$

where D_2 is the diameter of the runner inlet, z is the number of blades in the rotor, t_2 is the thickness of each blade, β_2 is the blade angle at the outlet and b_2 is the width of the circular cross section at the inlet. The inlet tangential velocity is also the necessary boundary condition for the leak flow model which will be discussed later.

2.6. Analysis Methods - Runner

A hydraulic turbine creates work by the change of angular momentum of the fluid passing through its rotating vanes. The basic theory of turbomachines involves the velocity triangles to compute the head developed or dropped by the runner. The incompressible Navier-Stokes equations are solved to obtain 1D relations.

2.6.1. Velocity Triangles

Determination of fluid velocity in the vicinity of the runner is complicated since we are dealing with rotating components. Velocity triangles obtained through the one-dimensional flow theory, help understanding the various components of the velocity of the working fluid, at the inlet and outlet of the runner. This one-dimensional flow theory with velocity triangles is based on the assumption that there is only a variation of pressure and velocity along the direction of the flow. Relative velocity $\vec{W}$ is the velocity experienced if we are moving with the fluid. The fluid is moving with an absolute velocity $\vec{C}$. The runnerr is rotating with a peripheral velocity $\vec{U} = \vec{\Omega} \times r$, where r is the radius of the runner at the inlet or the outlet in m, and $\vec{\Omega}$ is the angular rotation of the runner in rad/s. The relation between the velocities is given as,

$$\vec{W} = \vec{C} - \vec{U}. \tag{2.21}$$

In this theory, the relative velocity of the fluid is assumed to be parallel to the blade of the runner. With this, the velocity triangles can be constructed at both the inlet and the outlet. This simple analysis can be used to predict the performance of any turbo-machine.

Figure 2.8 shows the velocity triangles for the PRT runner. Alpha - α is the flow angle and β is the blade angle. The meridional component of the velocity is denoted with subscript m and tangential/peripheral component of the velocity is denoted with subscript u. Subscripts 1 and 2 denote the outlet and the inlet sides of the PRT respectively. The tangential velocities from the velocity triangle, are used to determine the energy transfer between the runner and the fluid, which will be explained in the next section. The meridional velocity (C_m), which is a measure for the flow rate through the runner is obtained as :

$$C_m^2 = \sqrt{C^2 - C_u^2}. \tag{2.22}$$

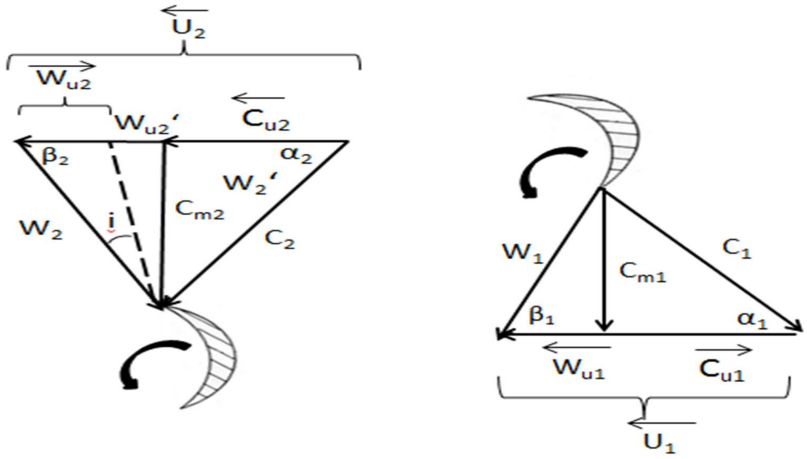

Figure 2.8: Velocity Triangles - PRT

2.6.2. Conservation and Euler Equations

The system is governed by the conservation of mass, momentum and the energy equations applied to selected control volumes. For the runner, the control volume is selected as shown in the figure 2.9. The runner rotates with an angular velocity Ω around a fixed axis. The angular speed is $2980 rpm$ for the PRT under study. The fundamental equations are simplified by assumptions that the fluid is inviscid, adiabatic incompressible and is in steady state.

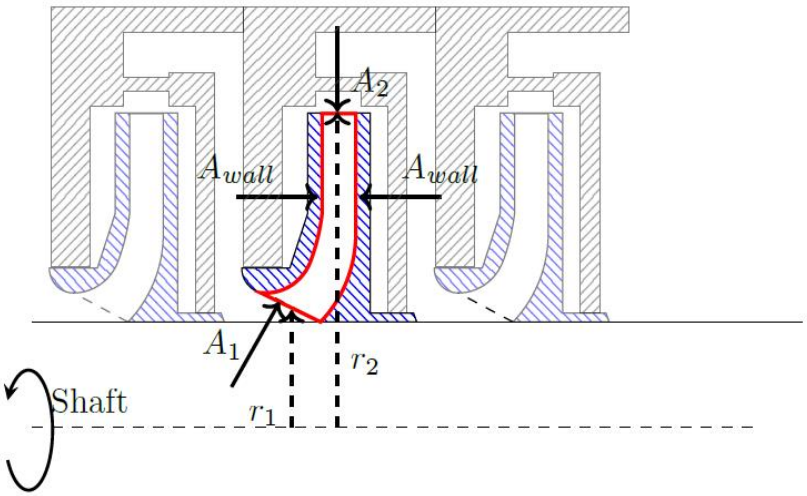

Figure 2.9: Control Volume - Runner Conservation Equations

MASS CONSERVATION

The mass conservation or the continuity equation for a specified control volume is described by the following equation :

$$\frac{\partial}{\partial t}\iiint_V \rho\, dV \quad + \quad \iint_S \rho\vec{C}\cdot\vec{n}\, dS = 0. \tag{2.23}$$

We observe that the flow happens only through the inlet and outlet of the runner, and there is no flow through the wall areas of the hub and the shroud. Hence only the areas $S = A_1, A_2$ are considered for the continuity equation, with $\vec{C}$, the absolute velocity through these areas. Since we assume a steady, incompressible flow, the volume integral term can be neglected and the equation simplifies to :

$$\rho\iint_{A_2}\vec{C}_2\cdot\vec{n}_2\, dA \quad + \quad \rho\iint_{A_1}\vec{C}_1\cdot\vec{n}_1\, dA = 0, \tag{2.24}$$

where $\vec{n}$ is the outward directed unit normal from the area. Since the normals are in opposite directions, it can be seen from Equation 2.24 that the mass flow that enters the runner at the trailing edge is equal to the mass flow that leaves the runner from the leading edge. Hence equation 2.24 simplifies to

$$\dot{m}_1 = \dot{m}_2 = \dot{m}. \tag{2.25}$$

MOMENTUM CONSERVATION

The sum of all the body and the surface forces acting on a system of mass m, along a direction z, is equal to the time rate of change of the total z-momentum of the system [11]. We therefore get steady flow momentum equation as,

$$F_z = (C_{z2} - C_{z1}), \tag{2.26}$$

where F_z is the axial thrust. It is neglected due to its small contribution, compared to the tangential velocity components in the 1D model.

ANGULAR MOMENTUM CONSERVATION

The rate of change of angular momentum experienced by the control volume, plus the outgoing, minus the incoming flow momentum over the surface, is equal to the sum of the the forces which act on the control volume element. Let us assume that the turbine develops a torque denoted by τ. Then the relation of the change in angular momentum between the fluid at the inlet and the outlet can be described using the equation :

$$\tau = \int_{A_1}\rho\vec{C}_1\cdot\vec{n}_1 C_{u1} r_1\, dA \quad + \quad \int_{A_2}\rho\vec{C}_2\cdot\vec{n}_2 C_{u2} r_2\, dA, \tag{2.27}$$

where C_u is the circumferential velocity component of the flow at the different cross sectional areas. As a simplification of the model, we assume that $C_{u1}r_1$ and $C_{u2}r_2$ are constant over the entire cross section at the inlet and the outlet. Equation 2.27 becomes,

$$\tau = C_{u1} r_1 \rho\int_{A_1}\vec{C}_1\cdot\vec{n}_1\, dA \quad + \quad C_{u2} r_2 \rho\int_{A_2}\vec{C}_2\cdot\vec{n}_2\, dA. \tag{2.28}$$

Using equations 2.24 and 2.25, we get

$$\tau = C_{u2} r_2 \dot{m} - C_{u1} r_1 \dot{m}. \tag{2.29}$$

The torque on the shaft, P_{shaft} can be calculated using the expression :

$$P_{shaft} = \Omega\tau = \Omega\dot{m}(C_{u2} r_2 - C_{u1} r_1). \tag{2.30}$$

Since the blade velocity is U=Ω r, we get

$$P_{shaft} = \dot{m}(C_{u2} U_2 - C_{u1} U_1), \tag{2.31}$$

$$W_{shaft} = \frac{P_s}{\dot{m}} = (C_{u2} U_2 - C_{u1} U_1). \tag{2.32}$$

The equation 2.32 is the equation to determine the specific work done on the runner and is called the Euler Turbine equation.

ENERGY CONSERVATION

For the case of a steady, incompressible, adiabatic flow in the control volume which we have considered, the rate of work done on the shaft can be expressed as

$$\dot{W} = P_{shaft} = \int_S (h + \frac{1}{2}C^2 + gz)\rho(\vec{C} \cdot \vec{n})\, dS. \tag{2.33}$$

From equation 2.25 and assuming constant velocities in cross sections, equation 2.33 becomes:

$$\dot{W} = P_{shaft} = (h_2 + \frac{1}{2}{C_2}^2 + gz_2)\dot{m} - (h_1 + \frac{1}{2}{C_1}^2 + gz_1)\dot{m}, \tag{2.34}$$

where $h = e + p/\rho$ is the enthalpy, with e the specific internal energy. Hence the specific work, transferred by the fluid to the blade as in equation 2.32 can be expressed as :

$$W_{shaft} = (h_2 - h_1) + \frac{1}{2}(C_2^2 - C_1^2) + g(z_2 - z_1). \tag{2.35}$$

Since $h_0 = h + \frac{1}{2}C^2$ is the total enthalpy, equation 2.35 becomes

$$W_{shaft} = (h_{02} - h_{01}) + g(z_2 - z_1). \tag{2.36}$$

But we do not consider enthalpy difference in this thesis, and hence the energy difference is not discussed further in the 1D analysis.

The head drop occurring across the runner can be determined by using the Euler turbine equation. It assumes that the fluid is inviscid, adiabatic and isentropic. The velocity profile is assumed to be uniform through the runner and is parallel to the blades. The head drop, obtained through this equation is therefore termed as the Euler Head.

Equation 2.32 is,

$$W_{shaft} = \frac{P_{shaft}}{\dot{m}} = (C_{u2} U_2 - C_{u1} U_1). \tag{2.32}$$

The Euler Head is defined by,

$$H_E = \frac{W_{shaft}}{g} = \frac{C_{u2}u_2 - C_{u1}u_1}{g}. \tag{2.37}$$

The swirl components have a big role to play in the determination of the head drop across the turbine as denoted by the equation. Assuming that the fluid coming out of the runner outlet does not have a swirl component, the Euler Head equation becomes,

$$H_{ideal} = \frac{C_{u2}U_2}{g}. \tag{2.38}$$

is the maximum theoretical head that can be obtained across the runner unless the swirl component acts in the same direction as that of the rotation of the runner. The ideal power is calculated as,

$$P_{ideal} = \rho g Q H_E. \tag{2.39}$$

2.7. Leak Flow Modeling

Estimation of leak flows is a very important part in the performance prediction of PRTs. This is because they have a significant impact on the head drop. In multistage pumps, axial seals are used, to control the leaks from high pressure regions to the stage with lower pressure. The terminology, wear-ring is also used to denote them. They are meant to prevent the leakage of the fluid between the inlet of the impeller and the casing, in the pump mode. But, simple plane axial seals have a small gap or clearance, through which the leak flow happens. There is the side chamber through which the leaked fluid flows before it reaches the seal. The leak flows in a single stage can be explained through the figure 2.10.

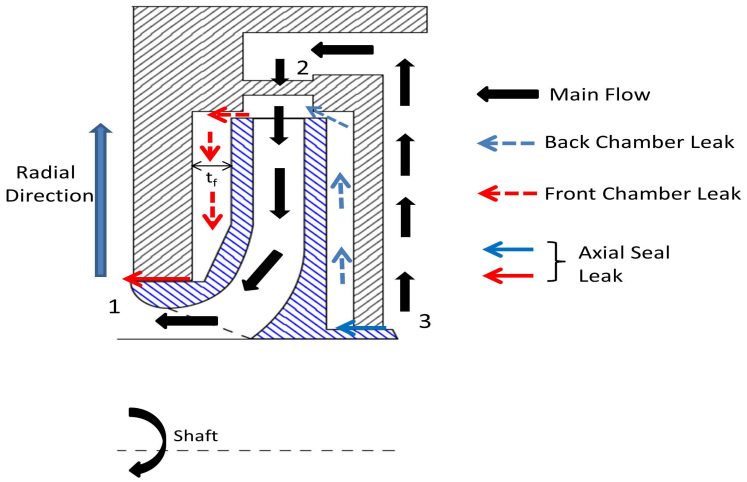

Figure 2.10: Leak flows within a single stage

The leak flows determine the volumetric efficiencies of the PRT. The different types of leaks will be explained in chapter 4. There are two leak flows happening in a single stage of a PRT, the front chamber leak flow indicated by red arrows, and the back chamber leak flow is indicated by blue arrows in figure 2.10. We see from the figure that each leak path consists of a side chamber and a wear-ring The pressure distribution in the side chamber also influences the forces and the axial thrust acting on the runner. The calculation of the leak flow through one chamber is distributed into two parts given as :

- Pressure (or) head drop across the side chamber.
- Pressure (or) head drop across the axial seal.

2.7.1. Side chamber leakage

FLOW BEHAVIOUR

The flow in the side chamber is modeled based on rotor-stator cavity models. Will [18] gives a detailed account of the the work that has been done in rotor-stator cavities. Schultz-Grunow first analyzed the flow caused by a rotating disk in a stationary casing and were able to derive a simple relation that was in good agreement with a simple, laminar Couette flow. Relations were also derived based on the Blasius law of resistance to cavity flow. Batchelor [19] investigated and predicted the occurrence of an inviscid core region between the rotor and the stator with zero radial velocity. Daily and Nece [20] analyzed the rotor-stator cavity flows both analytically and experimentally and they determined the existence of four regimes in the flow depending on the circumferential Reynolds number (Re_ϕ) and the dimensionless gap width G. The four regimes are shown in figure 2.11. Flow regimes III and IV are the most encountered in applications. The model in this thesis is only applicable for regime IV with large Reynolds numbers in the range of 10^6 and a large axial gap width [18].

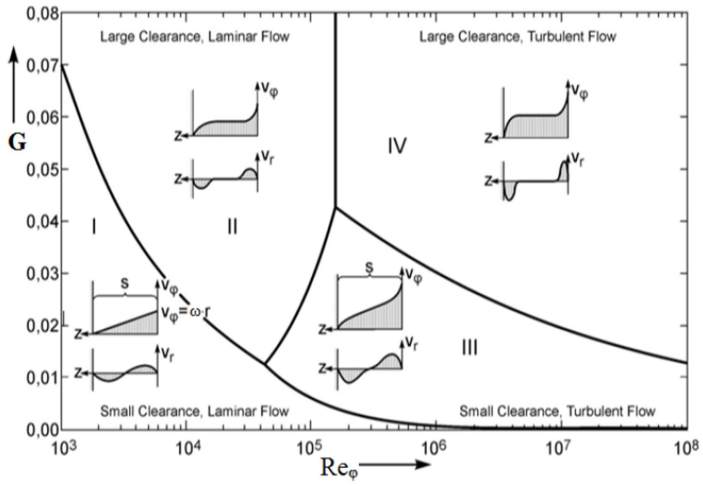

Figure 2.11: Flow Regimes according to Daily and Nece [18]

The viscosity of the fluid in the cavity sets it into motion along with the rotation of the runner. The velocity of the fluid matches the circumferential velocity of the runner at the rotor (runner) side, and is stationary at the stator (casing) side due to the no-slip condition. The velocity of the fluid between the two walls is dependent on the axial gap width(t_f). In rotor-stator cavities with a large axial gap width, a region of intermediate velocity called the 'core region' is established. This circumferential velocity in this region is characterized by the core rotation coefficient or the entrainment coefficient k_f, which is the dimensionless ratio of the angular velocity of the fluid to the angular velocity of the runner. Due to the dominating tangential motion, a radial pressure gradient is established, which is maximum at the outer radius of the cavity. The core region has zero radial velocity, while the fluid close to the stationary casing has zero tangential velocity. Due to this, there is a radial inflow of fluid at the stator side. On the rotor side, there is a radial outflow of fluid due to the centrifugal

forces. The pressure and the centrifugal forces balance each other at the core and are at radial equilibrium. Hence the four regions are formed which are shown in figure 2.12.

In addition to this, due to mass conservation, there is also an axial convection of fluid from the stator side to the rotor side [18]. Though the axial flow might have small velocities, they have a high axially convected angular momentum flux. The circumferential velocity distribution in the core region is important to determine the pressure distribution and the frictional resistances of the rotor. On the rotor side, the frictional resistance offered is determined by the difference of the angular momentum flux between the radial outflow and the axially convected flow into the rotor boundary. The core rotation balances the radial velocity components, and hence can be considered as the equilibrium parameter. The objective of this analysis is to determine the radial evolution of the core rotation coefficient, and thereby the leak flows.

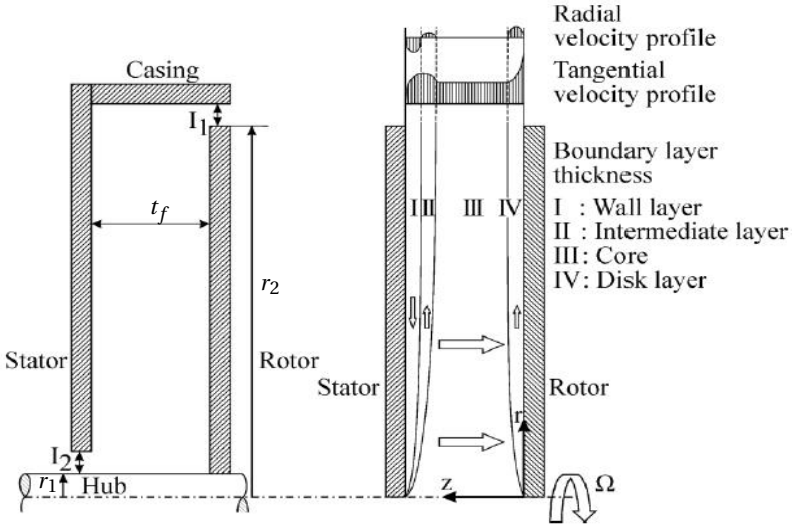

Figure 2.12: Rotor Stator Cavity Flow Outline

GOVERNING EQUATIONS

Will [18] derived the expressions for pressure and core rotation distribution based on the fundamental conservation of mass, momentum and the energy equations. Generally cylindrical coordinates are used to describe the flow in the cavities. As we are considering an incompressible and isothermal flow, the energy equation can be neglected. The Navier-Stokes equations are expressed in cylindrical coordinates considering the geometry. Equation 2.40 is the continuity equation, equations 2.41, 2.42, 2.43 are the radial, tangential and the axial momentum equations respectively.

$$\frac{1}{r}\frac{\partial(r v_r)}{\partial r} + \frac{1}{r}\frac{\partial(v_\varphi)}{\partial \varphi} + \frac{\partial(v_z)}{\partial z} = 0, \tag{2.40}$$

$$\rho\Big(\frac{\partial v_r}{\partial t} + v_r\frac{\partial v_r}{\partial r} + \frac{v_\varphi}{r}\frac{\partial v_r}{\partial \varphi} - \frac{v_\varphi^2}{r} + v_z\frac{\partial v_r}{\partial z}\Big) = f_r - \frac{\partial p}{\partial r} + \frac{1}{r}\frac{\partial(r\tau_{rr})}{\partial r} + \frac{1}{r}\frac{\partial(\tau_{r\varphi})}{\partial \varphi} - \frac{\tau_{\varphi\varphi}}{r} + \frac{\partial(\tau_{rz})}{\partial z}, \tag{2.41}$$

$$\rho\Big(\frac{\partial v_\varphi}{\partial t} + v_r\frac{\partial v_\varphi}{\partial r} + \frac{v_\varphi}{r}\frac{\partial v_\varphi}{\partial \varphi} + \frac{v_r v_\varphi}{r} + v_z\frac{\partial v_\varphi}{\partial z}\Big) = f_\varphi - \frac{1}{r}\frac{\partial p}{\partial \varphi} + \frac{1}{r^2}\frac{\partial}{\partial r}(r^2\tau_{\varphi r}) + \frac{1}{r}\frac{\partial(\tau_{\varphi\varphi})}{\partial \varphi} + \frac{\partial(\tau_{\varphi z})}{\partial z}, \tag{2.42}$$

$$\rho\Big(\frac{\partial v_z}{\partial t}+v_r\frac{\partial v_z}{\partial r}+\frac{v_\varphi}{r}\frac{\partial v_z}{\partial \varphi}+v_z\frac{\partial v_z}{\partial z}\Big)=f_z-\frac{\partial p}{\partial z}+\frac{\partial(\tau_{zr})}{\partial r}+\frac{\tau_{zr}}{r}+\frac{1}{r}\frac{\partial(\tau_{z\varphi})}{\partial \varphi}+\frac{\partial(\tau_{zz})}{\partial z}. \tag{2.43}$$

The following assumptions are made :

- Steady flow conditions, $\frac{\partial}{\partial t}=0$
- Axi-symmetric flow, $\frac{\partial}{\partial \varphi}=0$
- Body forces are disregarded.
- Normal forces due to viscosity $(\tau_{rr},\tau_{\varphi\varphi})$ cancel out. τ_{zz} is small and can be neglected.
- Shear stresses due to the gradient of tangential velocity with radius$(\tau_{\varphi r})$ can be neglected.

The equations are solved only for the mean velocity components, without considering the Reynolds stress terms, to derive a simple calculation method. The equations 2.40 to 2.43 are now simplified based on our assumptions as,

$$\frac{\partial v_r}{\partial r}+\frac{v_r}{r}+\frac{\partial(v_z)}{\partial z}=0, \tag{2.44}$$

$$\rho\Big(v_r\frac{\partial v_r}{\partial r}-\frac{v_\varphi^2}{r}+v_z\frac{\partial v_r}{\partial z}\Big)=-\frac{\partial p}{\partial r}+\frac{\partial(\tau_{rz})}{\partial z}, \tag{2.45}$$

$$\rho\Big(v_r\frac{\partial v_\varphi}{\partial r}+\frac{v_r v_\varphi}{r}+v_z\frac{\partial v_\varphi}{\partial z}\Big)=\frac{\partial(\tau_{\varphi z})}{\partial z}, \tag{2.46}$$

$$\rho\Big(v_r\frac{\partial v_z}{\partial r}+v_z\frac{\partial v_z}{\partial z}\Big)=-\frac{\partial p}{\partial z}+\frac{\tau_{zr}}{r}+\frac{\partial(\tau_{zr})}{\partial r}. \tag{2.47}$$

Neglecting the axial velocity, equation 2.46 can be written as,

$$\rho(v_r\frac{\partial v_\varphi}{\partial r}+\frac{v_r v_\varphi}{r})=0, \tag{2.48}$$

which can be expressed as

$$\frac{v_r}{r}\frac{\partial}{\partial r}(v_\varphi r)=0. \tag{2.49}$$

Since $v_\varphi\neq 0$, there are two possibilites. If $v_r=0$, equation 2.45 becomes,

$$\frac{\partial p}{\partial r}=\rho\frac{v_\varphi^2}{r}. \tag{2.50}$$

Alternatively allowing for a radial velocity, we have $v_\varphi r$ = constant. Hence with an extra term for the radial convection, we get from 2.45,

$$\frac{\partial p}{\partial r}=\rho\Big(\frac{v_\varphi^2}{r}-v_r\frac{\partial v_r}{\partial r}\Big), \tag{2.51}$$

which is the radial evolution of pressure in the side chamber. To analytically model the flow in the side chamber, Will uses the integral boundary layer theory, in which the equations have to be integrated in the axial direction. The general procedure is to integrate across every layer in the axial direction. But in this case, it is simplified and the integral relations are fulfilled only across boundary layer thicknesses δ_S, $\delta_S-\delta_R$, δ_R. This

can be understood from figure 2.13. The radial and tangential momentum equations 2.45, 2.46 are written respectively as,

$$\frac{\partial}{\partial r}(r v_r^2) + r\frac{\partial}{\partial z}(v_r v_z) - v_\varphi^2 = -\frac{r}{\rho}\frac{\partial p}{\partial r} + \frac{r}{\rho}\frac{\partial(\tau_{rz})}{\partial z}, \tag{2.52}$$

$$\frac{\partial}{\partial r}(r^2 v_r v_\varphi) + \frac{\partial}{\partial z}(r^2 v_z v_\varphi) = \frac{r^2}{\rho}\frac{\partial(\tau_{\varphi z})}{\partial z}. \tag{2.53}$$

Using Leibniz rule and accounting for the variation along the axial span from z=0 to z=t_f, equations 2.52 and 2.53 can be written as,

$$\frac{1}{r}\frac{\partial}{\partial r}\left(r\int_{z=0}^{z=t_f} v_r^2 dz\right) - \frac{1}{r}\int_{z=0}^{z=t_f} v_\varphi^2 dz = -\frac{1}{\rho}\int_{z=0}^{z=t_f}\frac{\partial p}{\partial r}dz + \frac{1}{\rho}(\tau_{rzS} - \tau_{rzR}), \tag{2.54}$$

$$\frac{1}{r^2}\frac{\partial}{\partial r}\left(r^2\int_{z=0}^{z=t_f} v_r v_\varphi dz\right) = \frac{1}{\rho}(\tau_{rzS} - \tau_{rzR}), \tag{2.55}$$

where τ_{rzS} and τ_{rzR} are the tangential shear stresses at the stator and the rotor sides respectively. These are the integral momentum equations for a steady, incompressible and axially symmetric flow field.

PRESSURE DISTRIBUTION

The simplified forms of the flow equation are used to derive the pressure distribution based on the dependent parameters. The leak flow, q_f through chamber can be given by the averaged or nominal radial velocity, V_{rf} across the chamber width, t_f as,

$$q_f = 2\pi r t_f C_{rf}. \tag{2.56}$$

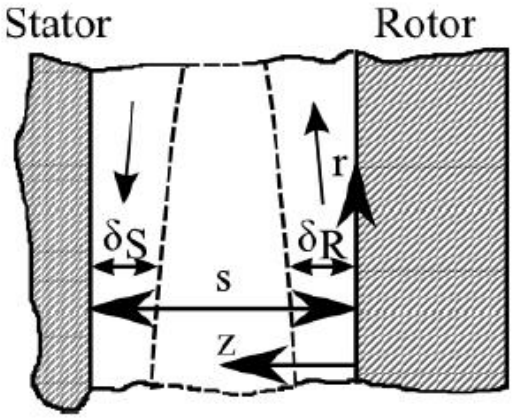

Figure 2.13: Side Chamber Regimes [18]

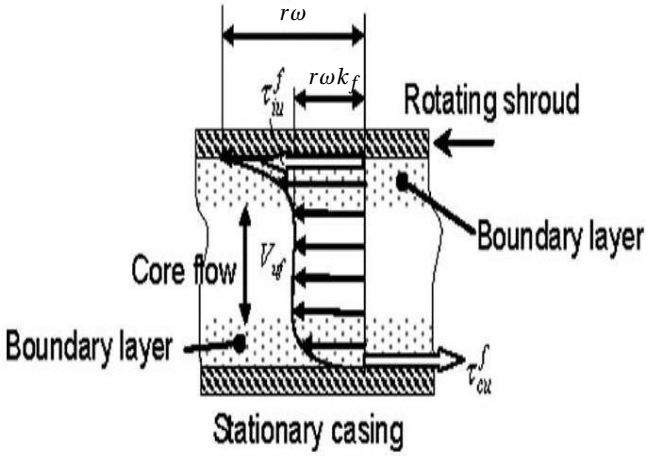

Figure 2.14: Control Volume developed in circumferential direction [21]

Figure 2.14 shows the control volume of the side chamber depicted in the circumferential direction. Neglecting the axial velocity, equation 2.44 becomes $\frac{\partial v_r}{\partial r} = -\frac{v_r}{r}$. Substituting this into equation 2.57, and using $v_\varphi = C_{uf}$ and $v_r = C_{rf}$ we get,

$$\frac{\partial p}{\partial r} = \rho\Big(\frac{C_{uf}^2}{r} + \frac{C_{rf}^2}{r}\Big), \tag{2.57}$$

where C_uf is the tangential velocity of the fluid entering the side chamber. Generally $C_{uf} = C_{u2}$. Using the relation for the core rotation coefficient $k_f = C_{uf}/r\Omega$, and equation 2.56, equation 2.57 can be written as,

$$\frac{\partial p}{\partial r} = \rho r k_f^2 \Omega^2 + \frac{\rho q_f^2}{4\pi^2 t_f^2 r^3}, \tag{2.58}$$

The pressure distribution in the case of no flow through the side chambers (leak flow) is given by,

$$\frac{\partial p}{\partial r} = \rho r k_f^2 \Omega^2. \tag{2.59}$$

We observe that the pressure distribution depends on the leak flow, the gap width, the rotation speed, fluid density and the core rotation coefficient. The methodology to determine the core rotation coefficient is now discussed.

CORE ROTATION DISTRIBUTION

The simplest model for the core rotation coefficient, k_f was given by Stepanoff [15]. He assumed a value of 0.5 to derive the pressure distribution. Will considers according to literature that the circumferential velocity is almost constant in the core region, and there is a significant change at the boundary layers. Hence v_φ could be taken out of the integral sign in equations 2.54 and 2.55. Hence it is assumed that the small distance in the axial direction, which show a change in v_φ can be neglected. The model, therefore has a limitation that it cannot be used in regime 3 as shown in figure 2.11, because the variations are strong when we have a smaller gap width to accomodate high Reynolds' number flows. This gives proof that the model is applicable only to Regime 4, which we encounter in this thesis. From figure 2.13, the integral additivity rule can be written as,

$$\int_{z=t_f}^{z=0} v_r v_\varphi dz = \int_{z=\delta_R}^{z=0} v_r v_\varphi dz + \int_{z=t_f-\delta_s}^{z=\delta_R} v_r v_\varphi dz + \int_{z=t_f}^{t_f-\delta_s} v_r v_\varphi dz. \tag{2.60}$$

The second term becomes zero since there is no radial velocity at the core. The leak flow rate is given as,

$$q_f = 2\pi r \int_{z=0}^{z=t_f} C_{rf}\, dz. \tag{2.61}$$

With equations 2.61 and expanding equation 2.55 with 2π, Will derives the expression for the radial distribution of core rotation as,

$$\frac{dk_f}{d\bar{r}} = \frac{\bar{r}^2}{4\varphi_g}\big(f^*\lambda_S k_f^2 - \lambda_R(1-k_f)^2\big) - \frac{2k_f}{\bar{r}}, \tag{2.62}$$

where λ_S and λ_R denote the resistance coefficients of the stator and the rotor. In such leak flow cases, the outer shroud or casing offers a resistance to the flow. The model does not take into account, the decelerating effect of the radial shroud on the core rotation. f^* is the correction factor for the friction offered by the stationary side and is given by,

$$f^* = 1 + \Big(\frac{t_f}{r_2 + l_1 - r_1} + 5\bar{r}^4 \Big| 1 - \frac{k_f}{0.58} \Big|^{6/5} \Big), \tag{2.63}$$

$\bar{r} = \frac{r}{r_2}$ is the non-dimensional radius, l_1 is the side chamber entry gap as shown in figure 2.12 and φ_g is the dimensionless leak flow rate given by,

$$\varphi_g = \frac{q_f}{\pi \Omega r_2}. \tag{2.64}$$

To determine the resistance coefficients, λ_S and λ_R, Will also found expressions based on the log law for the wall, which need to be solved iteratively.

$$\lambda_S = \frac{1}{\Big(A^* lg\big[2k_f \frac{\delta_S}{r} Re_\phi \sqrt{\lambda_S} \big] \Big)^2}, \tag{2.65}$$

$$\lambda_R = \frac{1}{\Big(A^* lg\Big[2\big(|1 - k_f| \big) \frac{\delta_R}{r} Re_\phi \sqrt{\lambda_R} \Big] - B^* \Big)^2}. \tag{2.66}$$

Here A^* and B^* are constants derived from the friction factor for the pipe flow. δ_S and δ_R are the thicknesses of the stator and the rotor boundary layer respectively, which will be discussed in chapter 4. Re_ϕ is the circumferential Reynolds number given by,

$$Re_\phi = \frac{\Omega r_2^2}{\nu}, \tag{2.67}$$

where ν is the kinematic viscosity of the fluid.

The expression for the core rotation distribution without the friction factor modification has one equation less to be solved iteratively. In this expression, the coupling of the stator and the rotor friction factors is done using an empirical relation. It is given by,

$$\frac{dk_f}{d\bar{r}} = \frac{0.079\bar{r}^{8/5}}{\varphi_g Re_\phi^{1/5}} \Big(\big(\frac{1 - k_{f0}}{k_{f0}} k_f \big)^{7/4} - \big| 1 - k_f \big|^{7/4} \Big) - \frac{2k_f}{\bar{r}} \tag{2.68}$$

A formula for the core rotation was derived by Zilling [16] for an enclosed rotating disk, which is used to calculate k_{f0}, the entrance rotation coefficient.

$$k_{f0} = \frac{1}{1 + \sqrt{\frac{\big(\frac{r_2+l_1}{r_2}\big)^5 - \big(\frac{r_1}{r_2}\big)^5 + 5\big(\frac{t_f}{r_2}\big)\big(\frac{r_2+l_1}{r_2}\big)^4}{1 - \big(\frac{r_1}{r_2}\big)^5 + 5\big(\frac{t_f}{r_2}\big)\big(\frac{r_1}{r_2}\big)^4}}}. \tag{2.69}$$

The detailed methodology of the calculation with results is are explained in chapter 4.

SIDE CHAMBER INLET LOSS

As in normal hydraulic pipes, there is a small head loss, that happens at the inlet to the side chamber. This loss is modeled with the inlet hydraulic loss equation given by,

$$\Delta H_{sc,inlet} = k_{f_{sc}} \frac{V_{sc}^2}{2g}, \tag{2.70}$$

where $k_{f_{sc}}$, the friction coefficient is taken as 0.3 corresponding to hydraulic pipe configurations [8] and the velocity V_{sc} is calculated with the side chamber entry area ($\frac{\pi}{4} {l_1}^2$) from figure 2.12, at the specified flow rate.

2.7.2. Leakage through axial seals

The leakage through an axial seal is modeled based on flow between a stationary and a rotating disk. The flow through the seal is axial. The leak model proposed by Stepanoff [7] incorporates the hydraulic diameter and the length of the axial seal to determine the head loss as,

$$\Delta H_{seal} = \lambda_{seal} \frac{L_s}{2s} \frac{V_s^2}{2g} + (k_{ens} + k_{exs}) \frac{V_s^2}{2g}, \tag{2.71}$$

where L_s is the length of the seal, s is the seal clearance, k_{ens} and k_{exs} are the seal entry and exit friction coefficients respectively.

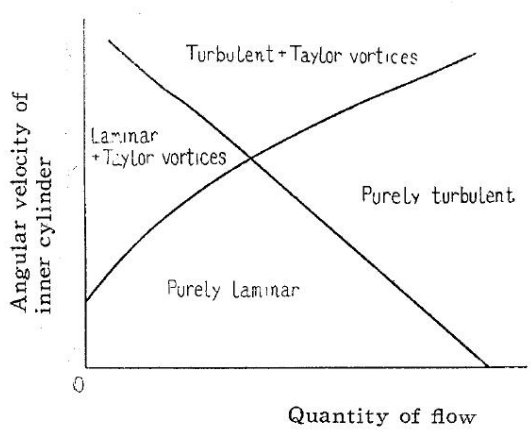

Figure 2.15: Yamada's flow regimes [22]

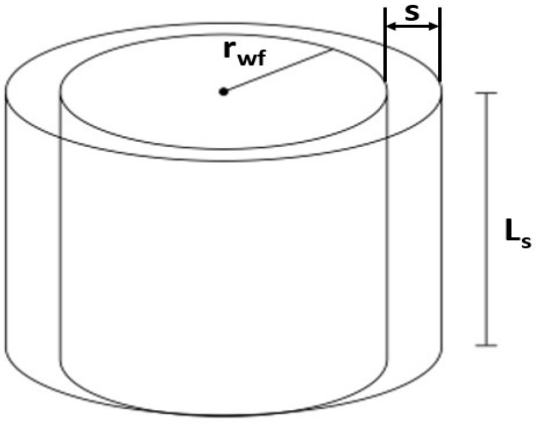

Figure 2.16: Axial Seal dimensions

The dimensions of the axial seal or the wear-ring are denoted in figure 2.16. r_{wf} is the radius of the wear-ring upon which the clearance s causes the leak. The velocity V_s is determined based on the leak flow by,

$$V_s = \frac{q_f}{\pi\left((r_{wf} + s)^2 - r_{wf}^2\right)}. \tag{2.72}$$

Yamada [22] derived a model for determining the leak flow within an annulus between a rotating and a stationary cylinder. He also found four regimes of flow that can happen within a seal which are shown in figure 2.15. He assumes smooth inner walls in deriving an expression for the friction in an axial seal based on Reynolds number of the flow as,

$$\lambda_{seal} = cRe_{ax}^{-\alpha}. \tag{2.73}$$

If velocity profiles according to the classical Blasius law are presumed [23], we arrive upon the relation,

$$\lambda_{seal} = 0.307 Re_{ax}^{-0.24}\left(1+\left(\frac{7}{8}\right)^2\left(\frac{Re_\Omega}{2Re_{ax}}\right)^2\right)^{0.38}, \tag{2.74}$$

depending on the two Reynolds numbers Re_{ax} and Re_Ω. The through flow Reynolds number is expressed as,

$$Re_{ax} = \frac{2V_s s}{\nu}. \tag{2.75}$$

The rotational Reynolds number is given by,

$$Re_\Omega = \frac{2sr_{wf}\Omega}{\nu}. \tag{2.76}$$

3

CFD Modelling and Analysis

In this chapter, the Computational Fluid Dynamic (CFD) modeling and simulations for the working of the PRT are briefly discussed. The setup of the simulations for the different stages of the multistage PRT are explained. The mesh sensitivity study and the convergence criteria used for the simulations have been discussed about. The results from the stage simulations, and the test data against which the results are to be validated are explained.

With pure 1D modeling generally, as discussed in Chapter 2, the unsteady nature, secondary flows, flow separations, and the turbulence occurring in the flow are not taken into account. The objective of using CFD to aid the 1D modeling is to ensure that these phenomena are approximated as close as possible to the actual behavior. On this ground, CFD results have been used for the head drops occurring in the volute throat and to account for the hydraulic efficiency across the components. A final CFD supported 1D model would thereby reduce cost and time involved in determining the performance of the PRT, compared to complete CFD or testing.

Even with CFD, for most complex flow phenomena such as turbulence, multiphase flows, etc., exact solutions are not feasible [24]. Hence we rely on different models to capture these complex flows. But this might end up reducing the accuracy of the solution, due to various errors. Modeling errors occur due to difference between the actual flow and the exact solution of the equations, which we use to represent them. Discretization and truncation errors are due to the difference between the exact solution to the equations that we use and the solution of their discretized forms. Numerical errors occur in the schemes we use to solve these discretized equations, due to the difference between the actual solutions of the discretized equations and the iterative solution to the differential equations [24]. The errors also depend on the type and size of mesh used to model the system. Hence even with CFD we end up only with an approximate solution to the physics we aim to study.

3.1. Governing Equations

Conservation laws are generally derived by considering a certain quantity of matter and its extensive properties, for example, mass, momentum and energy [24]. In the case of fluids, it is easier to deal with a specified region called the control volume (CV) through which the flow happens, rather than a quantity of matter. This is referred to as the control volume approach. We consider the two extensive properties, mass and momentum, and derive the Navier Stokes equations.

The conservation of mass equation is given as:

$$\frac{\partial \rho}{\partial t} + \vec{\nabla} \cdot (\rho \vec{v}) \;=\; 0, \tag{3.1}$$

where $\vec{v} = (u, v, w)$ is the velocity vector.

The conservation of momentum equation is given according to [24] as

$$\frac{\partial (\rho \vec{v})}{\partial t} + \vec{\nabla} \cdot (\rho \vec{v} \vec{v}) \;=\; \sum f, \tag{3.2}$$

where f is the sum of the external forces which can be surface forces such as pressure, surface tension, normal and shear stresses, or body forces such as gravity, electromagnetic, centrifugal and Coriolis forces. Expanding the surface force terms, equation 3.2 becomes

$$\frac{\partial (\rho \vec{v})}{\partial t} + \vec{\nabla} \cdot (\rho \vec{v} \vec{v}) \;=\; \vec{\nabla} \cdot \left(\vec{\vec{\tau}} - p\vec{\vec{I}} \right) + \rho \vec{f}. \tag{3.3}$$

Here $\vec{f} = (f_x, f_y, f_z)$ is the vector of external body forces. In the case of Newtonian fluids, the shear stress tensor $\vec{\vec{\tau}}$ is given as

$$\vec{\vec{\tau}} \;=\; -\left(p + \frac{2}{3}\mu \, \vec{\nabla} \cdot \vec{v} \right) \vec{\vec{I}} \;+\; 2\mu \vec{\vec{D}}, \tag{3.4}$$

where p is the static pressure, μ is the dynamic viscosity, $\vec{\vec{I}}$ is the unit tensor and $\vec{\vec{D}}$ is the rate of strain or deformation tensor given as,

$$\vec{\vec{D}} \;=\; \frac{1}{2}\left[\; \vec{\nabla} \vec{v} \;+\; \left(\vec{\nabla} \vec{v} \right)^T \; \right]. \tag{3.5}$$

We deal with incompressible flows, where the density of the fluid is constant with increase in pressure. The velocity and the pressure can be obtained from the mass and the momentum conservation equations. Temperature effects are small for hydraulic turbines. Hence, the equation of conservation for energy need is not considered for this study.

3.2. Modeling of Turbulence

The flow in a PRT is characterized by turbulence. Turbulence is the random chaotic motion exercised by a fluid in both space and time. The advantage of the Navier Stokes equations over the Euler equations discussed in section 2.6.2 is that the viscous effects are taken into account. Hence they can be used for better analysis of the losses and separation happening in the different components [25]. Turbulence is yet to be understood and solved completely. Therefore, a broad range of techniques are used to model it.

3.2.1. Reynolds Averaged Navier Stokes Equations

The Reynolds Averaged Navier Stokes (RANS) equations are used to model the turbulence in a flow. The direct approach for solving the Navier Stokes(N-S) equations for turbulence is by using the Direct Numerical Simulations(DNS). They solve the N-S equations by resolving all the motions and have been proved to be the most accurate [24]. But the computation time and resources for DNS are extremely high. Hence turbulence is modeled in terms of statistical mean quantities [26]. Reynolds developed equations using the mean velocity field instead of the velocity itself by averaging the N-S equations. The properties are written as the sum of their mean component ($\overline{\phi}$) and a time varying fluctuation component ($\phi^{'}$).

$$\phi = \overline{\phi} + \phi^{'}. \tag{3.6}$$

$$\overline{\phi} = \frac{1}{\Delta t}\int_{t}^{t+\Delta t} \phi \, dt. \tag{3.7}$$

The Δt is a time scale which should be chosen such that it is smaller than the time scale at which the equations are solved and larger than the time scale of the turbulent fluctuations. Adopting equation 3.6 into the properties p and ρ and using them into equations 3.1 and 3.3, we obtain the RANS equations.

The RANS equations for incompressible, unsteady flow, considering a constant molecular viscosity μ are,

$$\vec{\nabla}\cdot(\overline{\vec{v}}) \;=\; 0, \tag{3.8}$$

$$\frac{\partial \overline{\vec{v}}}{\partial t} \;+\; \overline{\vec{v}}\cdot\vec{\nabla}\overline{\vec{v}} \;=\; -\frac{1}{\rho}\vec{\nabla}\overline{p} \;+\; \frac{1}{\rho}\vec{\nabla}\cdot\left(\overline{\overline{\tau}} - \rho\overline{\vec{u}'\vec{u}'}\right) \;+\; \vec{f}, \tag{3.9}$$

where $\overline{\tau}$ is the shear stress corresponding to the mean flow, and the term $\rho\overline{\vec{u}'\vec{u}'}$ is called the Reynolds stress term. The Reynolds stress term is a measure of the turbulent dissipation and is the additional term compared to equation 3.3. For the steady state solution, equation 3.10 becomes

$$\overline{\vec{v}}\cdot\vec{\nabla}\overline{\vec{v}} \;=\; -\frac{1}{\rho}\vec{\nabla}\overline{p} \;+\; \frac{1}{\rho}\vec{\nabla}\cdot\left(\overline{\overline{\tau}} - \rho\overline{\vec{u}'\vec{u}'}\right) \;+\; \vec{f}. \tag{3.10}$$

Expanding this representation results in more number of unknowns than equations, Due to this closure problem, a turbulence model is needed to represent the Reynolds stress terms for finding the solution to these equations.

3.2.2. Turbulence Modeling

Based on the turbulent-viscosity hypothesis, a number of models are used to estimate the Reynolds stresses. Some of them are discussed here :

- The zero equation models are very robust, as they are calculated algebraically from the flow variables, and do not require solving ordinary differential equations. However, these models are not very accurate [26].
- The one equation models are those, in which the transport equations are solved for one quantity, the turbulent kinetic energy, k. They are more accurate than the one equation models. But, they have

the drawback of being incomplete since they require a length scale, a flow dependent quantity, which needs to be specified [26].

- The two equation models involve transport equations being solved for two turbulence quantities. They are more complete as they do not require any flow dependent specification. $k-\epsilon$ and $k-\omega$ are the most widely used two-equation models used on commercial CFD codes.

$k-\epsilon$ MODEL

The transport equations are solved for the two quantities, the turbulent kinetic energy, k and the turbulent viscous dissipation rate, ϵ. It models turbulence based on how the turbulent energy is dissipated by the eddies in the form of heat. $k-\epsilon$ model gives good results in the free stream region, has a good convergence rate and requires lesser memory than equivalent models. But k goes to zero at the walls, hence resolution is poor close to the walls and in regions of adverse pressure gradients [27]. Hence $k-\epsilon$ is not suitable for systems with rotating fluids, boundary layer separations, or geometries with curved surfaces.

$k-\omega$ MODEL

The $k-\omega$ model is based on a relation between the the turbulent kinetic energy, k and the turbulent frequency, ω. $k-\omega$ deals well with domains having adverse pressure gradients. Hence it is well suited to the near wall regions (boundary layer and viscous sub-layers). But it can have a strong influence and sensitivity on the incoming turbulence length-scale [28]. It is also not as good in the free stream region as the $k-\epsilon$ model. It takes up more time for convergence and more memory than the $k-\epsilon$ model.

$SST\ k-\omega$ MODEL

The Shear Stress Transport(SST) k-omega model is a hybrid model combining the $k-\epsilon$ in the free stream region and the $k-\omega$ model near the walls by the use of a blending function [29]. It initiates the appropriate model depending on the region of interest. Hence it eliminates the disadvantages of both the models. $SST\ k-\omega$ switches between using and not using wall functions, and is more accurate in near-wall regions than the $k-\epsilon$ model. It also does not have unrealistic sensitivity to the inlet turbulence length-scale [28]. Hence it is preferred for boundary layer simulations which require high accuracy.

NEAR-WALL TREATMENT

The accuracy of the wall shear stress and flow prediction depends greatly on the near-wall treatment, which influences the development of the boundary layers. This means that, there should be enough grid points in the boundary layer, to fully resolve the flow. Hence the viscous sublayer is bridged using wall-functions to determine the boundary conditions for the mean flow and turbulence transport equations [29]. Most commercial codes solve the transport equations at the center of each cell. Hence the values or conditions at the center of the first cell should be determined for solving the equations of the mean flow and turbulence.

The wall shear stress is given by τ_w and u_τ is the friction velocity defined by

$$u_\tau = \sqrt{\frac{\tau_w}{\rho}}. \tag{3.11}$$

If u^+ is the dimensionless velocity given by $\frac{\overline{u}}{u_\tau}$, according to the law of wall,

$$u^+ = f(y^+) = \left(\frac{1}{\kappa}\ln y^+\right) + B, \tag{3.12}$$

where $\kappa \approx 0.41$ is the von Kármán constant, $B \approx 5.2$ is a constant depending on the roughness of the wall and

$$y^+ = \frac{u_\tau y}{\nu}. \tag{3.13}$$

Here, y is the distance of the first cell from the wall. y^+, which is the non-dimensional wall distance, is a good estimate of how coarse or fine a mesh is. y^+ is better illustrated in figure 3.1.

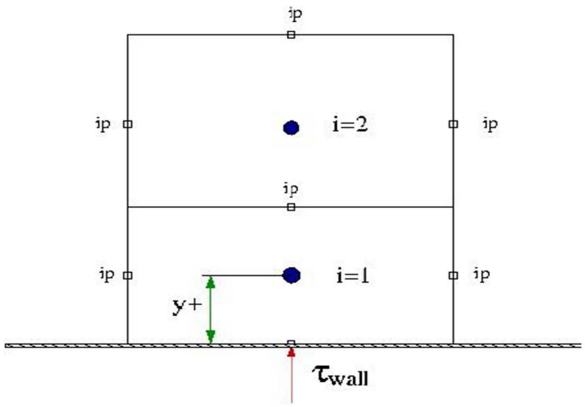

Figure 3.1: Cell Height for Near Wall Treatment [29]

Commercial softwares generally solve the transport equations at the center of each cell. Hence it is important to determine the values at the center of each cell to solve the equations. Hence as shown in figure 3.1, y^+ becomes significant. It is recommended that the y^+ values should always be greater than 11 when using wall functions, because outside them (y^+<11), the wall functions over-predict the turbulent kinetic energy. They should also be in the log law region [29]. The $k-\epsilon$ model generally requires a y^+ value of 30-100 as it uses a wall function to resolve the boundary layer. The $k-\omega$ model on the other hand does not use wall functions and hence y^+ should be approximately equal to 1. For $y+ < 2$, the $SST\ k-\omega$ model switches to a low-Re formulation near the wall, rather than the wall function formulation. If 11 < y+ < 300, the results will be fairly similar to the $k-\epsilon$ model since wall functions are used. For 2 < y+ < 11 the results are obtained, with a blend between wall functions and low-Re formulations.

3.3. ANSYS CFX

The simulations for the prediction of the PRT performance have been done using the commercial software package ANSYS 16.2. The Workbench enviroment of ANSYS links all the required simulation software tools. It is used to transfer information between the various components needed for our study, in sequence: geometry, meshing, setup and post-processing. Designmodeler is used to design and modify the geometry or import external CAD models, needed for our PRT models. The mesh for the fluid domain is generated using Turbogrid and ANSYS Meshing. Once the model has been meshed, it is imported to CFX. CFX is divided into three sub-components, namely CFX-Pre, CFX-Solver and CFX-Post. The entire physics corresponding to the flow model and the simulation settings are defined in CFX-Pre. Fluid properties, boundary conditions, interfaces, numerical schemes for the solution, turbulence model, convergence criteria etc., are be chosen here. CFX-Solver solves the equations based on the inputs and provides the output file. The visualization and the post processing of the converged results is done using CFX-Post.

3.4. Simulation Setup

The various components of CFX as explained earlier, are used in a sequence in setting up the simulations. The 11 stages of the PRT are simulated stage-by-stage, whose details are shown in table 3.1 below:

STAGE	Runners	Vanes	Crossover	No. of stages
First series stage	Single suction	3 vanes	Type 1	5
Second series stage	Single suction	5 vanes	Type 1	5
Last stage	Double suction	3 vanes	Type 2	1

Table 3.1: PRT - Stage Split

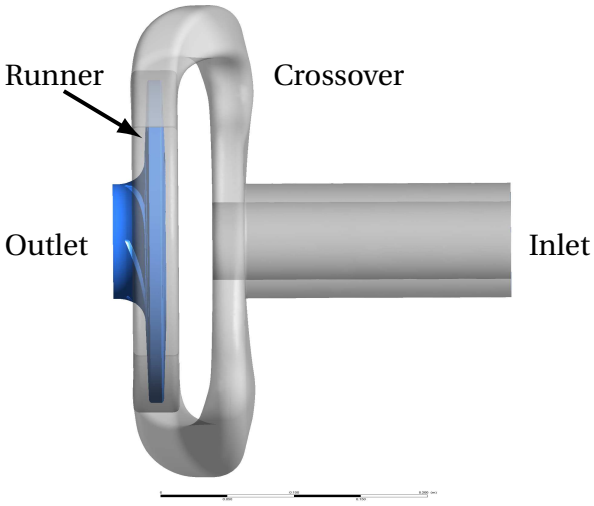

Figure 3.2: Single Stage CFD Setup

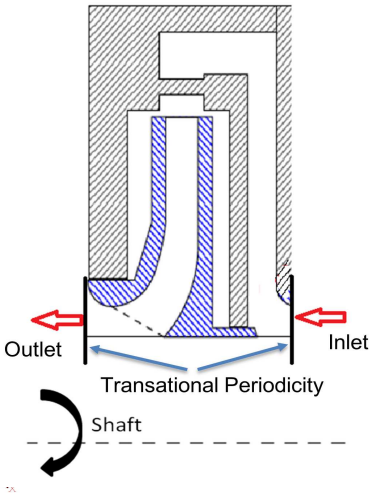

Figure 3.3: Single Stage Representation

Figure 3.2 shows a typical single stage of the PRT used for the simulation. The crossover domain from the inlet to the PRT is shown in gray, while the runner is shown in blue. The single stage simulations are done for the three runner-crossover setups as shown in Table 3.1 in the sequence described below.

Each of the stages in the multistage pump is a runner-crossover combination as shown in figure 3.2. The entire setup of the multistage pump will be explained in detail in chapter 4. There are two sets of five similar stages in the PRT. Since it is quite expensive in terms of time and resources to simulate the whole multistage setup, the methodology is to simulate the single stages and then combine them applying translational periodicity as explained figure 3.3. It means that, we simulate the two different stages individually, to study their performance. Since the stages of the same type behave similarly, the performance of the PRT is predicted by sequentially combining the stages which show similar performance. Each of the single series stages are similar to the setup shown in figure 3.3, whereas the last stage consists of a twin runner. This stage is the first stage for the pump. The meridional diagram of the last stage is shown in figure 3.4.

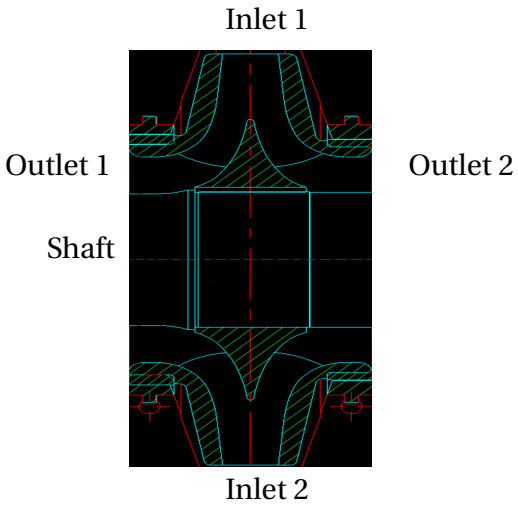

Figure 3.4: Last stage - Meridional Diagram

3.4.1. Geometry

The model of the runner is created by Flowserve's in-house software. The model is built with input geometric parameters i.e.,the width, radii, angle and thickness distribution. The output generated by the software is sent to BladeGen in ANSYS. The modifications like extension of the outlet area, which may be needed in the case of non-converging solutions, can also be performed using BladeGen. The crossover geometries are generated using CAD software and are imported into Designmodeler along with the blade geometries. The rearrangement of the entire geometry, creation and modification of the fluid domain is done in Designmodeler. The domain generated for the analysis is then sent to TurboGrid or ANSYS Meshing to generate the mesh. The geometry and the dimensions of the three types of runners are obtained from hydraulic drawings at Flowserve.

3.4.2. Meshing

The runner vanes and the fluid domain of the crossover and the volute are meshed separately using TurboGrid and ANSYS Meshing respectively. TurboGrid is tailored for meshing turbomachinery components. The runner geometry is exported to TurboGrid. The software divides the imported mesh into three domains: inlet, blade and the outlet. Suitable adaptations such as extension of the domain can be done to the inlet and the outlet domains. TurboGrid automatically generates a high-quality structured hexahedral mesh for the blade passage. This gives us the benefits of minimum mesh dependency when we study the performance of different designs. TurboGrid optimizes the blade mesh automatically with good grid angles and smooth

mesh transitions [30]. The mesh is created using the ATM Optimized Topology. The mesh is fine near the surfaces of the runner and in places of adverse pressure, velocity gradients. A coarser mesh is generated in areas of smaller pressure gradients and in the free stream regions. The mesh is controlled manually using the expansion ratio and the global size factor. Expansion ratio is the difference is size between the neighbouring cells. It relates the largest and the smallest sector volumes in the mesh domain. The global size factor controls the total number of elements in the mesh. The runner has been meshed with an offset $y^+ \approx 11$. This is to limit the number of elements in the mesh, while capturing the best of features in the flow. At $y^+ \approx 11$, the SST uses a blend of wall functions and low Re formulations, which is suitable for a performance analysis of a whole multistage PRT. The meshing has been discussed more in detail in section 3.5.

The rest of the fluid domain is meshed using the ANSYS Meshing tool. The meshing is controlled using the number of cells and the growth ratio. The inflation layers, which specify the number of cells required close to the wall, to capture the large velocity gradients, is also controlled well using the ANSYS Meshing tool. ANSYS meshing gives importance to the quality and fineness of the mesh in areas like inflation layers and cutwaters, where we expect complex flow patterns. With the proximity and curvature criteria turned on, we exercise more control over the maximum and minimum mesh size, and growth rates. ANSYS Meshing generally generates an unstructured tetrahedral mesh since it is difficult to obtain a structured mesh for the PRT geometry. The dependencies on these adjustments of the mesh on the results is analyzed through the Grid Sensitivity study explained in section 3.5.

3.4.3. Solver Setup

The mesh created for the geometry is sent to CFX-Pre. In CFX-Pre, the physics of the simulations are defined. They include the properties of the fluids, the boundary conditions, numerical schemes, and the physical models based on which the calculations are done. The fluid is water at 25^0C. The stationary (crossover) and the rotating (runner) domains are setup, with appropriate boundary conditions at the inlet. The stages are simulated for a wide range of volumetric flowrates ($120-250m^3/hr$), given as the inlet boundary condition. The inlet is modeled with a turbulence intensity of 5% according to recommendations from literature [31]. The interfaces are modeled with the frame change/stage mixing model, which connects regions with non-matching grids together. The simulations in this thesis have been performed with the frozen rotor interface model which will be explained later in chapter 4. This model contains a frame change, but there is no change in relative position. The flow can freely recirculate across the interface [32]. The setup of the runner and the crossover domain for the CFD simulations are shown in figures 3.5 and 3.6 respectively.

The SST turbulence model is chosen because it contains the advantages of both the $k-\epsilon$ and $k-\omega$ models, and its applicability to both the near-wall and the free stream regions. CFD simulations of multistage pumps are very time consuming. Hence a few assumptions are made to simplify the analysis and to aid the development of the 1D model. The simulations for each of the stages as mentioned in table 3.1 are to be performed to derive a 1D model and compare it with the full PRT test data. So the flow is assumed to be in steady state for the three types of individual stage simulations, with the wide range of input parameters. The discretization of the equations is done using the first order turbulence scheme. The high-resolution advection scheme option in CFX-Pre according to guidelines from Anup et al., [33]. This is because the high resolution scheme involves non linear solutions, which helps avoiding oscillations and wiggles in the solution, generally found in linear advection schemes.

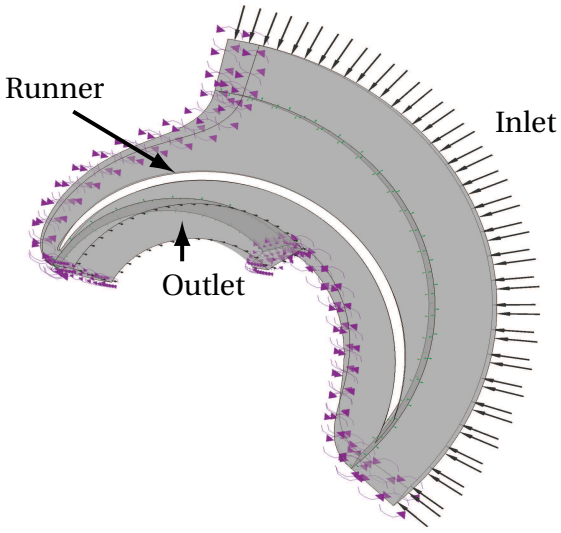

Figure 3.5: Runner setup - CFX.

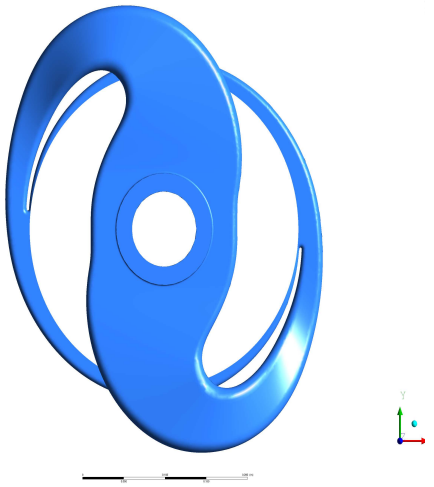

Figure 3.6: CFD model of a crossover(rear view)

CONVERGENCE CRITERIA

Since the fluid problems are highly non-linear in nature, and restrictive conditions are imposed, the program solves the equations iteratively. Therefore the convergence of the solution is important for an accurate result. The residuals need to be monitored, ensuring the conservation of the quantities and the proper convergence of the output values, or in other words, our quantities of interest. CFX generally outputs the root mean square(RMS) values of the residuals. RMS values of 10^{-4} is often a good indicator of good convergence, which means that the residuals have gone down 10^{-4} orders of magnitude from the beginning till the end. But values of 10^{-5} indicate a well-converged solution, while residuals with a value 10^{-6}, show that the solution is tightly converged [34].

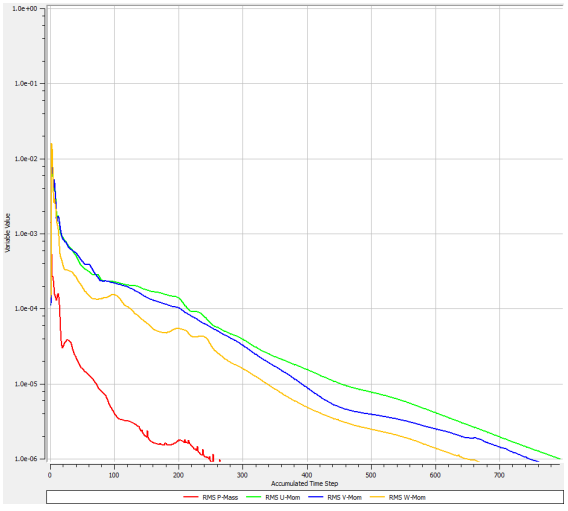

Figure 3.7: Converged solution for 3 vaned series runner stage after 800 iterations. Q = BEP

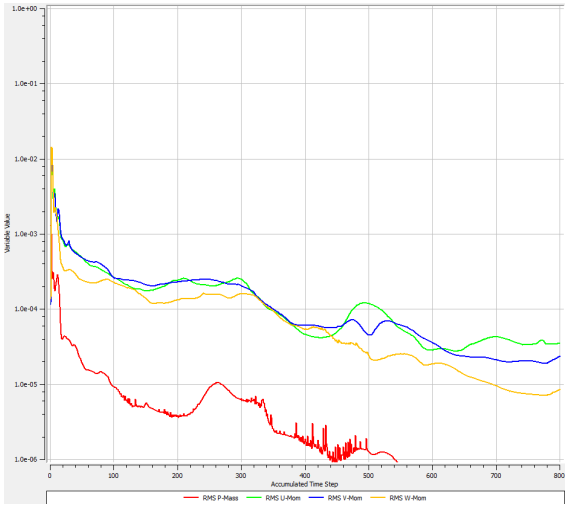

Figure 3.8: Non-converged solution for 3 vaned series runner stage after 800 iterations. Q = 0.6BEP

The CFD imbalances, which are indicators of the conservation of the equation quantities, are never exactly zero. They are monitored and solution imbalances of below 1% are preferred. Lower values of residuals also give low imbalances. Figures 3.7 and 3.8 indicate the converged and non-converged solutions for the

same simulation at Q = 0.6BEP and Q = BEP respectively. BEP means the Best Efficiency Point of the PRT. It can be seen that at BEP flow, a good convergence is achieved with a residual RMS magnitudes of 10^{-6}. But at lower flow rates, such as in figure 3.8, the residual RMS is only about 10^{-4} for the same number of iterations. The flow is unstable and has oscillations. The imbalances also have higher values than those of the BEP flow. This is because of the unsteady behavior at low flow rates. Hence steady flow could not be assumed for low flow rates.

3.5. Grid Sensitivity Study

The predictive capability of CFD, depends a lot on the resolution of the spatial grid, in addition to the physical sub-models employed(eg., turbulence, multiphase flows) [35]. In any study, importance is placed on the control of numerical accuracy. Considering the time and computational resources available, an optimum mesh size has to be decided upon for our analysis, such that the accuracy of the solution is preserved. The grid sensitivity study is carried out, with this as the objective. It addresses the use of improved grid resolution in evaluating accuracy. In this study, the grid independence is done using Richardson extrapolation method based on the guidelines from Philips and Roy [35]. A short summary for comprehension of the results is given here, while the detailed discussion is done at the Appendix A.

Three different grid densities (Fine-G_1, Medium-G_2 and Coarse-G_3) were used and simulated for grid independence, to decide on the best economical mesh that could be used for our simulations. This was done for the three types of runner-volute combinations used in the PRT. The best grid for the simulation is chosen for one stage by comparing combinations of two grids and deriving their Grid Convergence Index (GCI). The GCI is widely used as an uncertainty estimator. It compares two spatial grids and gives an estimate of how close two grids solutions are, to each other. It is derived based on the output parameters ϕ, in this case, the head(H) and the efficiency(η) values. The mesh sizes of the chosen refined grids are given by:

$$h = \left[\frac{1}{N} \sum_{i=1}^{N} V_{domain} \right]. \tag{3.14}$$

If a and b are the two meshes to be compared r_{ba}=$h_b - h_a$, the mesh refinement is given by,

$$e^{ba} = \left| \frac{\phi_a - \phi_b}{\phi_b} \right|, \tag{3.15}$$

$$GCI^{ba} = \frac{1.25 e^{ba}}{r_{ba} - 1}. \tag{3.16}$$

Grid Convergence - Interpretation

The interpretation of the GCI is that the lower the value of the GCI between two meshes, the closer are the results. The mesh with the lower number of elements, in the combination with the lower GCI value is chosen for analysis. This is because increasing the number of elements beyond this gives relatively a smaller difference in the results. The grid sensitivity is initially performed for the runner exclusively, after meshing with TurboGrid. The mesh for the runner has been improved by adjusting the mesh global growth factor and the spanwise blade to blade ratio with values of 1.14, 1.30 and 1.36. The range of values were chosen based on the previous simulations on centrifugal pumps done at Flowserve, also considering the limitations imposed on the mesh size by the number of licenses. The results of the grid sensitivity analysis for the runner are shown in table 3.2. It is seen from the table that the GCI value for the fine-medium combination has a

low value for both the head and the efficiency values. Hence the medium mesh with factor values 1.30 is chosen as the setting for the simulations. The sensitivity analysis is now done with these fixed settings for the runner mesh and incorporating changes in the crossover-volute fluid domain mesh. The crossover mesh is modified by changing the number of inflation layers in the mesh as 10,11 and 12 respectively and by keeping the growth factor constant. The results are shown in table 3.3. Head is considered a more important estimate in terms of pump performance according to American Petroleum Institute (API) Standard 610 [36]. It can be seen that the GCI value for the combination of Grids 1-2 is lower than that of Grid 2-3. Hence the number of inflation layers is chosen as 10 for the 5-vane runner stage. Typical meshes used in this study generated using TurboGrid and ANSYS Meshing are shown in figures 3.9 and 3.10 respectively. The mesh generated by ANSYS Meshing at the throat and cutwater region is also shown in figure 3.11. The proximity and curvature setting in ANSYS Meshing generates a finer mesh in these regions based on curvatures, to capture the high gradients in the flow.

	Elements	**Growth Factor**	**Outputs**		**GCI (%)**		
			Head(m)	**Efficiency(%)**	**Combination**	**Head**	**Efficiency**
Grid 1	500,292	1.14	162.31	77.60	Grid 1-2	1.16	1.53
Grid 2	1,049,436	1.30	163.97	78.64	Grid 2-3	0.17	0.02
Grid 3	1,421,598	1.36	163.89	78.65	-	-	-

Table 3.2: Grid sensitivity study for 5-vane runner

	Elements	**Inflation Layers**	**Outputs**		**GCI (%)**		
			Head(m)	**Efficiency(%)**	**Combination**	**Head**	**Efficiency**
Grid 1	3,630,532	10	255.61	79.92	Grid 1-2	2.29	3.34
Grid 2	4,553,092	11	256.80	79.38	Grid 2-3	4.87	2.00
Grid 3	4,985,070	12	257.75	79.26	-	-	-

Table 3.3: Grid sensitivity study for 5-vane full stage

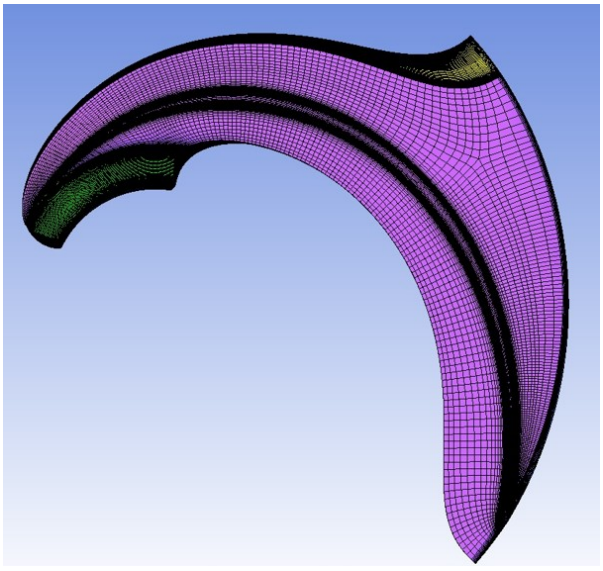

Figure 3.9: Runner mesh generated using TurboGrid(only one blade shown)

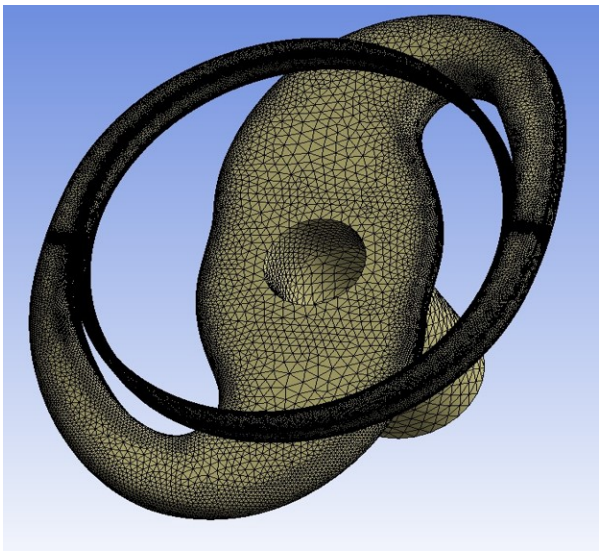

Figure 3.10: Mesh for crossover-volute flow domain generated using ANSYS Meshing

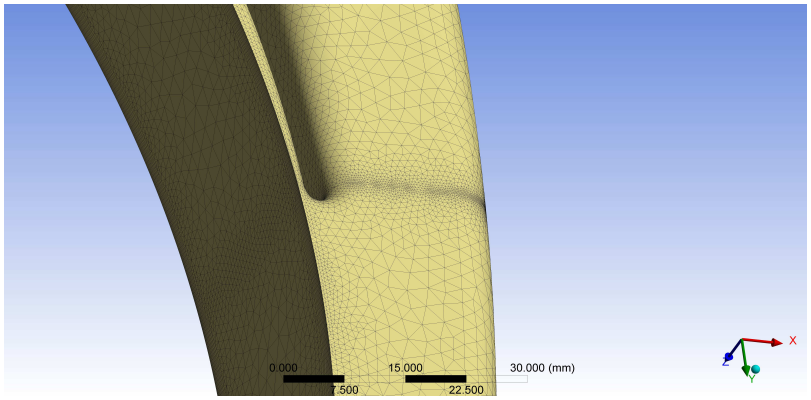

Figure 3.11: Cutwater region mesh

3.6. Stage CFD simulations

The PRT consists of two different types of series stages (5 stages each) and a last stage. The last stage of the PRT(which is the first stage in the pump), which also consists of a 3 vane runner, is modeled with similar mesh settings as the 3 vane series stage. A common global size factor and spanwise blade to blade factor of 1.30 for the runner, and 8 inflation layers are chosen as the appropriate settings for the last stage. CFD simulations are performed for one of each of the 5 vane and the 3 vane series stages, and for the last stage. The same fluid properties and boundary conditions are used for all these simulations. The performance curves are derived from the results of these simulations. The head curves for the three stages are shown in figure 3.12.

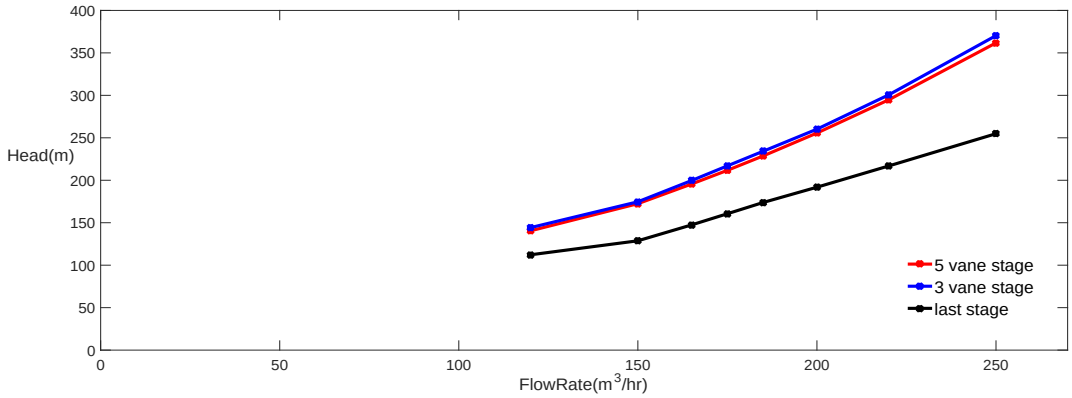

Figure 3.12: H-Q curves for the different stages of the PRT

The H-Q curves are more horizontal at lower flow rates and become steeper with higher flow rates. The simulations at lower flow rates below the BEP also becomes unstable due to the incidence and recirculation losses within the runner. This has been illustrated by figure 3.8 through the convergence behavior. From figure 3.12, it can be seen that the head drop curves of the series stages are similar, as they have the same crossover and dimensions, except the difference in the number of vanes. The 3 vane runner stage creates a greater head drop than the 5 vane runner stage.

Since the CFD simulations do not involve the leak paths, they only account for the hydraulic efficiency across the PRT. The hydraulic efficiencies obtained from the CFD simulations are used for the modeling of the PRT performance. The models for the leakage flows, as discussed in section 2.7 are built around the 1D head

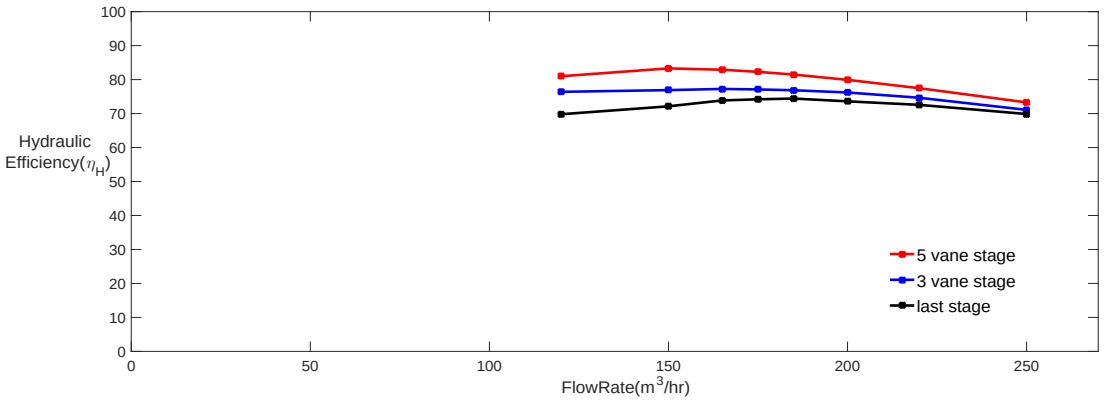

Figure 3.13: Q-η_H curves for the different stages of the PRT

or pressure drops across stages. Since the CFD simulations do not include the leak paths, they give only an estimate of the hydraulic efficiency. The combined head drop across the components are corrected with the hydraulic efficiency, obtained from CFD. This will be after estimating the head drops across the components, explained in detail in chapter 4. The efficiencies are also compared between the series and the last stages, and are shown in figure 3.13.

3.7. Test measurements

The results from the CFD aided 1D model are to be compared with the test measurements. The multistage pump with the setup as shown in table 3.1 is tested as a PRT at the Flowserve test facility, to measure its performance. The test was conducted to check, if the PRT met rated conditions and customer specifications.

3.7.1. Test specifications and calculations

The performance of the PRT is tested at various flow rates with water in a closed loop. These measurements are done according to the American Petroleum Institute(API) 610 11^{th} edition standard [36]. According to the API standard, the PRT should be tested for flow rates close to shut-off and at least within the range 95 - 105% of the rated flow. The performance at shut-off (zero discharge flow) is not measured at Flowserve, Etten-Leur as this is not feasible for multistage pumps. The temperature of the fluid is measured in the pipes before entering and after exiting the PRT. The fluid used is water. The flow rate is measured with magnetic flow meters at the inlet of the PRT. The suction pressure is measured just before the inlet of the PRT and the discharge pressure, just after the outlet of the PRT. The head drop across the PRT is calculated according to the equation,

$$H = \frac{P_2 - P_1}{\rho g} + \frac{V_2^2 - V_1^2}{2g} + Z_2 - Z_1, \tag{3.17}$$

where the pressures and the velocities are denoted by P and V, with the subscripts 1 and 2 denoting the values at the inlet and the outlet respectively. The power delivered by the fluid, P_p was calculated using the obtained head with the equation,

$$P_p = \rho g Q H_{test} \tag{3.18}$$

If P_s is the power obtained from the shaft, the efficiency of the PRT is obtained from,

$$\eta_{PRT} = \frac{P_s}{P_p} \times 100\% \tag{3.19}$$

The tolerances for the measurements are obtained from the API standard. However, the specifications and their tolerances differ according to the customer. The performance tolerances mentioned in the API 610 11^{th} edition are ±3% for the head, and the rated flow should be within 80% to 110% of BEP [36]. There are no tolerances specified for the efficiency.

3.7.2. Results and modifications

The performance test was conducted for the PRT for a wide range of flow rates between 87 - 235 m^3/hr. The rated conditions for the PRT, shown in table 3.4, were determined by the customer. The test shows that the PRT did not break enough head at the rated flow. The BEP was as a higher flow rate than expected.

Rated Capacity(m^3/hr)	180.6
Rated Speed(rpm)	2985
Rated Head(m)	1986
Rated Efficiency(%)	58
Specific Gravity	0.7

Table 3.4: PRT Test - Rated conditions

The throat areas were then measured, and it was found that they were on average 12.4% larger than the areas according to the hydraulic drawing for the series stages. The reduction of the throat area was then done by bolting inserts into the casing. This resulted in a throat area 15.1% lesser than that given by the hydraulic drawing. The performance test was then done for the PRT with the modified throat areas. We thus obtain two sets of performance curves for the multistage PRT, for the smaller and the larger throat areas with which the 1D-CFD model can be validated. Hence the CFD simulations are performed for three stage setups, with the design (according to hydraulic drawing), smaller and larger throat areas, to analyze the performance and to validate the results. The validation will be discussed in chapter 5.

4

1D-CFD Modeling Results

The modeling of the multistage PRT is performed in two steps. In the first step, the single stages are modeled, using a combination of 1D methods and CFD results. The 1D results are validated with CFD. In the second step, the model for the single stages are combined together to obtain the complete model for the multistage PRT. The single stage modeling is done by combining the models for the components within the stage in a sequential manner. The sequence in which the modeling is done for a single stage is shown in figure 4.1. The components within a single stage in meridional view are shown figure 4.2.

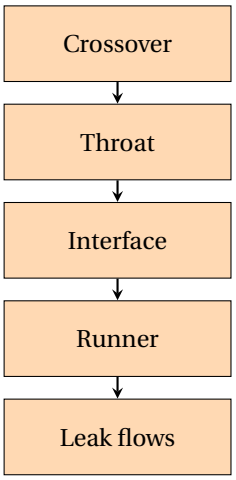

Figure 4.1: Single stage sequential modeling

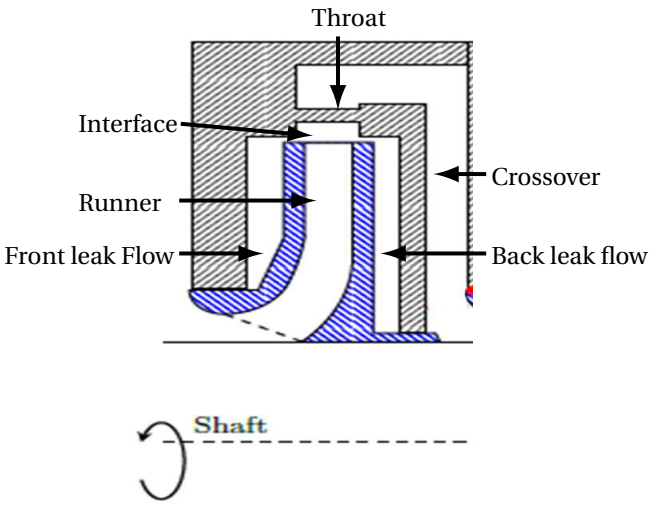

Figure 4.2: Components for modeling

The crossover, interface, runner and the leak flows are modeled using 1D methods. CFD results obtained from the setup discussed in chapter 3, have been used for the head drop across the throat area, and the hydraulic resistances. This completes the model for a single stage. The individual stages are then put together,

for the multistage model. When combining the stages together, the leak flows between the stages also need to be taken into account. An iterative analytical scheme is used to model these leak flows to complete the performance prediction of the PRT. The fluid used is water, and the flow is assumed to be in steady state in the CFD simulations. Uniform velocity conditions are used at the inlet of every stage for both the CFD and 1D modeling. Sections 4.1 and 4.2 explain results for the crossover and the throat-volute interface models respectively. Section 4.3 explains the results obtained from the calculations for the runner. Section 4.4 discusses the results of the leaks within a single stage, while section 4.5 explains how the leaks between stages are estimated.

4.1. Crossover modeling

The first step in the modeling is the crossover which connects one stage to the next. The crossover is a complex flow path which contains bends and curves. Since the pump contains a diffusing crossover to increase the pressure of the fluid, the flow is converging across the same path in the PRT mode. Hence the modeling is done by a lumped analysis, where the entire flow domain is broken down into smaller volumes whose behavior can be predicted using existing fluid models and pipe equations. Figure 4.3 shows the streamlines of the flow through the crossover domain. The planes shown in black are cut in post-processing to make those small volumes. The head drop occurring within smaller volumes is thus observed, and is modeled using analytical expressions based on the dimensions.

The average of the quantities of interest, such as the pressure and the velocities are determined at these planes shown in figure 4.3. The volumes which we obtain, resemble the flow through curved pipes and nozzles. Hence they are modeled based on the respective flow equations. The methodology has already been discussed in sections 2.4.1 and 2.4.2. Figure 4.4 shows the front and side views of the volumes obtained between different planes 4-5 (top) and planes 2-3 (bottom) shown in figure 4.3. The head drops across each of these small volumes until the cut-water, are lumped together, to build the entire model for the crossover.

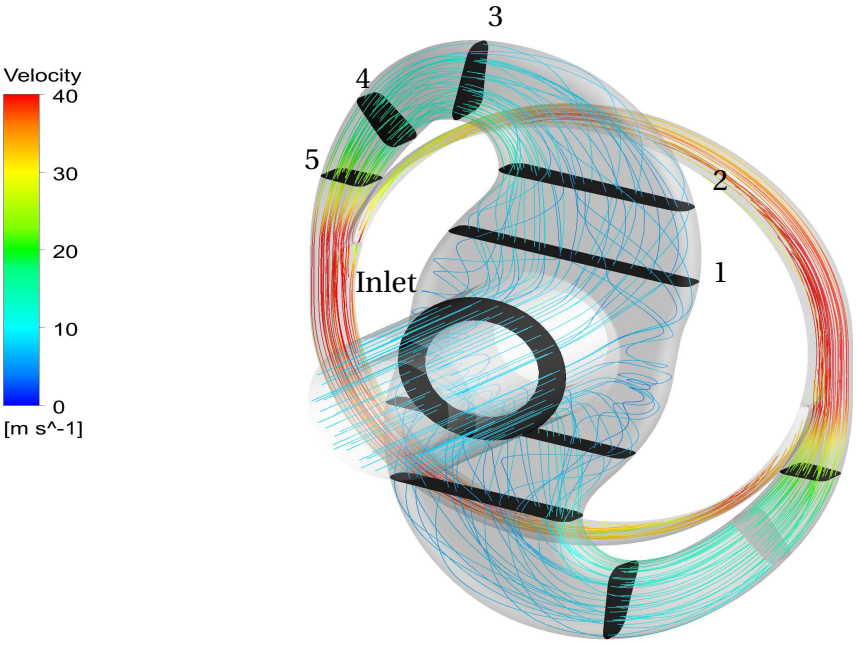

Figure 4.3: Streamlines of crossover flow. The cut planes are shown in black.

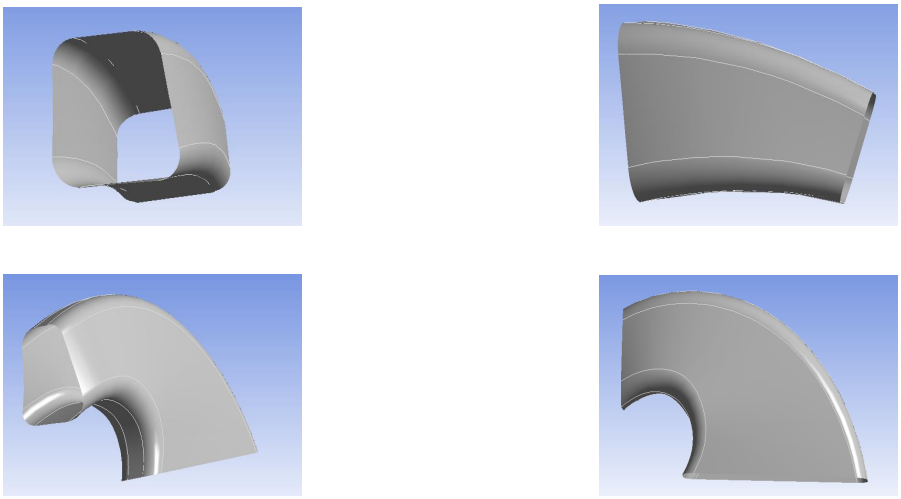

Figure 4.4: Volumes between planes 4-5 (top) and 2-3 (bottom). Front views(left) and side views(right).

4.1.1. Coefficients and Parameters

From equations 2.10 and 2.12, we see that the loss coefficients need to be determined. The choice of both the curve and the nozzle models are considered for all the sections, and the model is selected based on the comparison with the CFD head drop across that section. For flow through the curved pipes, equation 2.10 is used, which requires that f_s, the Moody friction factor from the Moody diagram and k_b, the bend loss coefficient are to be determined. These are discussed more in detail in the Appendix B. For the nozzle equation used to model the section volume between planes 1 and 2, the coefficient C_d is determined using equation 2.13. Table 4.1 shows the coefficients that are used in the calculations.

Section	**Type**	$\theta(deg)$	f_s(-)	k_b(-)	C_d(-)
Inlet -1	Curve	90	0.025	0.3	-
1-2	Nozzle	-	-	-	0.9878
2-3	Curve	90	0.025	0.3	-
3-4	Curve	60	0.025	0.37	-
4-5	Curve	20	0.025	0.3	-

Table 4.1: Coefficients for crossover model

4.1.2. Results

The pressure losses in a bend are due to friction and transfer of momentum between layers of the fluid, as the direction of flow changes along the path. A centrifugal force acts on the fluid due to the presence of a radial pressure gradient. The fluid at the inner side of the bend separates and moves outwards. The curvature induces secondary flow effects, as the fluid at the outer end moves slower than the fluid at the inner end. This slower moving fluid at the outer end therefore drifts towards the inner side. The flow obtained in a curved section of the pipe is shown in figure 4.5.

The head drops determined across the small volumes are lumped together to obtain the cumulative head drop across the whole crossover. The results obtained from the lumped model are plotted against the flow rate to obtain the head drop curves. These calculations are done until plane 5 as shown by the schematic

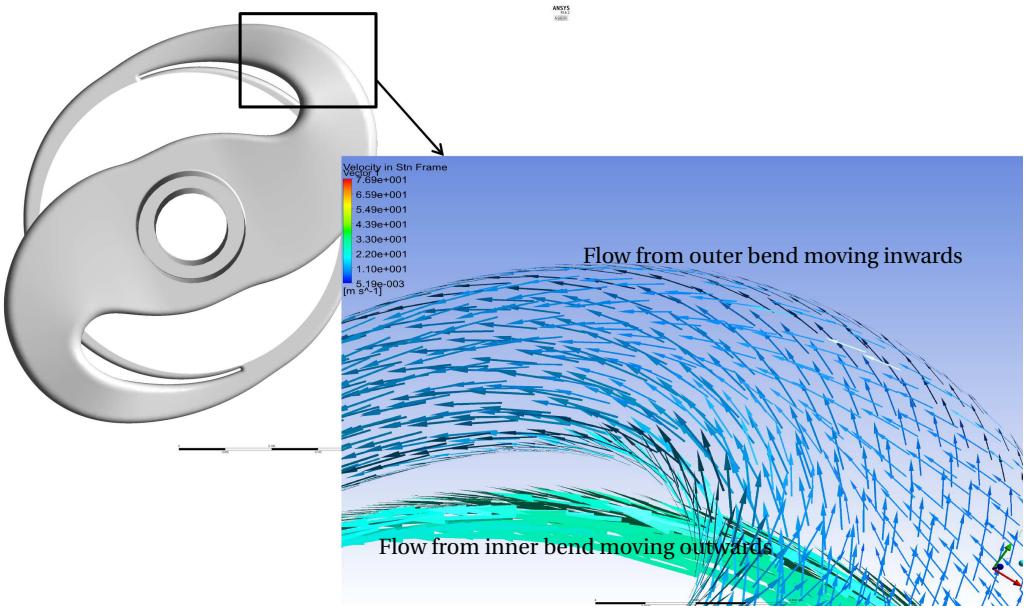

Figure 4.5: Flow observed in a curved section of crossover. Black arrows show flow from inner bend moving outwards. Outer flow moving inwards is shown by blue arrows.

4.3. It is found that the crossover contributes to around 3-4% of the total head drop occurring across both the series stages and the last stage. The results of the model in comparison with the results obtained from CFD are shown in figure 4.6. The deviation between the 1D and the CFD head drops is attributed to the selection of coefficients, interpolating values from the graphs for the Moody diagram. There is also a possible difference between the angles manually calculated from the hydraulic drawing, to the actual angles of the bend existing in the 3D configuration.

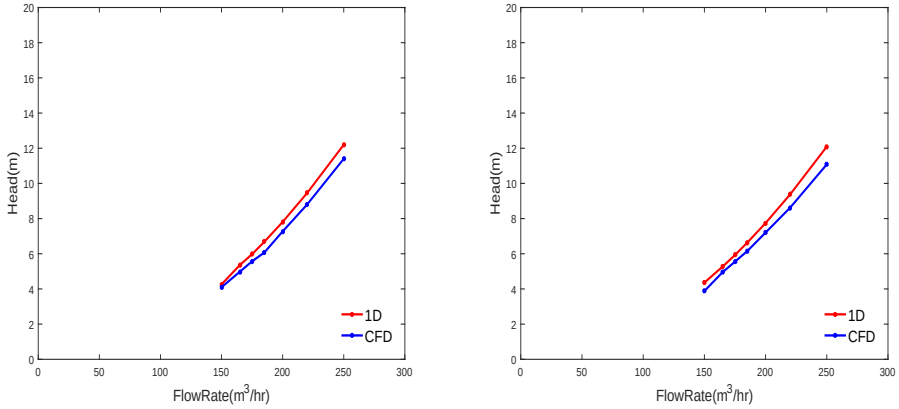

Figure 4.6: Comparison of 1D and CFD Head drops across crossover. The left figure shows the drop across the series stages with the same type of crossover, the right one shows the drop for the first stage

Table 4.2 shows the comparison between the 1D calculations and the CFD results for the crossover for a flow rate of $150 m^3/hr$. It can be seen that the 1D model over-predicts the overall head drop. The difference in prediction in the curved sections contributes the most to the deviation between the 1D and the CFD results. Since the head drop due to the crossover is considerably smaller compared to the whole stage head drop (about 3-4%), the deviation is of low significance. From this context, the 1D model provides a relatively good picture of the actual head drop across the crossover.

Section	CFD Head Drop (m)	1D Head Drop (m)	Deviation (%)
Inlet - 1	1.85	1.92	+3.65
1-2	0.54	0.52	-3.70
2-3	1.16	1.29	+13.00
3-4	0.48	0.36	-25.00
4-5	0.45	0.46	+2.22
Total	4.45	4.55	+2.22

Table 4.2: Comparison of CFD and 1D head-drops across crossover for $Q = 150 m^3/hr$.

4.2. Interface modeling

One of the critical areas of analysis in the PRT is the interface between the runner and the crossover. The fluid passes from the crossover, across the throat into the volute, and then into the runner. In the case of a pump, the fluid from the volute, hits the cutwater and goes into the crossover. In the PRT mode, the fluid flows past the throat and enters into the volute through the cutwater. This section explains the modeling of the fluid exiting the throat, followed by the modeling of the volute interface.

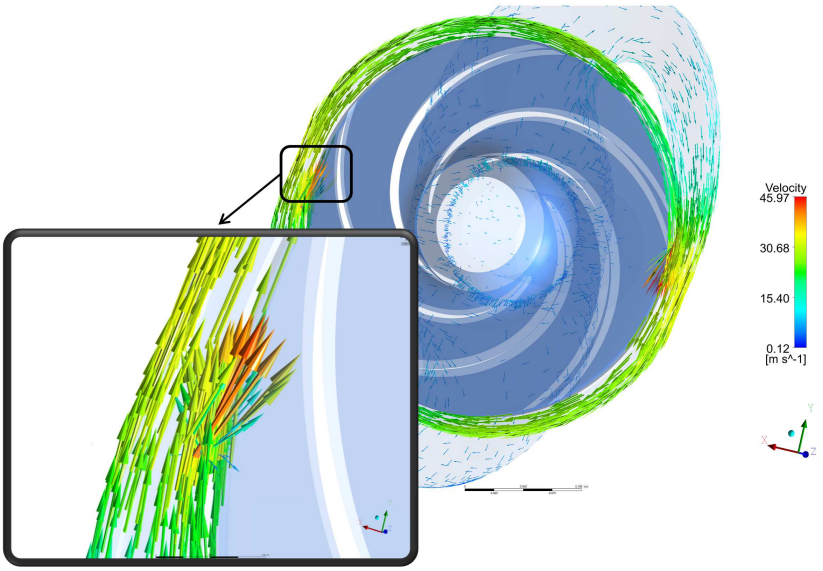

Figure 4.7: CFD Visualisation of interface velocities. The zoomed figure shows the velocities at the throat.

4.2.1. Modeling the throat

Modeling the outflow from the throat is important to determine the inlet conditions of the runner. It is also significant to understand the effect of changing the cross sectional area of the throat on the total head drop. The throat and the interface are difficult to be modeled with a 1D method due to the complex 3D flow existing across the throat and the cutwater. An illustration of the flow from the crossover to the interface between the stationary and rotating parts are given in figure 4.7. It shows the velocity vectors only for the volute and the interface, without those on the runner. We observe that the average velocities are high at the exit of the throat (cutwater), and the flow behavior is highly three dimensional. This is due to the sudden expansion of the fluid past the cutwater and the interactions with the runner. This interaction makes it difficult to derive a 1D

model. Hence the results from the CFD are used to model the throat.

The throat head drops are obtained from the simulations for all the three configurations (design, smaller, and larger throat areas). Design configuration has a throat area according to the hydraulic drawing. The larger configuration has 123% the area of the design throat area, while the smaller throat is of 84% the design area. From the CFD results, a second order curve fitting is done for the throat head drop. Figure 4.8 illustrates the difference in velocity at the throat, for the three different throat areas. It can be observed that the velocity magnitudes are high at the exit of the throat for the smaller configuration, due to the constriction in area. The increase in tangential velocities across the throat and cutwater are more for smaller throat areas, leading to a higher head drop. Morever, it can also be seen that the velocity reached a very high value downstream from the cutwater, compared to the value at the cutwater. This effect is magnified in the case of the smaller throat area, while it is less pronounced in the configuration with the larger throat area. This is an important consideration in the design because the higher velocities lead to difference in circulation at the interface.

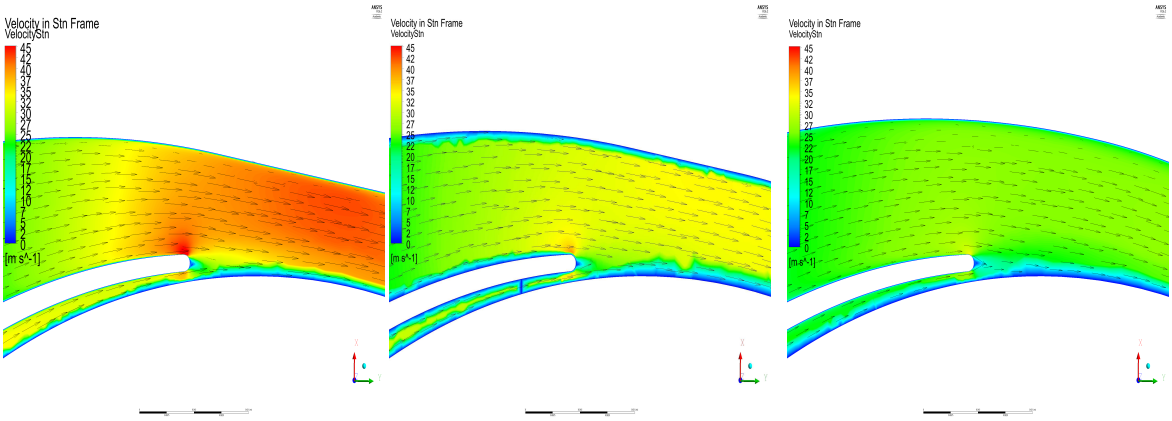

Figure 4.8: Velocities at the throat. The tangential velocity vectors are shown by the black arrows.

Figure 4.9 shows the head drop contour occurring across the stationary domain of the PRT for a single stage. The contours for all the three configurations are shown. The tangential velocity is extremely high at the exit of the throat for the smaller cross sectional area (figure 4.9b). This is seen from the darker yellow arrows for the design and smaller configurations compared to the larger one. The total head drop occurring across the respective configurations until the interface, are indicated by H, below each subfigure. These head drops show the influence of the change in throat area. They are substantially high for the smaller throat.

The tangential velocity of the fluid at the inlet to the runner needs to be determined to calculate the head drop across the runner. It is also the initial boundary condition to the leak flow model which will be discussed in section 4.4. Therefore, the tangential velocity of the fluid exiting the crossover is calculated from the throat area, and the clearance between the runner and the surface of the volute, as shown in section 2.5. The angle at which the fluid exits the crossover from the cutwater (α_{th}), is determined by using the pump drawings. They are determined to be 1.8° for the series stages as they contain the same crossover type and 1.94° for the last stage. C_{uth} denotes the tangential velocity imparted to the flow by the volute, while $r_{z,eff}$ denotes the effective radius, to take into account the cross section between the volute surface and the inlet of the runner. C_{u2} is the tangential velocity at the interface. The expressions for these calculations are already shown in section 2.5. The calculation results for the throat-volute region, for the throat area of the design configuration,

are shown in table 4.3. Due to a larger $r_{z,eff}$ for the last stage as shown in table 4.3, the tangential velocity at the inlet of the runner is higher than the series stages. The comparison between tangential velocities for the three crosssectional throat areas are shown in figure 4.10. The effect of the change in the interface velocities on the performance in discussed in chapter 5.

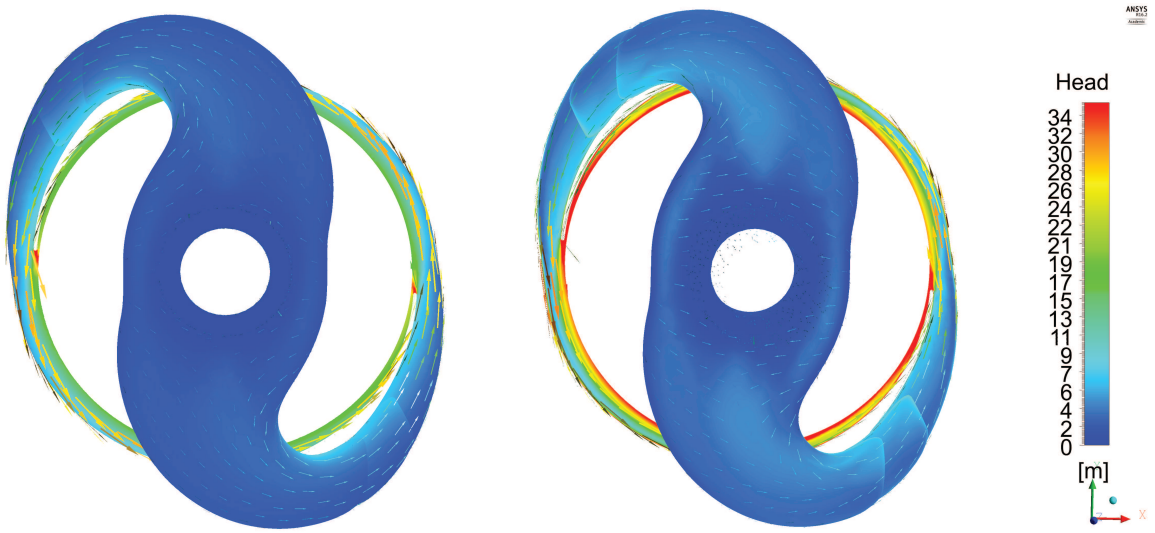

(d) Design Throat Area. H = 20m.

(e) Smaller Throat Area. H = 26m.

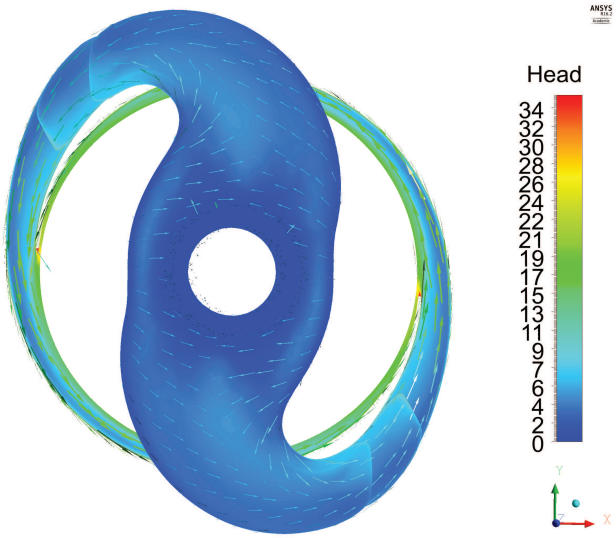

(f) Larger Throat Area. H=14.5m.

Figure 4.9: CFD head drops for different configurations at Q = 165m^3/hr.

Parameter	Series stage (Design)	Last stage
α_{th} (°)	1.8	1.94
C_{uth} (m/s)	32.45	32.44
$r_{z,eff}$ (m)	0.17	0.15
C_{u2} (m/s)	34.30	37.84

Table 4.3: Volute clearance calculations for Q=165m^3/hr

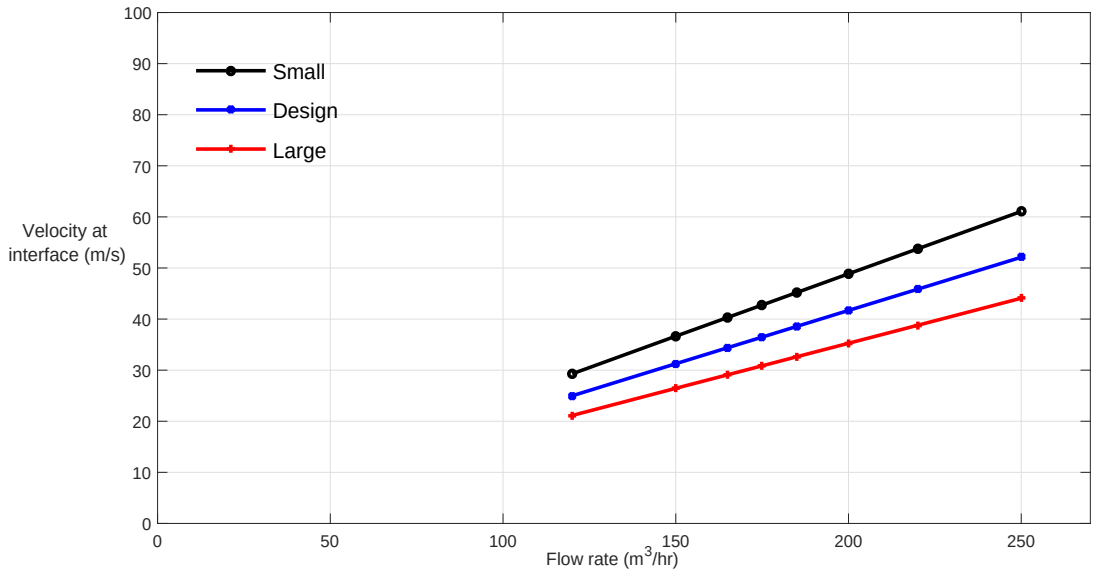

Figure 4.10: Tangential velocities at the interface.

4.2.2. Modeling the volute interface

An estimate of the contribution of the throat section alone to the head drop would give us a closer model to understand the flow at the volute interface. This can be done by neglecting the influence of the runner to the change in flow parameters at the interface. It would also give us an idea of how the interface can be possibly modeled in 1D. Hence CFD simulations of the crossover alone, eliminating the rotor are performed as the next step for the same range of flow rates. The crossover used for the series stage simulations is meshed with almost the same settings as explained in section 3.5. The number of elements in the mesh is around 1.1 million. The setup is simulated for a series of flow rates to understand the contribution of the cut-water to the head drop. The comparison of 1D average velocities obtained at the throat and at the interface with the corresponding CFD results, are shown in table 4.4. The results are shown for the three throat area configurations, for a flow rate of $165 m^3/hr$. It can be seen that the 1D calculations agree well with the CFD values for the velocity at the throat, inspite of the small deviation. This is due to the influence of the curved geometry of the pipe before the fluid reaches the throat. There is a slightly higher deviation between the CFD and the 1D values at the interface. This is because, the flow between the exit of the throat and the interface is highly three dimensional, and a 1D prediction has the limitation of not capturing every detail in the flow. Transient results and extensive study on the throat-volute interface is therefore needed to improve the prediction. The modeling of the interface is completed with the calculation of the inlet conditions of the runner. This is discussed in the next section.

	Design		**Large**		**Small**	
	CFD	**1D**	**CFD**	**1D**	**CFD**	**1D**
Velocity at throat(m/s)	32.03	32.45	26.49	26.32	38.42	38.61
Velocity at interface(m/s)	33.21	34.30	27.1	28.21	39.75	40.49

Table 4.4: Comparison of CFD and 1D results at throat and interface.

4.3. Runner modeling

After exiting the crossover, the fluid flows past the volute interface into the runner. The velocity at the volute interface has been determined in the last section. This section explains the calculations performed for the runner. The 1D head drop across the runner is calculated using the velocity triangles.

The volute interface is characterized by the incidence of the flow from the throat with the vanes. The interface is modeled using the frozen rotor or the mixing plane interface models. The mixing plane model circumferentially averages the flow properties and requires an exact matching of the areas at the interface. The errors increase as the distance between the interfaced domains increases [34]. With the frozen rotor interface model, the position of the wakes and secondary flows stay exactly the same. It performs the calculations for a fixed relative position of the runner with respect to the stationary domain. Hence the requirement of simulating a number of runner positions becomes inevitable for accurate prediction of the performance. However, since the performance of the turbine over a wide operating range is to be determined, the frozen rotor model, with its better representation of the secondary flows is preferred over the mixing plane model.

4.3.1. Inlet

To model the inflow to the runner, the blade/vane incidence should be considered as an important factor. Figure 4.11 shows a typical flow on the trailing edge of the blade in the PRT mode with the contours of the relative velocity vectors. In the case of a PRT, since the rotation of the runner is in the opposite direction, the incoming flow hits the blade at the trailing edge. Since the pump vanes are not designed for this mode of operation, the effects are pronounced on the trailing edge of the blade, as can be seen by the higher relative velocities. The tangential velocity of the fluid is shown by the black arrows in figure 4.11, while the red arrows show the absolute velocities of the fluid going into the runner.

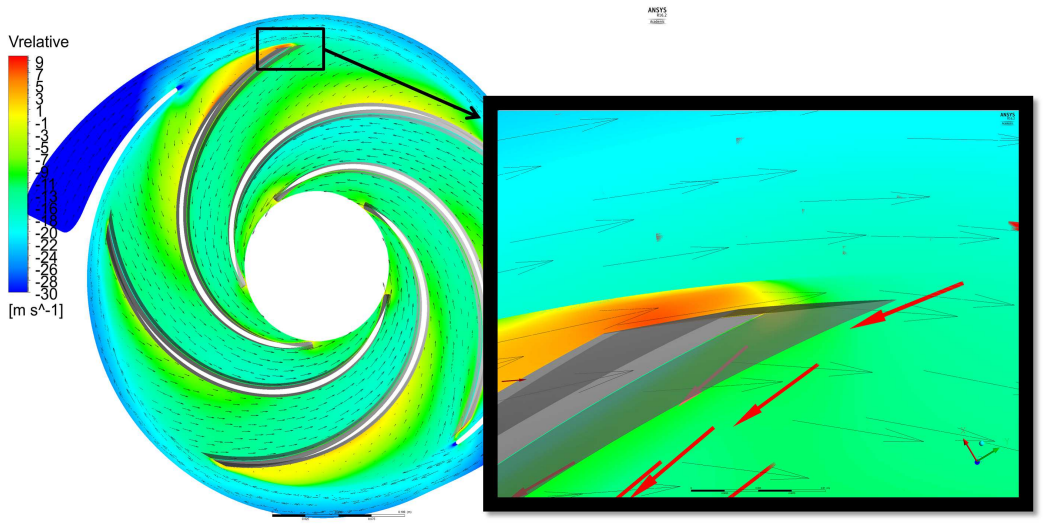

Figure 4.11: Incidence on a vane plotted with the relative velocity contour. The zoomed figure shows the absolute velocity (red arrows) and the tangential velocity (black arrows).

The velocity triangles for the PRT inlet are shown in figure 4.12. We can see that the conditions are different for the low and high flow rates. The velocity triangles have been derived with basic understanding, that the fluid pushes the blade on the pressure side of the pump vane, in accordance with Gulich [8]. The flow angle

α_2, is imparted by the volute and β_2 is the blade angle. Hence $\alpha_2$and β_2 are fixed. In the case of low flow rates, the tangential velocity component C_{u2} is smaller than the rotational velocity U_2. Since W_{u2} has a relatively small value, in that case, $C_{u2} + W_{u2} \neq U_2$. This means that the flow is impeded by the blade, but due to the low velocity of the incoming fluid, it is also slightly accelerated by the component $W_{u2}^{'}$, along the blade (due to the angle i, which completes the triangle). This component gets added to the tangential velocity C_{u2}, and the new tangential velocity is given by $C_{u2,new} = C_{u2} + W_{u2}^{'} - W_{u2}$ for the low flow rates, as seen from triangle 4.12A. But in the case of very high flows, the value of C_{u2} is greater than U_2. Hence the relative component $W_{u2}^{'}$ should be subtracted in the calculation from the tangential velocity C_{u2}, to account for the incidence on the vane. But the component $W_{u2}^{'}$ is either small or does not exist in 1D when $C_{u2} = U_2$. The influence of the impact of component $W_{u2}^{'}$ could not be estimated. Hence as a generalized interface correction, the incidence on the blade is incorporated by using the expression $C_{u2,runner} = C_{u2} - W_{u2}$. But the determination of the component $W_{u2}^{'}$ is critical, along with a better prediction of tangential velocities at the interface. The results obtained from this consideration in the analysis are found to be close to the actual performance of the PRT obtained from the test results. This indicated the velocity of the rotating blade has a significant impact on the head drop The results of the model without the incidence consideration and that with the incidence correction are validated with the test results in chapter 5. A validation with the result from CFD is shown in figure 4.16. It shows that this model under-predicts the head drop for lower flow rates, but gets better at higher flows. This might be due to the actual difference between W_{u2} and $W_{u2}^{'}$. They seem to become equal at higher flow rates. This could be a suitable 1D model for the interface, in the case of a pump with backward curved blades running as a turbine.

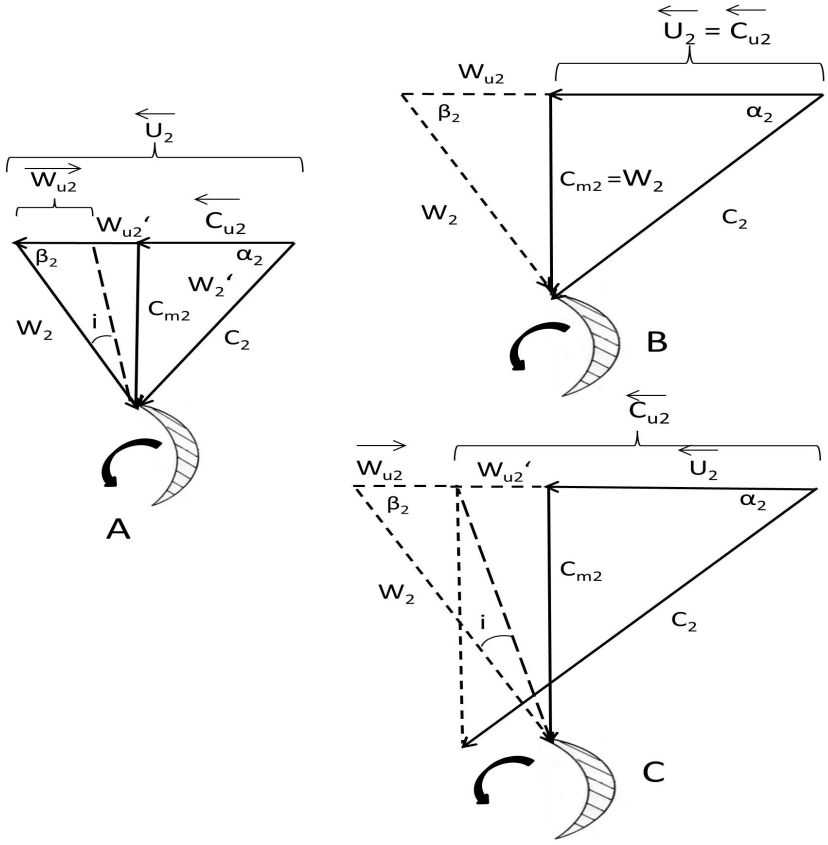

Figure 4.12: Inlet velocity triangles. A) Low flow ($C_{u2} < U_2$), B) Medium Flow ($C_{u2} = U_2$), C) High Flow ($C_{u2} > U_2$).

4.3.2. Outlet

The head drop obtained from the runner is calculated using the Euler equation, given by equation 2.37, where C_{u2}, C_{u1} are the inlet, outlet tangential velocities and U_2, U_1 are the runner rotation speeds at the inlet and the outlet respectively.

$$H_E = \frac{C_{u2}U_2 - C_{u1}U_1}{g}. \tag{2.37}$$

The swirl component at the outlet which corresponds to the tangential velocity is illustrated by the velocity vectors in figure 4.13. If $U_1 = r_1 \times \Omega_1$, the outlet tangential velocity is calculated as,

$$C_{u1} = U_1 - W_{u1}, \tag{4.1}$$

where W_{u1} is the tangential component of the relative velocity at the outlet, given as,

$$W_{u1} = \frac{C_{m1}}{tan\beta_1}. \tag{4.2}$$

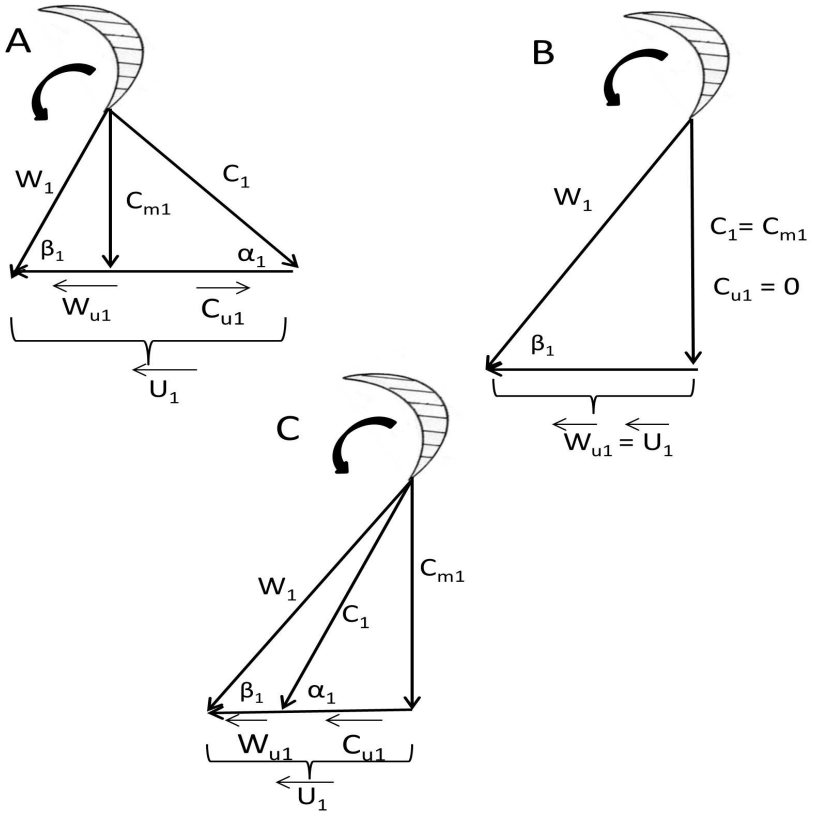

Figure 4.13: Inlet velocity triangles. A) Low flow (C_{u1} is opposite to U_1) B) Medium Flow (Radial outlet) C) High Flow (C_{u1} is along U_1).

Figure 4.14 shows the velocity swirl at the outlet for the three different configurations. The tangential velocity is opposite to the direction of the runner rotation for low flow rates. As the flow increases, the outflow from the blade becomes more radial and therefore, the tangential velocity decreases and changes direction. It can be seen as shown in figure 4.13C, that the tangential velocity changes direction at high flow rates, and acts along the direction of rotation of the runner. This is also seen in table 4.6. The negative values of the

outlet tangential velocity, according to equation 2.37, therefore contribute to an additional head drop. The 1D method from the velocity triangles can estimate the velocities only based on the geometry and the flow conditions. Hence the prediction for the swirl does not change for the three different configurations. The swirl is higher close to the blade in each case. The results for the outlet tangential velocity for the 5 vane series runner in the design configuration are shown in table 4.6.

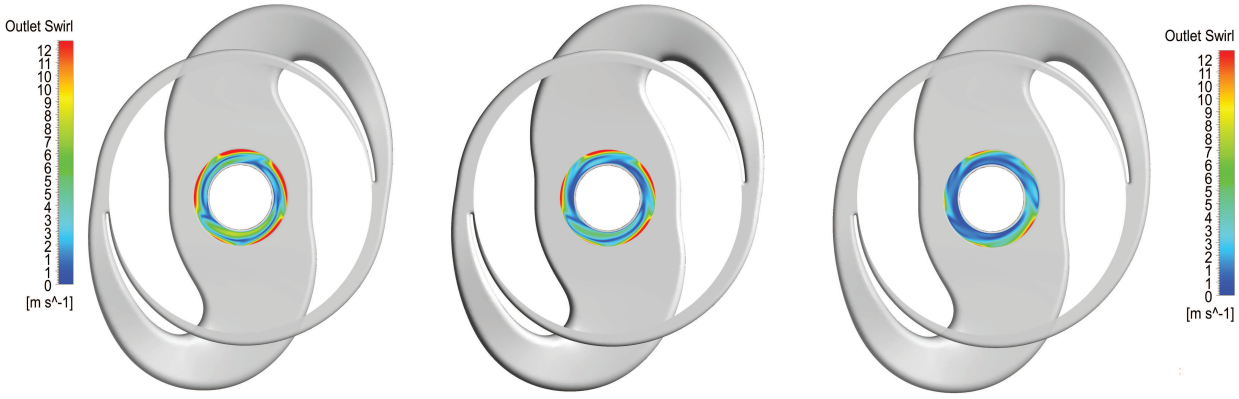

(a) Small (b) Design (c) Large

Figure 4.14: Outlet swirl representations.

	Swirl velocity component (m/s)	
	CFD	**1D**
Large	3.18	6.18
Design	4.35	
Small	5.31	

Table 4.5: Comparison of CFD and 1D outlet swirl for $Q = 165 m^3/hr$.

Flow rate(m^3/hr)	**Outlet tangential velocity - C_{u1} (m/s)**	
	Series stage	Last stage
120	9.36	9.76
150	7.27	7.24
165	6.18	5.99
175	5.54	5.15
185	4.84	4.32
200	3.80	3.05
220	2.41	1.38
250	0.32	-1.13

Table 4.6: Outlet tangential velocities.

The comparison of the results obtained from the 1D model with the results for the outlet obtained from CFD are shown in table 4.5 for a flow rate of $Q = 165 m^3/hr$. The 1D method gives a roughly good estimate of the swirl as well, which is incorporated into the Euler head equation.

4.3.3. Results

The results of the head drop across the components are consolidated for the 5 vane series stage in the design configuration, and are plotted in figure 4.15. The results here include the CFD head drops for the interface for a basic understanding of the requirement of a detailed interface model. This is obtained by the difference between the head drops of the full stage simulations and the simulations excluding the runner.

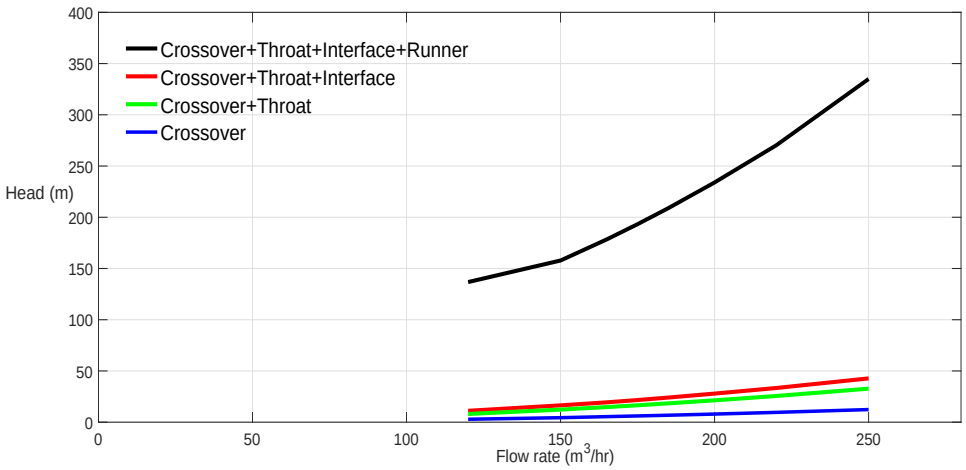

Figure 4.15: Comparison of head drops across different components in single stage (5 vane - design).

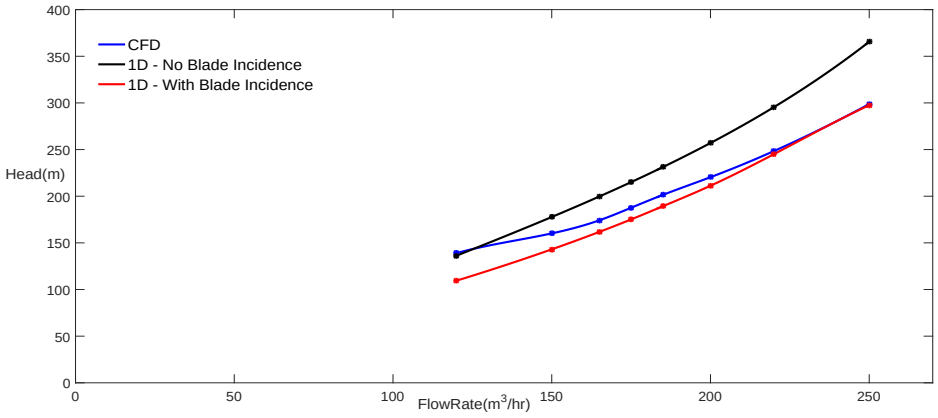

Figure 4.16: Comparison of head drops across runner for one series stage (5 vane - design).

It can be seen that when we exclude the head drop contribution by the runner in a single stage, the throat accounts for the highest head drop. The interface head drop obtained as mentioned above accounts for 3-4 % of the total head drop. Hence the 3D flow phenomena from the throat until the interface demands requires detailed research from the throat. Also a comparison of the head drops across the runner obtained from the model, with and without considering the correction for blade incidence at the inlet, with the results from CFD are shown in figure 4.16. We observe that the model without the blade incidence has a large deviation from the values from CFD, where the deviation for the model with blade incidence is way lesser, less than 6% for the operating range of 150 - 200 m^3/hr. The CFD results for the low flow rates are unstable, and hence a strange behavior is observed due to the unreliable prediction of hydraulic efficiencies from the steady state

simulations. Morever, the consideration of the inlet interface correction could also have an impact on the low flow rates. The values of the model with blade incidence also get closer to the CFD results at higher flow rates, and hence is used for the further calculations. This could be very well explained from the inlet velocity triangle. At low flow rates, the determination of the W'_{u2} is critical for closer results. This component becomes smaller and vanishes with lower flow rates and hence there is no correction to the tangential velocity needed at higher flow rates.

4.4. Stage Leak modeling

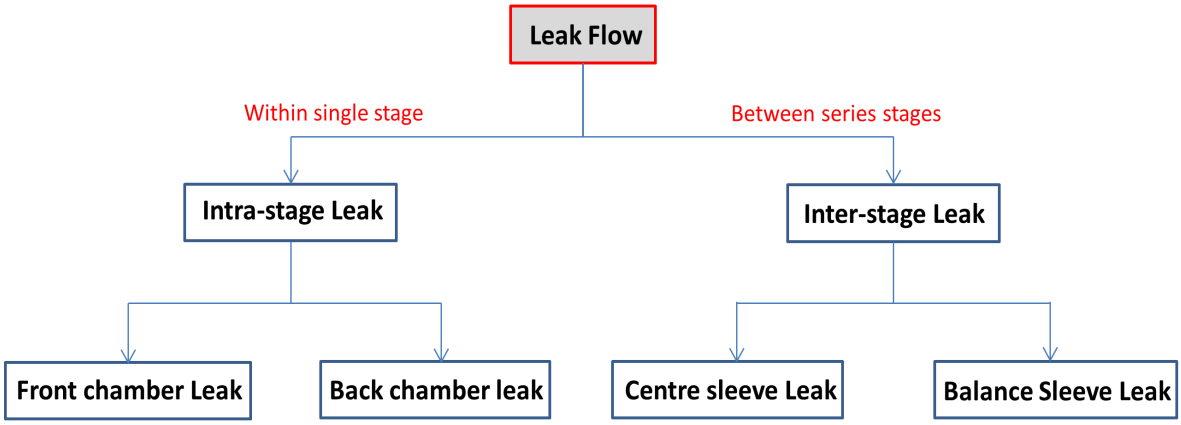

Figure 4.17: Leak flow classification

Leak flows reduce the power obtained from the PRT and the volumetric efficiency. The leaks can be classified as shown in figure 4.17. The leak flows can be classified as intra-stage and inter-stage leaks. The intra-stage leaks involve the leaks which occur within a single stage. They are the front chamber and the back chamber leaks. The inter-stage leaks are caused due to the center and the balance sleeves, through which leaks occur when the fluid flows from one series stage to the other.

Since we used CFD to simulate only a single stage in the pump, the leak flows are not incorporated in them. The leak flows are calculated based on rotor-stator cavity flow models. The results from the analytical model for the intra-stage leaks are discussed in this section. The inter-stage leaks will be discussed in the next section. The different stages of the multistage pumps along with the inter-stage leaks are illustrated in figure 4.18. Each of this stage is characterized by the intra-stage leaks. The intra stage leak can be understood from figure 4.19. The multistage pump contains a front and a back leak in each of the stages, with the following exceptions :

- The first stage of the PRT contains a radial inlet, with a front side chamber leakage, and a leak along the back side chamber, but in the opposite direction. This back leak contributes to the center sleeve leak indicated by the red arrows in figure 4.18.
- The first stage of the second series (denoted by S2S1 in figure 4.18), also has a radial inlet coming from the long crossover. It contains only a front side chamber leak, while the center sleeve leak comes into this stage through the back side chamber. Hence the flow through the runner of this stage is actually higher than the flow coming from the previous series stage through the long crossover.

- The last stage, which is a double suction impeller (in a pump) contains two front-chamber leaks.

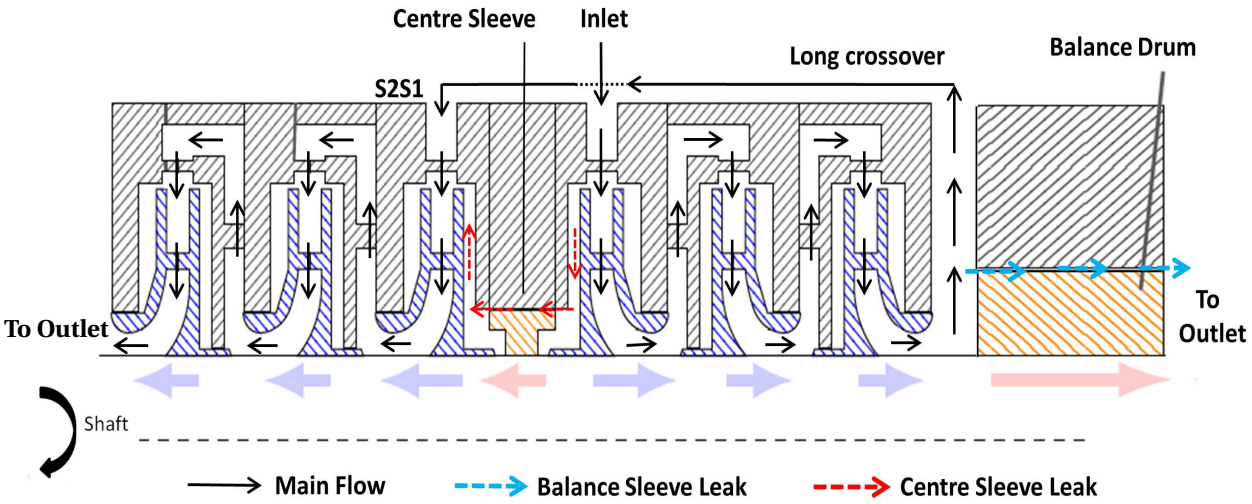

Figure 4.18: Multistage pump with inter-stage leaks

The inter-stage leaks can be explained as follows:

- The center sleeve leak is composed of a flow though the back chamber of the first stage, an axial seal leak, and a leak through the back chamber of the first stage in the second series. Hence the total head drop cross the center sleeve is a sum of all the three individual head drops. This is equal to head drop across the first set of series stages.
- The balance sleeve leak is only composed of an axial seal leak. The head drop across the balance sleeve is equal to the pressure drop across the stages in the second series and the last stage.

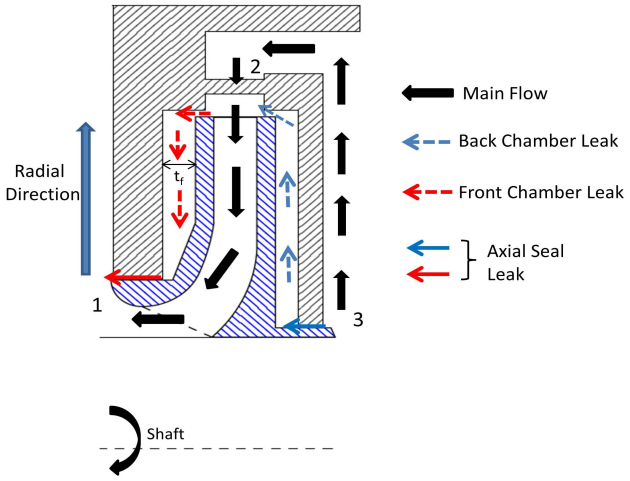

Figure 4.19: Illustration of single stage leak.

The model for the multistage PRT encompasses a combination of the intra-stage and the inter-stage leaks. The front and the back chamber leaks are a combination of the flow through a side chamber and an axial seal as shown in figure 4.19. The front leak flow in a single stage is driven by the total pressure difference between the interface and the exit of the runner. The back chamber leakage is driven by the difference between the total pressure of the fluid at the inlet to the stage and the end of the cutwater, at the volute interface. The inputs to the model are therefore the 1D head or the pressure drops at locations as mentioned above. These head drops are corrected with the hydraulic efficiency obtained from the CFD. The inter-stage leaks are also determined using the same side chamber and axial seal models, based on cumulative head drops from series

stages. They are explained in detail in section 4.5. The parameters which define the leak flow behavior are discussed further in the upcoming section.

4.4.1. Parameters and Coefficients

The modeling of the leak flow is done with the following parameters:

- G, the ratio of the side chamber width, t_f and the outer runner radius, r_2

$$G = \frac{t_f}{r_2}. \tag{4.3}$$

- The non-dimensional radius $\vec{r} = r/r_2$.
- The non-dimensional leak flow rate φ_g, given by equation 2.64.

$$\varphi_g = \frac{q_f}{\pi \Omega r_2}. \tag{2.64}$$

- The core-rotation factor or the entrainment coefficient, $k_f = V_{uf}/r\Omega$.

According to equation 2.58, we see that the pressure varies radially, across the whole chamber.

$$\frac{\partial p}{\partial r} = \rho r k_f^2 \Omega^2 + \frac{\rho q_f^2}{4\pi^2 t_f^2 r^3}. \tag{2.58}$$

The leak flow q_f is initially assumed, and all the other parameters are known from the dimensions. The core rotation factor, k_f also varies radially and is given by two methods, using the friction factors or not. They are given by equations 2.62 and 2.68 (which were discussed in chapter 2) respectively as,

$$\frac{dk_f}{d\bar{r}} = \frac{\bar{r}^2}{4\varphi_g}\left(f^* \lambda_S k_f^2 - \lambda_R (1-k_f)^2\right) - \frac{2k_f}{\bar{r}}, \tag{2.62}$$

$$\frac{dk_f}{d\bar{r}} = \frac{0.079\bar{r}^{8/5}}{\varphi_g Re_\phi^{1/5}}\left(\left(\frac{1-k_{f0}}{k_{f0}}k_f\right)^{7/4} - \left|1-k_f\right|^{7/4}\right) - \frac{2k_f}{\bar{r}}. \tag{2.68}$$

The difference between the two equations is that equation 2.62 accounts for different friction factors on the rotor and the stator. In most literature, the Blasius law is used for determining the wall stresses. But this method has its disadvantages that the shear stress in the viscous sublayer goes to infinity and hence there arises a discontinuity in the middle of the pipe, according to Will [18]. Will proposes an approach based on the logarithmic law of the wall. The logarithmic law of wall is a self similar solution to the mean velocity parallel to a solid wall. This approach uses two constants A^* and B^*. Will states that the Von Kármán relation for the friction factor in smooth pipes and channels, given as,

$$\frac{1}{\sqrt{\lambda}} = A^* lg\left(Re\sqrt{\lambda}\right) - B^*, \tag{4.4}$$

can be used, where $A^* = 2.03$ and $B^* = 0.8$. They are used for the calculations in equations 2.65 and 2.66. These require values for the stator and the boundary layer thicknesses δ_S and δ_R, which are given by,

$$\delta_S = A^+ \frac{a_1}{a_2}\frac{(1-k_f)^{\frac{12}{5}}}{k_f}\frac{r}{Re_l^{0.2}} - \frac{\varphi_g}{C^+ a_1 2\pi r^2 \Omega k_f}, \tag{4.5}$$

.

$$\delta_R = A^+ \frac{r}{Re_l^{0.2}} (1 - k_f)^m. \tag{4.6}$$

The various coefficients used in equations 4.5 and 4.6 are given according to Will[18] as $A^+ = 0.3035$ (proportionality constant) and C^+=0.408. The velocity factors a_1 and $a_2$are determined from empirical relations of Kurokawa and Sakuma [37] as,

$$a_1 = 1.03\left(\frac{Re_l}{10^5} + 2\right)^{-0.387}, \tag{4.7}$$

$$a_2 = 1.18\left(\frac{Re_l}{10^5} + 2\right)^{-0.49}, \tag{4.8}$$

based on flow angle measurements for regime 4 (shown in figure 2.11 in chapter 2). The flow can be oriented in the centrifugal (hub to casing) or the centripetal (casing to hub) direction [38]. In the case of centripetal flow, the leak flow rate is negative, when used in equation 4.5 to determine the stator boundary layer thickness.

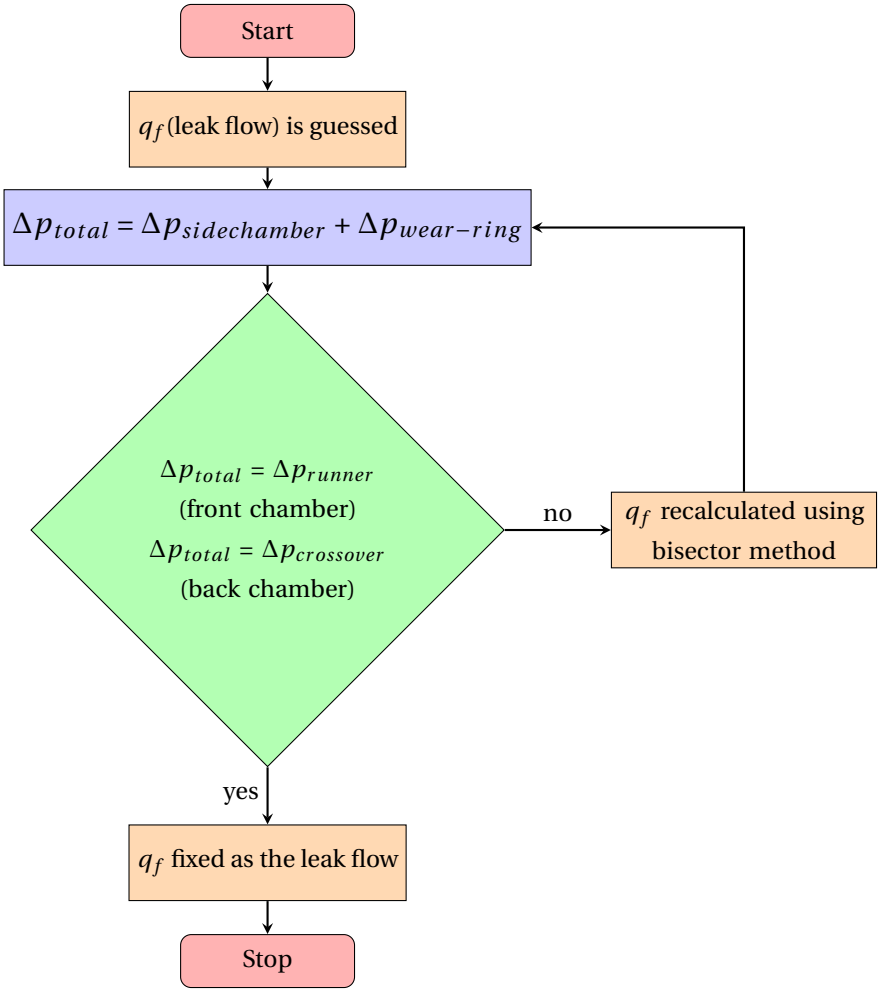

Figure 4.20: Flowchart to determine intra-stage leak flow

4.4.2. Analytical Method

Equations 2.62 and 2.68, which estimate the variation of core rotation coefficient with radius, need to be solved to estimate the leak flow. We need an iterative method, to solve for k_f in each step. If the friction factor modification is used, we have an additional equation to be solved due to the dependence of λ_S and λ_R on k_f, and λ_S, λ_R from the previous step. Hence, the determination of friction factors also requires an iterative cycle. The fourth order explicit Runge-Kutta method is used for solving the differential equation. The flowchart of the methodology used is described in figure 4.20.

The methodology to estimate the front chamber leak flow is explained here. In this method, a leak flow of 5% the total flow is assumed, an average based on the leak flow occurring in the pump (data obtained from Flowserve). A minimum and maximum value is initialized to the leak flow to begin the iteration. The 1D head drop between the interface and the outlet of the runner, corrected with the CFD hydraulic efficiency, is taken as the initial condition for the model. The inlet loss to the side chamber is estimated, as shown in section 2.7.1. To estimate the side chamber head loss, the equation for the core rotation coefficient needs to be solved iteratively in the radial direction. Since there is a centripetal flow in the front side chamber, the leak flow has a negative sign in the model. The side chamber is divided into 5000 parts in the radial direction according to the guidelines from Li's model [21]. The core rotation coefficient corresponding to the entrance tangential velocity of the fluid C_{u2}, is taken as the initial boundary condition. The thickness of the stator and rotor boundary layers, δ_S and δ_R, and thus the rotor and stator resistance coefficients, λ_S and λ_R are explicitly calculated with the k_f value, for each of the 5000 parts.

Inlet Tangential Velocity (m/s)	**Leak Flow (% of Total Flow)**		**Deviation(%)**
	No Friction Factors	**Friction Factors**	
20	2.64	2.58	2.26
25	2.63	2.56	2.51
30	2.61	2.53	2.99
35	2.59	2.52	2.74
40	2.57	2.51	2.26

Table 4.7: Comparison of friction resistance models, G = 0.093, φg=0.0003

4.4.3. Front Chamber Leak Estimation

This section explains from the front chamber leak estimation as shown in figure 4.20. The comparisons for the leakage flow in the rotor-stator cavities of the PRT are done as discussed by Will [18], [21] similar to that of the centrifugal pumps. They include assessing various leakage flow rates (φ_g), side chamber gap widths (G) and entrance rotation coefficients (k_{f0}) as shown in equation 2.69. Table 4.7 shows the comparison of the leak flows calculated without the friction factors and with them, according to equations 2.62 and 2.68 respectively. The deviation observed between the results is quite small. Hence, the model without the friction factors is used to estimate the leak flows, considering the advantage of a lower computation time. The relevance between the model for the pump and that for the PRT is that, in spite of the reversed flow direction in the PRT, the leakage flows occur in the same direction as that of the pump (centripetal direction in the front chamber, and centrifugal direction in the back chamber [21]). Hence the model is validated against flow models of Möhring and Kurokawa [37] for the rotor cavities, as discussed by Will [18]. The comparison, shown in figure 4.21 also includes a set of experimental data from Will [39] with the parameters as :

- The non-dimensional leak flow rate φ_g = 0.0003,
- Three different side chamber axial widths, G = 0.027, 0.093, 0.227.
- The corresponding entrance rotation coefficients are k_{f0}=0.54, 0.55 and 0.45 respectively for the three comparisons with different axial gap widths.

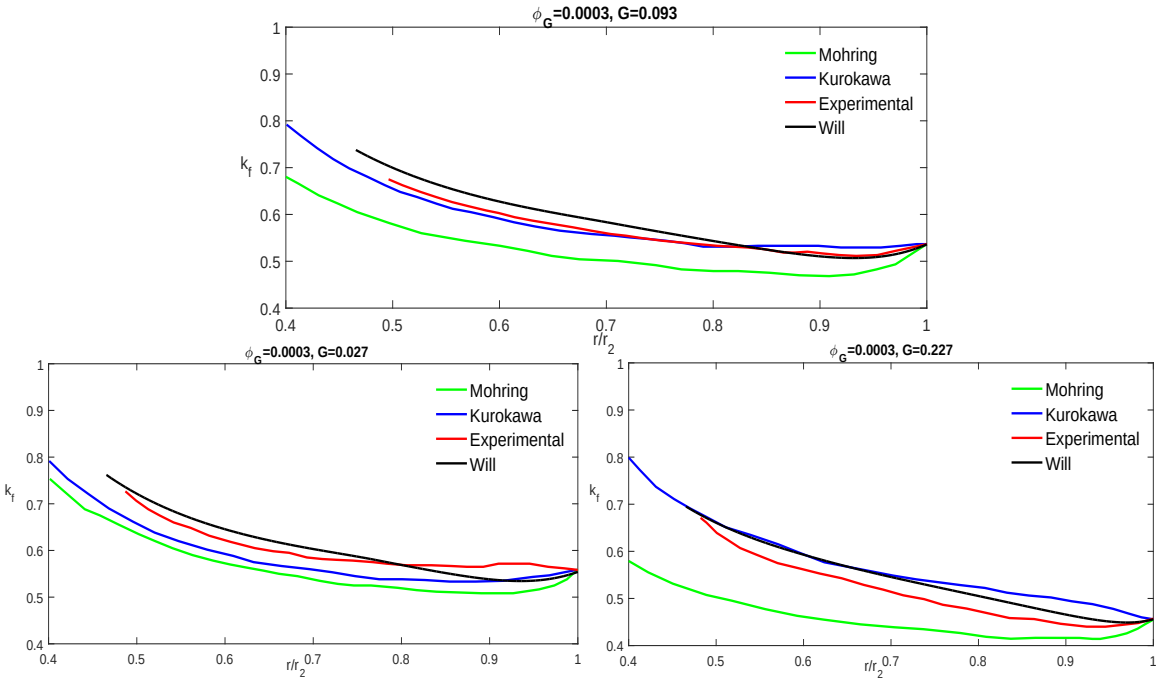

Figure 4.21: Comparison of leak flow model with literature and experimental data

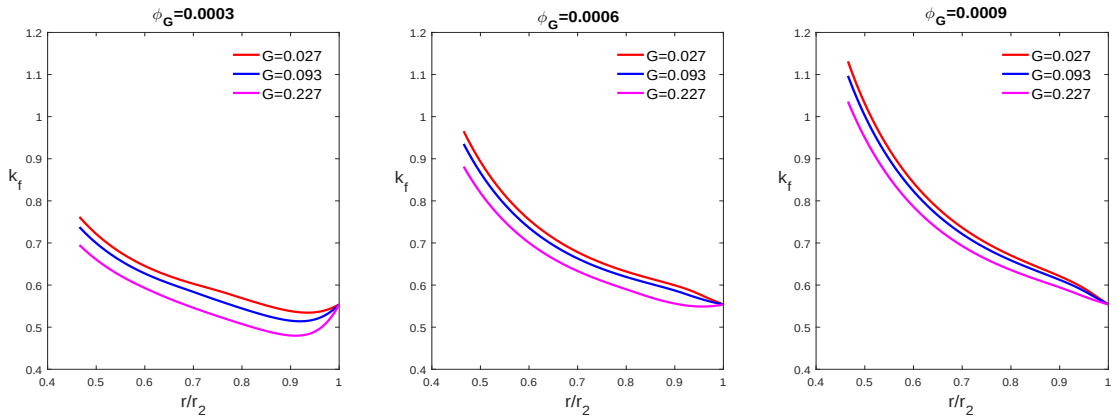

Figure 4.22: Core rotation coefficient behavior for different leak flows.

It can be seen from figure 4.21 that the results from the model agree qualitatively with the experimental data, with a deviation of 3-5%. Since the φ_g values in the PRT models discussed in this thesis are around 0.05, the leak flows have been predicted with this leak model throughout all the stages. For $k_f = V_{uf}/r\Omega < 1$ at

the entrance, the rotation of the fluid is lesser compared to the angular velocity of rotation of the rotor. To satisfy the no slip condition, the rotor tries to set the fluid to rotate at the same angular velocity as itself. Hence we see an increase in the core rotation coefficient inward along the radial direction. Figure 4.22 shows the variation of the entrance rotation coefficients in the radial direction for different leak flows, with the same entrance rotation coefficients. For the same rotational speed of the rotor and leak flow, the fluid is accelerated more with an decrease in the gap width. The acceleration is also more for higher leak flow rates, and the fluid begins to rotate at an angular velocity higher than that of the rotor, at even higher radial positions. An initial decrease in core rotation is observed for φ_g =0.0003, after which the core rotation increases. This effect is magnified for larger side chamber widths. Figure 4.23 shows the core rotation behavior with different values of inlet rotation ($k_f 0$).

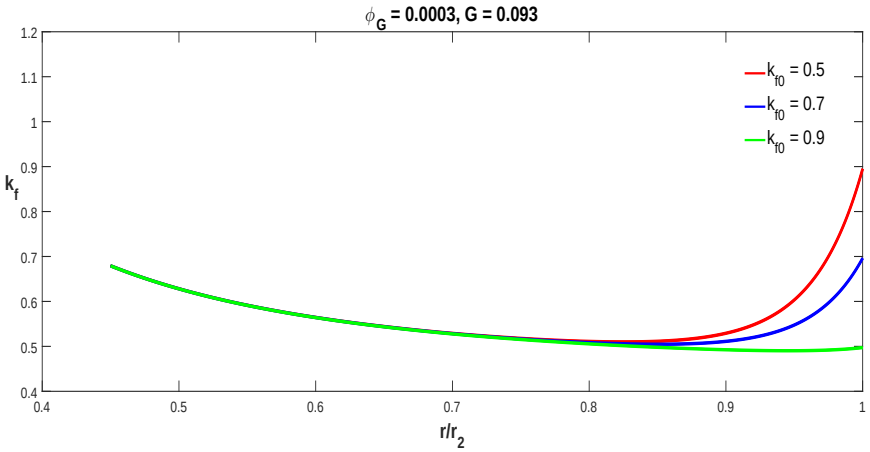

Figure 4.23: Core rotation coefficient behavior for different front chamber entrance rotation coefficients.

In the case of high inlet rotation, the entering flow is strongly decelerated at the outer radius, and then the core rotation increases towards the inner radius. This is due to the influence of the boundary layer on the side of the casing (stator boundary layer). It is observed from the model that both the stator and the rotor boundary layer thicknesses (given by δ_S and δ_R respectively), increase initially when fluid enters the side chamber. But the magnitude of increase of δ_S is greater than that of δ. Hence the stator boundary layer has a greater impact on the leak flow pressure variation than its rotor counterpart. This is because, due to its rotation, the fluid which enters the side chamber impinges on the casing wall and gets separated from it. This causes a greater increase in the stator boundary layer thickness. Whereas on the rotor side, the increase is more gradual. Hence, it can be understood from figure 4.23, that this influence is magnified for the fluid coming in with a higher rotation, and the velocity and core rotation are reduced. As the fluid moves down the side chamber, the stator boundary layer increases until a point, and then starts to gradually decrease causing an increase in the velocity at lower points in the radial direction. The rotor boundary layer on the other hand, initially increases until a certain point, and then decreases gradually. But towards the end of the side chamber, it starts increasing , thereby pushing the fluid more towards the stator side. This thereby causes an increased magnitude of reduction in the stator boundary layer thickness, causing a greater increase in the velocity or the core rotation towards the end of the side chamber.

The dimensions of the side chamber and the wear-rings that are used to model the stage leak flows are given in table 4.8. The axial seal pressure drop is estimated as explained in section 2.7.2. With the total pressure drop of the side chamber and the axial seal, the leak flow for the front side chamber are estimated. The leak flows for the 5 vane, 3 vane and the last stage of the pump are shown in tables 4.9, 4.10 and 4.11

respectively. It can be seen that the leak flow increases for smaller cutthroat areas. This is because of the higher pressure drop across the runner driving the flow, and higher velocity of the water at the entrance to the runner. Hence more leakage happens through the front chamber. The leak flow in the case of the 3 vane runner is also slightly higher than that of the 5 vane runner stage, in spite of being enclosed by the same crossover. The 1D head across the runner used as the input to the leak flow estimation is corrected with the efficiency obtained from CFD. This difference in the leak flow is therefore attributed to the varied efficiencies of the 3 vane runner and the 5 vane runner, as seen in figure 3.13. The last stage, on the other hand has two leak flow paths similar to the the front side chamber. The leak flow results are shown in table 4.11. The leak flow is therefore twice the values shown in the table 4.11.

	Series stages		**Last stage**	
	Front	Back	Front	Back
Side chamber width, t_f (mm)	8.31	8.54	5.34	-
Wear-ring clearance, s (mm)	0.30	0.30	0.33	-
Wear-ring length, $l(mm)$	23.81	19.05	20.5	-
Outer radius of runner, r_2 (mm)	161.11	161.11	130.20	-
Dimensionless side chamber width, G	0.05	0.05	0.04	-

Table 4.8: Dimensions of the stage leak paths

FlowRate(m^3/hr)	Front chamber leak (% of Total flow)		
	Small	Design	Large
120	10.77	9.32	8.00
150	10.03	8.83	7.75
165	9.70	8.58	7.59
175	9.50	8.42	7.48
185	9.31	8.28	7.38
200	9.08	8.08	7.25
220	8.80	7.86	7.12
250	8.52	7.63	7.02

Table 4.9: Front chamber leak flows for 5 vane runner stage for different throat areas.

FlowRate(m^3/hr)	Front chamber leak (% of Total flow)		
	Small	Design	Large
120	11.22	9.78	8.54
150	10.31	9.26	8.22
165	9.90	8.99	8.02
175	9.66	8.81	7.89
185	9.44	8.64	7.76
200	9.13	8.41	7.59
220	8.80	8.13	7.39
250	8.43	7.80	7.18

Table 4.10: Front chamber leak flows for 3 vane runner stage for different throat areas.

4.4.4. Back Chamber Leak Estimation

The back chamber leak modeling is done similar to the front chamber, except that in this case the leak flow is driven by the pressure difference between the inlet to the stage and the interface between the volute and

FlowRate(m^3/hr)	Front chamber leak (% of Total flow)
120	13.25
150	10.89
165	10.55
175	10.34
185	10.02
200	9.685
220	8.92
250	8.10

Table 4.11: Front chamber leak flows for last stage

the runner. This leak flow is also characterized by an axial seal and the side chamber. The inlet boundary condition is the core rotation coefficient, determined by the averaged tangential velocity at the outlet from the previous stage. The variation of the core rotation coefficient in the radial direction for different entrance rotation coefficients is shown in figure 4.24. In contrast to the front leak chamber, the core rotation coefficient increases with an increase in radial position. But the back chamber leak is much lesser compared to the front leak, because the leak is driven by a smaller pressure difference (between the inlet and the interface) than the pressure difference due to the runner. This can be seen from table 4.12, where the dashes denote really low back chamber leak flows less than 1% of the total flow. The leak increases with an increase in the total flow rate and also with an decrease in the area of the throat, which cause higher head drop across the crossover, throat and the interface.

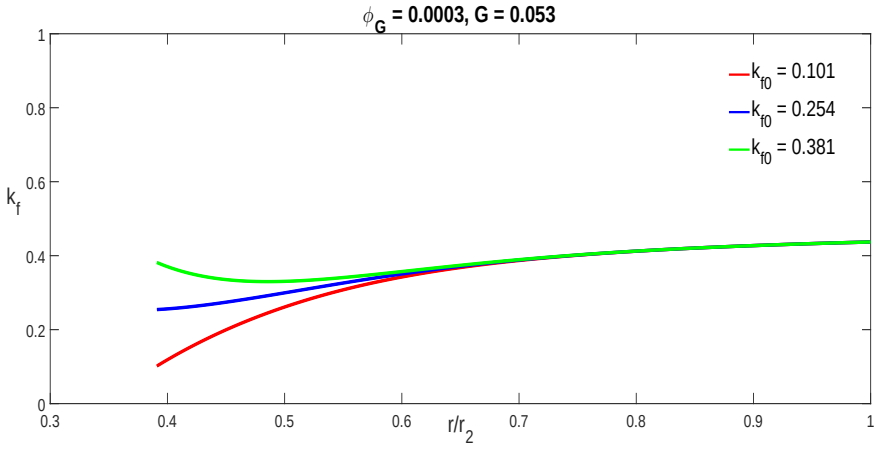

Figure 4.24: Core rotation coefficient behavior for different back chamber entrance rotation coefficients.

4.4.5. Leak Flow Contributions

In this section the comparison of the leak flow is done between the axial seals and the side chamber. The contribution from the inlet to the chambers are also considered. The axial seal leakage is governed by the Reynolds number of the flow, the axial seal clearance(s) and the length of the seal(L_s) as discussed in section 2.7.2. Tables 4.13 and 4.14 show the leak flows across the front and the back chamber respectively.

They show the pressure drops across the seal and the chamber separately in terms of contribution to the total pressure drop. The values are for an axial gap width, G = 0.053. The split up gives a better understanding

FlowRate(m^3/hr)	Back chamber leak (% of Total flow)		
	Small	Design	Large
120	-	-	-
150	-	-	-
165	1.46	-	-
175	1.97	-	-
185	2.28	1.00	-
200	2.59	1.78	1.41
220	2.86	2.21	1.96
250	3.12	2.53	2.34

Table 4.12: Back chamber leak flows for 3-vane and 5-vane runner stages.

FlowRate	**Pressure ($\times 10^5$ Pa)**				**Contribution (%)**		
(m^3/hr)	**Inlet**	**Side chamber**	**Axial seal**	**Total**	**Inlet**	**Side chamber**	**Axial seal**
150	0.0024	5.50	9.50	15.00	0.02	36.66	63.32
200	0.0034	7.96	13.11	21.07	0.01	37.79	62.20
250	0.0047	11.66	17.28	28.94	0.01	40.29	59.70

Table 4.13: Pressure drop split up - Front Chamber Leak, G=0.053

of the leak flow behavior. In every case of the front chamber leak, as seen in table 4.13, the contribution of the axial seal is greater than that of the side chamber. For the back chamber, almost the same behavior is observed, except that the side chamber pressure drop predominates that of the axial seal for low flow rates. From table 4.12, we see that the back flow itself is small and negligible for low flow rates. Hence this behavior is of less significance in determining the performance of the PRT. A quantitative comparison and elaboration with the inter-stage leaks is done in section 4.5.4.

FlowRate	**Pressure($\times 10^5 Pa$)**				**Contribution (%)**		
(m^3/hr)	**Inlet**	**Side chamber**	**Axial seal**	**Total**	**Inlet**	**Side chamber**	**Axial seal**
200	0.0013	1.16	1.12	2.28	0.05	59.75	49.20
220	0.0024	1.40	1.83	3.23	0.07	43.36	56.57
250	0.0043	1.22	2.90	4.12	0.01	29.56	70.33

Table 4.14: Pressure drop split up - Back chamber leak, G=0.053

4.5. Inter Stage Leak Modeling

The multistage PRT is of the opposed runner design. Each runner in a multistage PRT creates a force in the axial direction. The advantage of the opposed runners is that these forces counteract each other resulting in a much lower force. But there is still a requirement of a device to compensate the forces which are produced. This is done by using the balance drum, present of at the end of the first five stages. The series stages in the opposed impeller design are connected by a center sleeve. Leakage happening through both the center and the balance sleeves causes a reduction in the head drop that can be obtained from the PRT. The center and the balance sleeve leaks together are know as the inter-stage leaks. This section explains the methodology adopted to estimate these leaks.

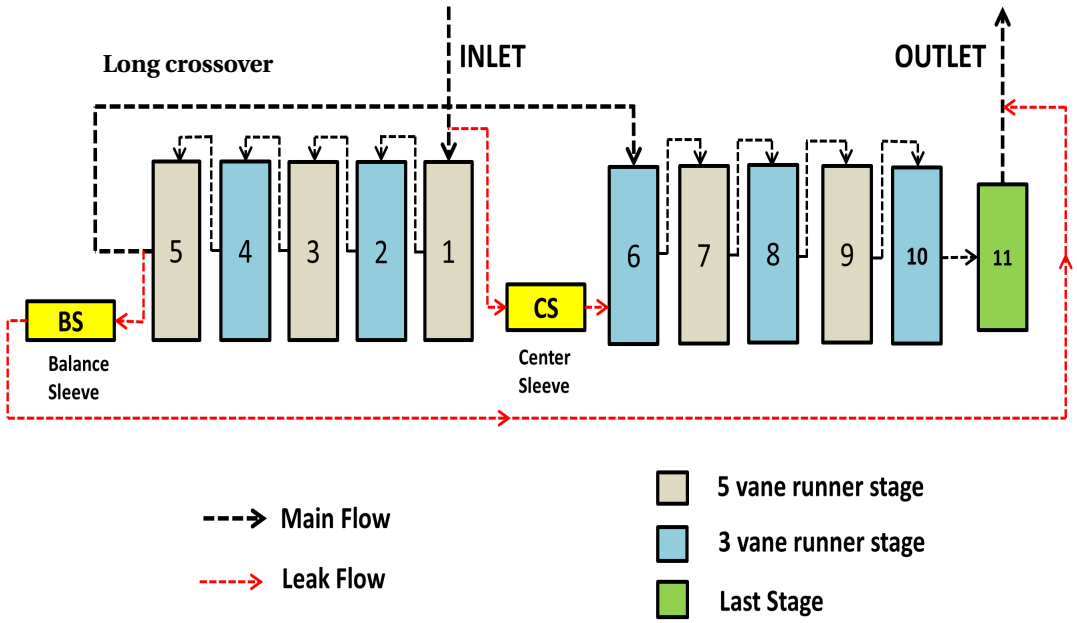

Figure 4.25: Schematic of a multistage pump with leak flows

4.5.1. Methodology

The simplified setup of the multistage pump in the turbine mode, studied in this thesis, is shown in figure 4.25. The inter-stage leaks can be explained from the figure as follows:

- The center sleeve leak is driven by the difference between the pressure of the fluid at the inlet of the first stage, and the pressure of the fluid at the inlet of stage 6. Hence the center sleeve leak, reduces the flow through the first five stages.
- The balance sleeve leak is driven by the difference between the pressure of the fluid at the exit of the 5th stage and the pressure of the fluid at the outlet of the PRT.

The methodology to calculate the head drop across the entire PRT is split into two parts. The first part is the estimation of the center sleeve leak, to calculate the head drop across stages 1-5. The second part is the estimation of the balance sleeve leak to determine the head drop across stages 6-11. An iterative procedure is required for these parts, because of the interdependence of the center sleeve leak and the head drop across the first five stages on each other. The stepwise methodology is explained in flowchart 4.26. The following nomenclature is used to explain the modeling of the inter-stage leaks :

- H_{set1} - Head drop across first five series stages, which are alternatively 5-vane and 3-vane stages.
- H_{set2} - Head drop across series stages 6-10, which are again alternatively 5-vane and 3-vane stages, and the last stage. The flow from stage 5 has a balance leak which goes directly to the PRT outlet. The remaining flow comes to stage 6 through a long crossover.
- Q - Total flow through the PRT.

- Q_{CS} - Leak flow across the center sleeve.
- Q_{BS} - Leak flow across the balance sleeve.
- $Q_{eff,set1}$ - Effective flow across stages 1-5. It is given by,

$$Q_{eff,set1} = Q - Q_{CS}. \tag{4.9}$$

- $Q_{eff,set2}$ - Effective flow across stages 6-10 and the last stage. It is given by,

$$Q_{eff,set2} = Q - Q_{BS}. \tag{4.10}$$

4.5.2. Estimation of the center sleeve leak

The center sleeve leak reduces the flow though the stages 1-5. To begin the calculation, we assume that there is no leak through the center sleeve, and the entire flow Q, flows through the first five stages. The head drop is calculated for each individual stage as a sum of the head drops across the crossover, throat, interface and runner. They are combined and corrected with the hydraulic efficiency obtained from the CFD simulations. The front and the back chamber leaks are calculated iteratively for each stage according to section and the effective head drop across a stage is calculated after subtracting the leak flows. The net head drop, H_{set1} across the first 5 stages is determined by adding the head drops across the individual stages. As discussed in the last section, the center sleeve leak flow path is composed of a flow though the back chamber of the first stage, an axial seal flow, and a leak flow through the back chamber of the 6th stage. The combined head drop across the three leak paths is equal to the head drop across stages 1-5.The center sleeve leak, Q_{CS} is thus estimated using the value of H_{set1}, according to the methodology given in flowchart 4.20. The center sleeve leak is now subtracted from the total flow, and the new H_{set1} is calculated for the flow $Q - Q_{CS}$. The new head drop is then used to calculate the center sleeve leak, Q_{CS}. The iterative calculation is done until a convergence of $H_{set1}(i) - H_{set1}(i-1) < 1$ is achieved. Q_{CS} and H_{set1} are thus determined as the center sleeve leak, and the net head drop across stages 1-5 respectively.

4.5.3. Estimation of the balance sleeve leak

The flow through stages 6-11 as shown in figure 4.25 is obtained by the subtracting the balance sleeve leak and adding the center sleeve leak from stage 1. Similar to the estimation of the center sleeve leak, we assume that there is no leak through the balance sleeve to begin the calculation. Since the leak through the center sleeve enters stage 6, the entire flow, Q is initially assumed to flow through stages 6-11. The head drop across each stage is again calculated. The front and back leaks are again determined iteratively for each stage, with the exception that the last stage has two front chamber leaks for the twin runner and no back chamber leak.The effective head drop, H_{set2} is thus calculated subtracting the leak flows from the main flow, similar to the method described in the center leak estimation. The balance sleeve leak is only composed of a flow thorough an axial seal leak path. The head drop across the balance leak paths is equal to the head drop across stages 6-11. The important correction is that the balance sleeve leak, Q_{BS} needs to be calculated from the effective flow $Q_{eff,set1}$, across stages 1-5. $Q_{eff,set1}$ is given by equation 4.9. The balance sleeve leak is now subtracted from the total flow, and the new H_{set2} is calculated for the flow $Q - Q_{BS}$. The new H_{set2} is used to calculate the balance sleeve leak, Q_{BS}, from $Q_{eff,set1}$. The iterative calculation is done until a convergence of $H_{set2}(i) - H_{set2}(i-1) < 1$ is achieved. Q_{BS} and $H_{set2}$are thus determined as the balance sleeve leak, and the net head drop across stages 6-11.

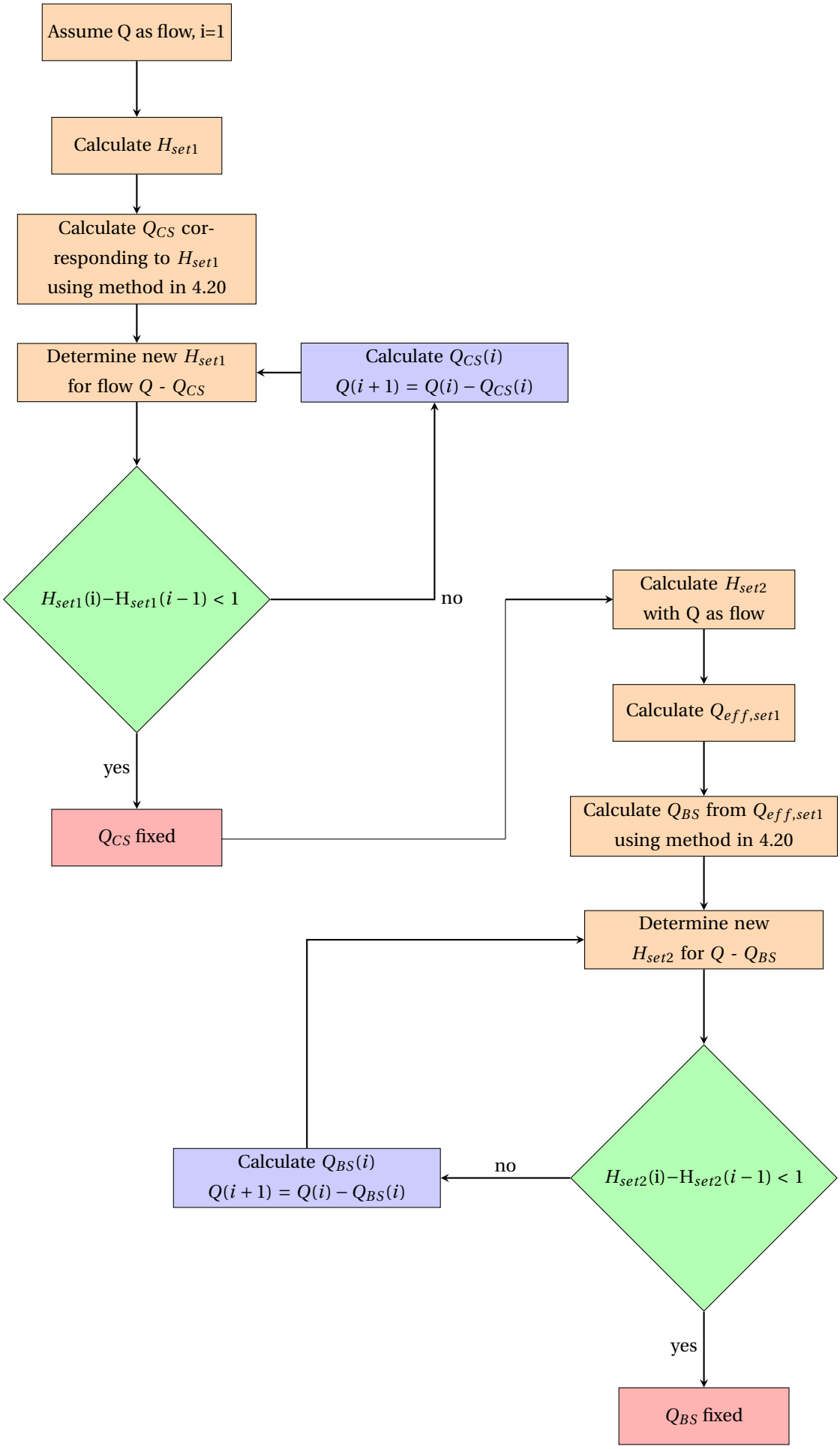

Figure 4.26: Flowchart to determine inter-stage leak flow

4.5.4. Results

This section describes the inter-stage leak results in terms of percentage leaks. The dimensions of the side chamber and wear-rings that are present in the center and the balance sleeves are given in table 4.15. The iterative steps discussed in sections 4.5.2 and 4.5.3 are performed to estimate the leaks across the center and the balance sleeves and to determine their effect on the overall head drop. The same steps are also carried out for the PRT setups with the smaller and larger throats in the series stages. Table 4.16 shows the center sleeve leaks obtained after convergence for the design, large and small throats, while the balance sleeve leaks are shown in table 4.17.

	Center sleeve		**Balance Sleeve**
	Stage 1	Stage 2	Front
Side Chamber Width, t_f (mm)	8.31	8.54	-
Wear-ring clearance, s (mm)	0.25		0.20
Wear-ring length, $l(mm)$	61.9		88.9
Outer radius of runner, r_2 (mm)	161.11	161.11	-
Dimensionless side chamber width, G	0.05	0.05	-

Table 4.15: Dimensions of the center and balance sleeves

FlowRate(m^3/hr)	Center sleeve Leak (% of Total flow)		
	Small	Design	Large
120	13.71	11.88	11.19
150	12.64	11.34	10.73
165	12.23	11.07	10.47
175	12.00	10.89	10.25
185	11.79	10.73	10.10
200	11.54	10.50	9.90
220	11.26	10.24	9.66
250	10.97	9.92	9.38

Table 4.16: Center sleeve leak flow results

FlowRate(m^3/hr)	Balance sleeve Leak (% of Total flow)		
	Small	Design	Large
120	8.96	7.94	7.57
150	8.39	7.45	7.21
165	7.91	7.24	6.91
175	7.77	7.11	6.78
185	7.65	7.00	6.67
200	7.51	6.84	6.45
220	7.37	6.67	6.32
250	7.24	6.47	6.15

Table 4.17: Balance sleeve leak flow results

The results show that, similar to the intra-stage leak flow results shown in tables 4.9 - 4.11, the percentage leak flow decreases with an increase in throat area. From the behavior of the leaks it can be seen that in every case, the balance sleeve is less than the center sleeve leak, in spite of the higher head drop that governs it, due to 6 stages. The amount of effective flow through the first 5 stages is therefore less than the effective flow through stages 6-11. Hence the average head drop per stage is relatively higher in stages 6-11, than that of stages 1-5.

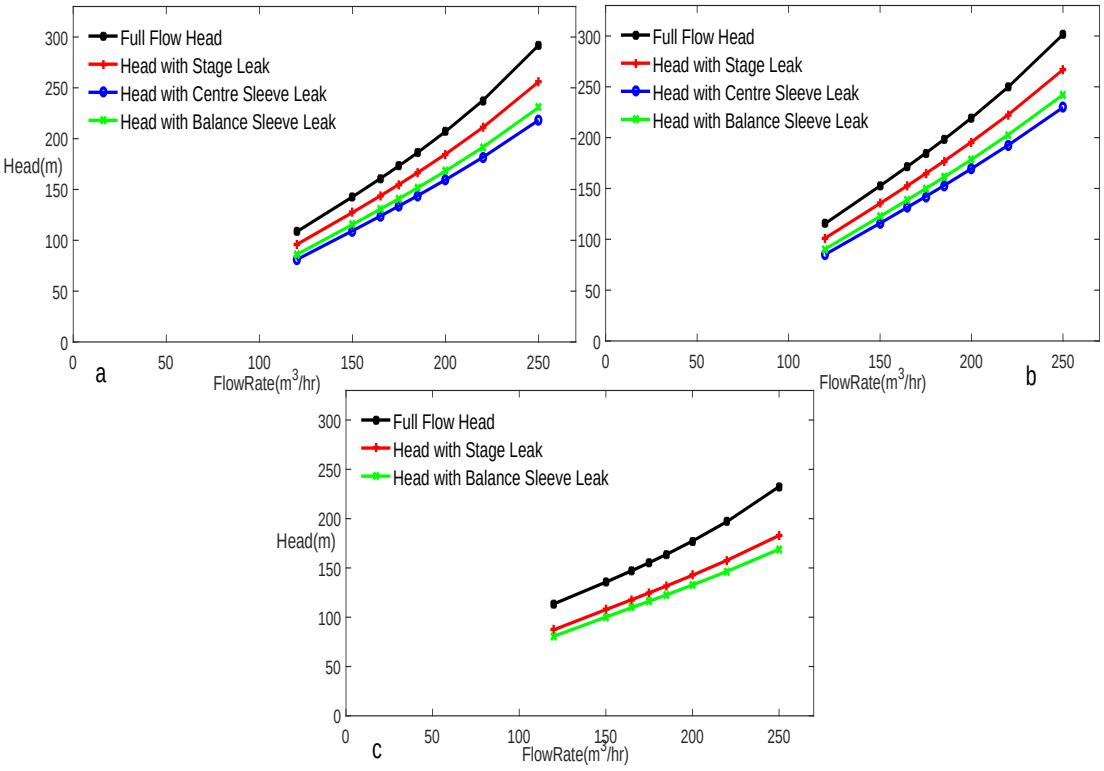

Figure 4.27: Head curves for single stages in the design configuration, considering the leaks. a) 5-vane runner stage b) 3-vane runner stage c) Last stage

Figure 4.27 shows the comparison of the head drops with and without considering the leaks for the three different types of stages present in the PRT. The curves are only shown for the design throat area configuration. It can be seen that the head drops obtained in the case of the series stages (5-vane and the 3-vane runners), shown by figures 4.27a and 4.27b are quite similar in terms of the relative difference between the head drop curves. Stage leaks involve the front and the back chamber leaks, though the back chamber leaks are close to insignificant to head drops occurring across the whole PRT. The center leak is calculated using the total head drop across the stages 1-5. Hence it includes the stage leakage losses. Similarly, the head drop curve considering the balance sleeve leak also includes the intra-stage leaks. It can be seen from tables 4.9 - 4.11, 4.16 and 4.17, that the percentage of leak flow decreases with an increase in flow rate, for both the intra-stage and the inter-stage leaks. Hence the percentage difference in the head drop also decreases with an increase in flowrate. The effect of the balance sleeve leak on the head drop is less than the center sleeve leak as discussed before. The last stage head curves are shown in figure 4.27c. Being the last stage, the center sleeve leak does not affect its performance. The last stage contains two front chamber leak paths, instead of one front and one back chamber, as in the other series stages. Hence the difference in head between the full flow, and the effective flow considering the stage leaks, is higher than that of the series stages.

4.5.5. Leak Contributions

The leak flows are modeled based on the head drops developed by multiple stages. The logic is that the leak flows head drops across all these stages and the leak paths are equal. Hence an analysis of the contributions of the different segments that make up the leak path is interesting from an engineering perspective, to make improvements in design. The center sleeve, as shown in figure 4.18, has two side chambers and one axial seal, with the dimensions in table 4.15. SC1 denotes the back chamber on stage 1 and SC2 denotes the back side chamber of stage 6. The contribution of each of these components to the pressure drop across the sleeve is shown in table 4.18 for the design contribution.

FlowRate	**Pressure**($\times 10^5$ **Pa)**				**Contribution (%)**		
(m^3/hr)	**SC1**	**Axial seal**	**SC2**	**Total**	**SC1**	**Axial seal**	**SC2**
120	3.11	26.55	0.42	30.08	10.34	88.26	1.4
175	4.79	45.55	0.32	50.54	9.46	89.90	0.63
200	5.86	54.63	0.28	60.77	9.65	89.88	0.47
250	8.78	74.52	0.23	83.52	10.51	89.22	0.28

Table 4.18: Pressure drop split up - Center sleeve leak

The results show that the center sleeve head drop is dominated by the head drop across the axial seal. For a quantitative explanation, we compare these results with those of the intra-stage leak contributions given by table 4.13. Considering equations 2.71 and 2.72 from chapter 2, it can be seen that the head drop across the seal is directly proportional to the length, and inversely proportional to the wear-ring clearance. The length of the axial seal in the center sleeve is 2.6 times greater than those in the front chamber of the series stages. But the wear ring clearance in the center sleeve is only 0.83 times the stage front chamber wear ring clearance. Hence the axial seal contribution to the pressure drop is greater in the case of a center sleeve, than the stage.

Due to the dominant effect of the axial seal in the head drop, the effect due to the side chamber is subdued. The second side chamber contribution is close to negligible, and decreases with an increase in the flow rate. The balance sleeve pressure drops are given in table 4.19. The balance sleeve only consists of a long axial seal, whose dimensions are given in table 4.15. The pressure drops are also pretty high across the balance sleeve, because the pressure drop is equal to the total pressure drop across stages 6-11.

FlowRate(m^3/hr)	Pressure drop ($\times 10^5 Pa$)
120	38.9
175	63.3
200	75.2
250	102.3

Table 4.19: Balance sleeve axial seal pressure drops

5

Model Validation

This chapter explains the comparison of the results from the combined CFD-1D model to the test results from Flowserve for the PRT. The customer evaluates the PRT in terms of its performance parameters, the head, flow and power. The performance parameters need to be estimated for all three throat cross-section areas, to be compared with the test results. This chapter contains the details of determining these parameters, starting from the single stages, and combining them for the multiple stages, to show that the CFD-1D model could be used to determine the performance curves of the turbine. Finally, a preliminary correlation with the known pump performance is also discussed.

5.1. Single Stage Calculations

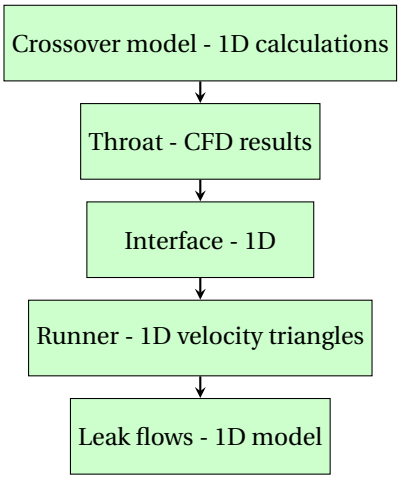

Figure 5.1: Single stage modeling sequence

The head drops for every single stage involve the same set of calculations, obtained from the combined 1D-CFD model, in the sequence shown in figure 5.1.

- The single stage contains a crossover and the runner enclosed by it. The head drop across the crossover ($H_{crossover}$) is calculated according to section 4.1.2.
- The CFD head drop at the throat (H_{throat}) is used in the model. The head drops are obtained for the three different throat areas from the respective simulations, and a second order curve fitting is done to determine them at required throat area values.
- The 1D head drops across the runner (H_{runner}) are determined using the velocity triangles and the 1D methods. The difference between the model with and without considering the blade incidence, and its implications are discussed later in this chapter.
- The leak flow (Q_L) is then incorporated for the single stage using the head drop between the interface and the exit of the runner. The effective head drops for the single stage is then calculated after subtracting the leak flow from the main flow.

  To summarize the whole leak calculation for a single stage, the back chamber leaks are calculated at the beginning of every stage. Stages 1 and 6 do not comprise a back leak. The flow through the back chamber is subtracted from the flow through the crossover. It gets added back, before the flow enters the runner. The flow through the front chamber is subtracted from the main flow through the runner. It gets added back at the end of the stage. So Q remains the same before and after every stage. If subscripts BC and FC denote the back and the front chambers respectively, the flow through the crossover and the runner are given as,

$$Q_{crossover} = Q - Q_{BC}, \tag{5.1}$$

$$Q_{runner} = Q - Q_{FC}. \tag{5.2}$$

  H and η denote the head drop and the efficiency respectively. $H_{crossover}$ is calculated from $Q_{crossover}$, and H_{runner} is calculated from Q_{runner} respectively. The subscripts 5V, 3V and L denote the 5 vane series, 3 vane series and the last stage respectively.

$$H_{5V} = H_{5Vcrossover} + H_{5Vthroat} + H_{5Vrunner}, \tag{5.3}$$

$$H_{3V} = H_{3Vcrossover} + H_{3Vthroat} + H_{3Vrunner}, \tag{5.4}$$

$$H_L = H_{Lcrossover} + H_{Lthroat} + H_{Lrunner}, \tag{5.5}$$

  are the head drops across the 5-vane , 3-vane and the last stages respectively. Since the same crossover is used for the series stages, $H_{5Vcrossover} = H_{3Vcrossover}$.

5.1.1. Inter stage leak corrections

The inter stage leaks also influence the flow into each stage of the PRT. The flow that goes into the center sleeve does not go into stage 1-5, but directly enters stage 6. Similarly, the flow through the balance sleeve does not enter stages 6-11, but goes directly to the outlet. Each series stage has alternatively 5-vane and 3-vane stages. Hence, if subscripts CS and BS denote the center and the balance

sleeves, and S_{1-5} and S_{6-11} denote stages 1-5 and stages 6-11 respectively, the corrected flows through the stages are given by,

$$Q_{5V,S_{1-5}} = Q - Q_{CS} - Q_{5V,FC}, \tag{5.6}$$

$$Q_{3V,S_{1-5}} = Q - Q_{CS} - Q_{3V,FC}, \tag{5.7}$$

$$Q_{5V,S_{6-11}} = Q - Q_{BS} - Q_{5V,FC}, \tag{5.8}$$

$$Q_{3V,S_{6-11}} = Q - Q_{BS} - Q_{3V,FC}, \tag{5.9}$$

$$Q_L = Q - Q_{BS} \; - \; (2 \times Q_{L,FC}). \tag{5.10}$$

The last stage contains two front chamber leaks and hence the effective flow through the runners is less compared to the other series stages.

5.2. Calculation of performance parameters

The overall performance parameters, which are the head drop across the entire PRT and the overall efficiency, are of importance to the customer. This section explains the calculation of the overall head and efficiency of the PRT. The head drop across each stage is calculated according to the expressions 5.3 - 5.5 with the corresponding flow rates from expressions 5.6 - 5.10. The multistage PRT consists of a 5-vane and a 3-vane stage alternatively as shown in figure 4.25. Set1 (stages 1-5) contains three 5-vane runner stages and two 3-vane runner stages. Set2 (stages 6-11) contains three 3-vane runner stages, two 5-vane runner stages and the last stage. H_{set1} and H_{set2} are the head drops for stages 1-5 and stages 6-11 respectively. They are given as :

$$H_{set1} \;\; = \;\; 3 \times H_{5V,S1} \; + \; 2 \times H_{3V,S1}, \tag{5.11}$$

$$H_{set2} \;\; = \;\; 2 \times H_{5V,S2} \; + \; 3 \times H_{3V,S2} \; + \; H_L. \tag{5.12}$$

The Total Differential Head (TDH) is therefore given as,

$$TDH \;\; = \;\; H_{set1} \; + \; H_{set2}. \tag{5.13}$$

The diameter of the last stage runner is 0.81 times the diameter of the series stage runners. There are 10 series stages, and each have the same runner diameter and the same crossover. The affinity laws are used to determine the performance characteristic of one hydraulic machine from a known characteristic measured at a different speed or runner diameter [10]. According to the affinity laws, the heads of two machines, H_A and H_B of different runner diameters D_A and D_B can be given as,

$$\frac{H_A}{H_B} = \left(\frac{D_A}{D_B}\right)^2. \tag{5.14}$$

Since there are 10 series stages, and the last stage, the average head per stage is calculated from the TDH as,

$$TDH_{average} = \frac{TDH}{10 + (0.81)^2}. \tag{5.15}$$

EFFICIENCY

The overall efficiency of the PRT is given by,

$$\eta_t = \frac{P_{shaft}}{P_{fluid}} = \eta_{ht} \times \eta_{vt} \times \eta_{mt}. \tag{2.9}$$

where $\eta_{ht}, \eta_{vt}, \eta_{mt}$ are the hydraulic efficiency, volumetric efficiency and the mechanical efficiency respectively. The efficiencies are calculated for each individual stage of the PRT. The hydraulic efficiency as mentioned earlier, is obtained from CFD simulations for the three different throat cross-sectional areas.

The volumetric efficiency is the estimate of the effective flow that goes through the runner compared to the original flow that enters the PRT. The estimate of the volumetric efficiency incorporates all the leak flows occurring in the pump. Hence the volumetric efficiencies for the individual stages are given by the ratio of the corrected flows given in equations 5.6 - 5.10 to the total flow Q through the PRT.

$$\eta_{V-5V,S1} = \frac{Q - Q_{CS} - Q_{5V,FC}}{Q} = \frac{Q_{5V,S1}}{Q}, \tag{5.16}$$

$$\eta_{V-3V,S1} = \frac{Q - Q_{CS} - Q_{3V,FC}}{Q} = \frac{Q_{3V,S1}}{Q}, \tag{5.17}$$

$$\eta_{V-5V,S2} = \frac{Q - Q_{BS} - Q_{5V,FC}}{Q} = \frac{Q_{5V,S2}}{Q}, \tag{5.18}$$

$$\eta_{V-3V,S2} = \frac{Q - Q_{BS} - Q_{3V,FC}}{Q} = \frac{Q_{3V,S2}}{Q}, \tag{5.19}$$

$$\eta_{VL} = \frac{Q - Q_{BS} - (2 \times Q_{L,FC})}{Q} = \frac{Q_L}{Q}, \tag{5.20}$$

are the volumetric efficiencies of the individual stages.

The overall volumetric efficiency is given by,

$$\eta_{vt} = \frac{3 \times (\eta_{V5V,S1} + \eta_{V3V,S2}) + 2 \times (\eta_{V3V,S1} + \eta_{V5V,S2}) + \eta_{VL}}{11 \times Q}. \tag{5.21}$$

Mechanical efficiency relates to the losses due to the mechanical components in the PRT such as the axial bearings and shaft seals. These losses depend on the design of the pump. In the case of small pumps, the mechanical components consume considerable amount of power. The mechanical efficiency of large pumps is generally 99.5% or more [8]. Hence their effect on the overall efficiency is very small. Since accurate information is not available with respect to these mechanical components, the mechanical efficiency is calculated according to equation 5.22 [8] as,

$$\eta_{mt} = 1 - L_m, \tag{5.22}$$

where L_m is the mechanical loss which is given by,

$$L_m = 0.0045 \left(\frac{Q_{ref}}{Q}\right)^{0.4} \left(\frac{N_{ref}}{N}\right)^{0.3}, \tag{5.23}$$

Here Q_{ref}=1 m^3/s and N_{ref}=1500 rpm. Q and N are the operating flow and speed of the PRT respectively. The mechanical efficiency generally decreases with a decrease in speed [8]. Hence the hydraulic efficiencies from the CFD results, and equations 5.21 and 5.22 are combined to give the overall efficiency of the PRT. The volumetric efficiencies of the three cross sectional areas are compared in figure 5.2 and the mechanical efficiencies for the PRT are given in table 5.1 for the 5 vane series stage. The volumetric efficiency varies with every configuration while the mechanical efficiency remains the same as it depends only on the flow rate and the speed.

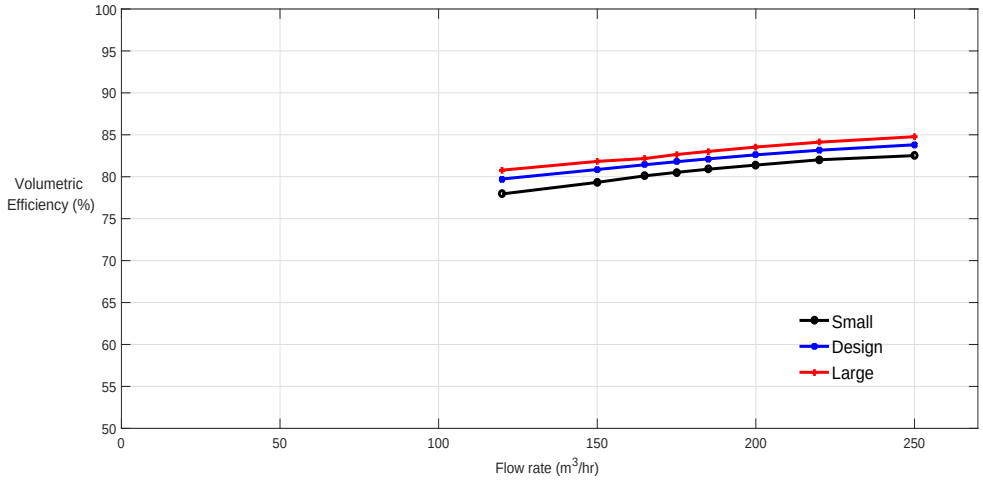

Figure 5.2: Efficiency curve comparison with test results.

FlowRate(m^3/hr)	Mechanical Efficiency(%)
120	98.57
150	98.69
165	98.74
175	98.77
185	98.80
200	98.84
220	98.88
250	98.94

Table 5.1: Mechanical Efficiency

5.3. Validation of performance with test results

The test results from Flowserve are available for a rotor speed of 2985rpm. The test results had been obtained initially for a larger throat area by 112%. An attempt was made to decrease the area by bolting inserts into the casing and the test was conducted again. The second test gives the performance curves for a throat area 89.4% the area from the hydraulic drawing. The entire 1D-CFD model for the pump as

discussed in sections 5.1 and 5.3.2 have been combined to be compared with the experimental curves. The performance curves H-Q and η-Q, obtained from the model in comparison with the experimental curves are discussed next.

5.3.1. Without incidence correction

The results for the discussion in section 4.3 are shown here. In section 4.3, it was considered that the blade incidence correction could be incorporated by subtracting the relative velocity component from the tangential velocity at the interface. This tangential velocity at the interface was calculated according to the method discussed in section 2.5. The performance curves obtained considering this modification are shown in figures 5.3 and 5.4.

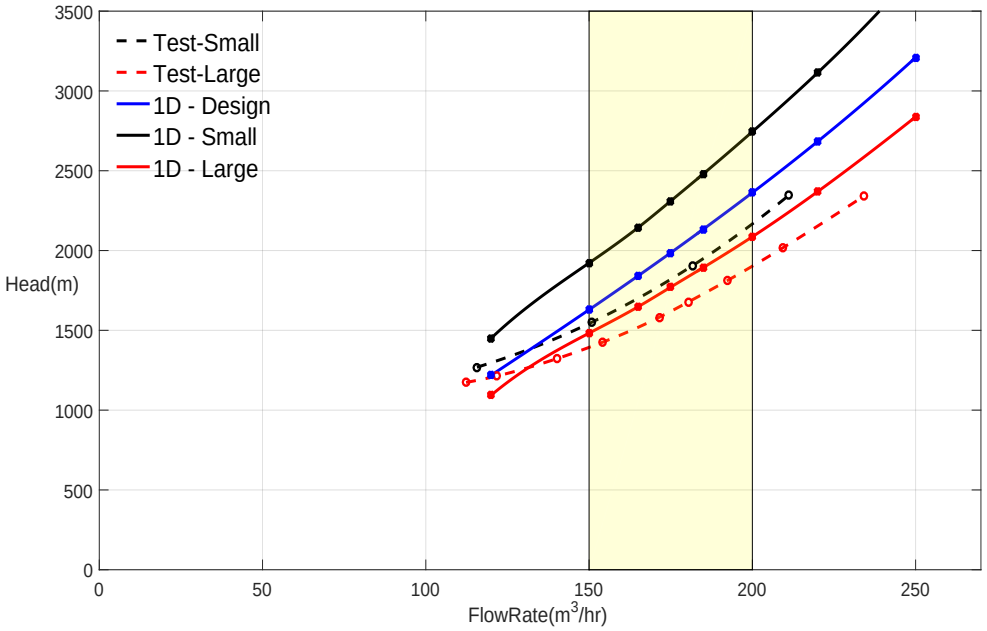

Figure 5.3: H-Q curve comparison with test results for the multistage PRT - without considering blade incidence.

The operating range of these multistage PRTs is from $150-200 m^3/hr$. Hence, the calculations and the simulations have been performed for the range of flow rates of $120-250 m^3/hr$. Since there was no test result for the design configuration, only a single curve (blue curve) from the 1D-CFD model can be presented for it. In this method, the head is calculated according to Euler's head equation given by 2.37. This equation considers only the tangential velocity components at the inlet and the outlet exclusively, for the head calculation. The results shown by the head curve comparison in figure 5.3 are not promising, as the results for the larger throat deviates by around 7-7.5 % from the test result for low flow rates and it increases to 11 % for high flow rates. The deviation is even larger for smaller throat areas, where it exceeds 20 %. The efficiency curves in figure 5.4 give closer results to test measurements at higher flow rates. Hence a comparison is to be made with the model considering the blade incidence correction for accuracy and closeness of the performance parameters. The black curves indicate the head drops for the smaller cross sectional area at the throat, while the red curves indicate those for the larger throat. The dotted and the solid lines represent the test and the 1D-CFD model values respectively. The blue

curve shows the head drop calculated for the design dimensions according to the hydraulic drawing. The yellow region is the area of interest - operating range.

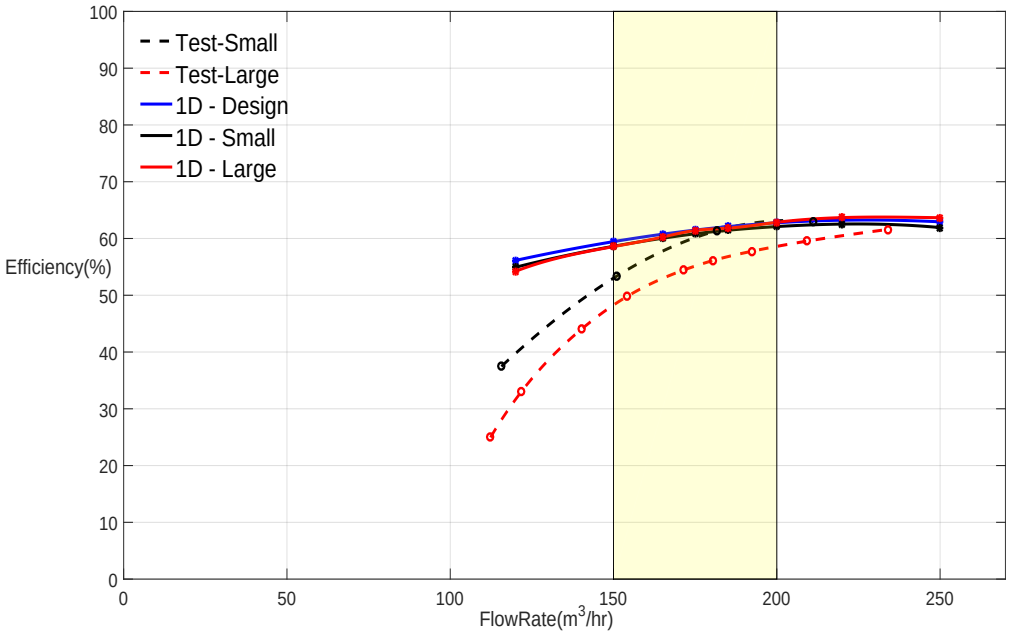

Figure 5.4: Efficiency curve comparison with test results for the multistage PRT - without considering blade incidence.

5.3.2. With incidence correction

The total head drop across the PRT, considering the leakages, and the incidence correction, has been plotted in figure 5.5. The head curve comparison indicates that the results from the 1D model agree well with the test results. The design curve falls well within the expected range between the curves for the smaller and the larger configurations. The prediction for the smaller configuration has a deviation of 6-7% from the results for the operating range. The larger curve on the other hand, has a deviation of less than 8% in the operating range, and around 10-12% at low flow rates. It can also be seen that at low flow rates, less than $150 m^3/hr$, the 1D model also deviates from the value obtained from testing. This can be attributed to the unsteady behavior that is occurring in the PRT at low flow rates. At such low flow rates, the hydraulic efficiencies predicted by the CFD steady-state simulations are also not reliable. The deviation can also be attributed to the variation in blade incidence, where a component of velocity gets added to the tangential velocity as shown in section 4.3.1. Better methods to predict this, would bring the model closer to reality. Transient simulations may predict the performance at such an operating point better. Since the model augurs quite well in the operating range, steady state simulations are sufficient for a preliminary prediction of the performance at points where the PRT can be operated. The efficiency curve comparison shown in figure 5.6 give us a better insight into the performance.

We observe from the efficiency curves that the 1D tool slightly overpredicts the efficiencies by around 5 %, at flow rates of 175-220m^3/hr. But the prediction is even more diverging for lower flow rates. The efficiency prediction is pretty close to the test result for the smaller throat area. Hence it can be observed from the performance curves, that the head drop obtained from the PRT is higher with smaller throat area. The PRT also operates with a higher efficiency, with a decrease in the throat area, in the

desired operating range. This behavior can be seen from both the tool's prediction and the test results. The prediction of the 1D tool is also closer for the smaller throat areas, and expected behavior is observed in the design configuration.

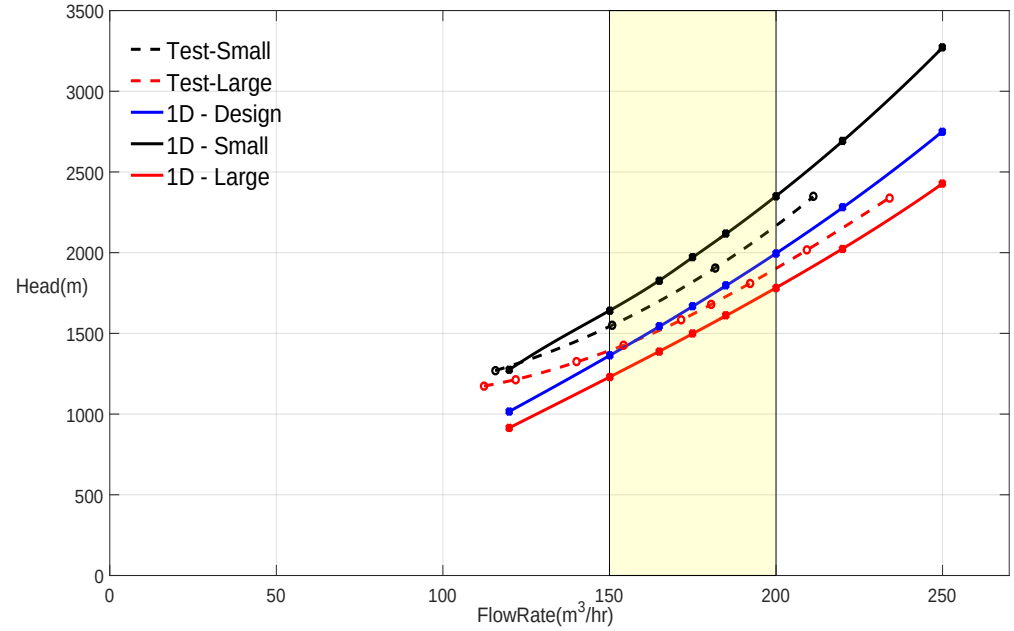

Figure 5.5: H-Q curve comparison with test results for the multistage PRT - with blade incidence.

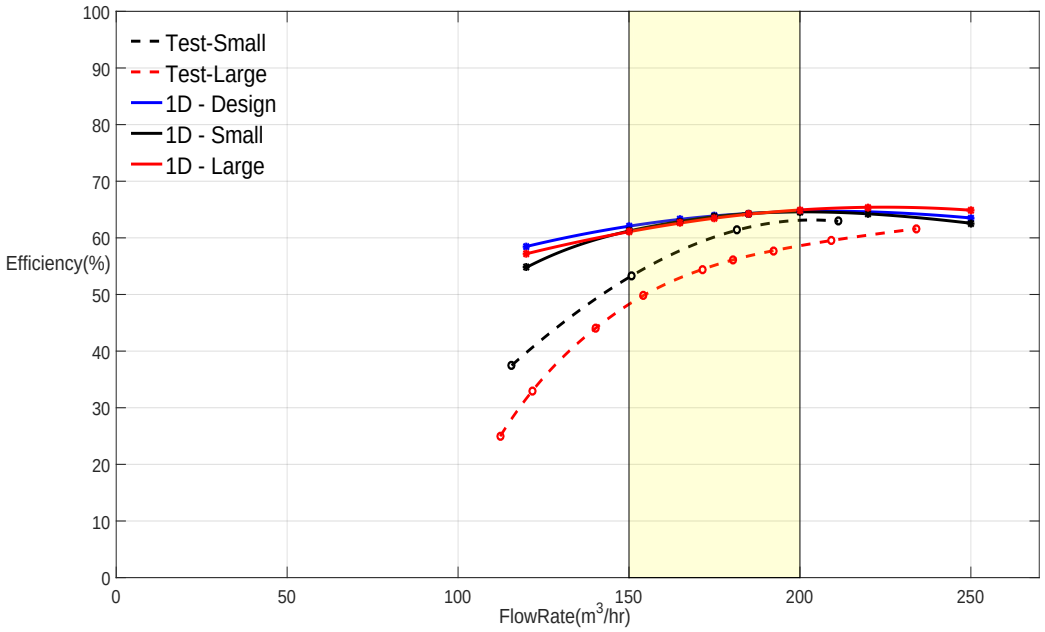

Figure 5.6: Efficiency curve comparison with test results for the multistage PRT - with blade incidence.

Smaller throat areas imply a higher tangential velocity of the fluid coming into the runners. Hence it is beneficial that a pump can be operated as a PRT with the design throat areas or with smaller throat

configurations in the operating range from a customer point of view. The prediction from the tool is also close to the test results for such configurations in the operating range. But at flow rates higher than that of the operating range, the prediction of the 1D tool deviates for the configuration involving higher tangential velocities. It improves for the larger throat configuration, which have lower tangential velocities.

Another important part of the analysis from the performance curves would be the sensitivity of the model. From the performance curves and their analysis, we observe that the prediction is quite good for the smaller throat configuration in the operating range. But as the flow rate increases, the prediction of the model improves for the configuration with the larger throat areas and deviates for the smaller area, as seen with the head curves. This is an important observation, because the tangential velocities of the fluid, are higher for the smaller throat configuration, at higher flow rates. Hence, the range of velocities where the model predicts the performance quite accurately, is similar. The model is quite sensitive to extremely high and low tangential velocities. But it works quite well for velocities which correspond to the operating range of the PRT.

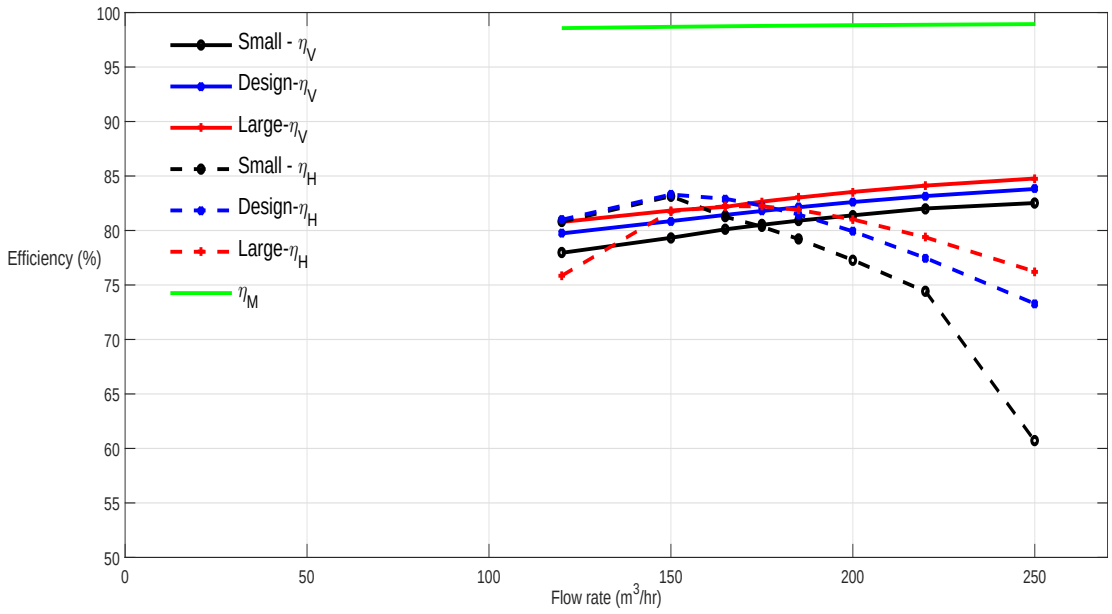

Figure 5.7: Efficiency comparison.

The efficiencies of the PRT are predicted with the same behavior as observed with the test results, where higher efficiencies are achieved at lower flow rates for the smaller throat area configuration. The BEP is achieved at a higher flow rate for the larger throat area compared to the smaller throat area configuration. The overall efficiency of the PRT consists of the hydraulic, volumetric and mechanical efficiency contributions. The efficiencies of all the configurations for the different configurations are compared in figure 5.7. This contains the hydraulic efficiencies obtained from CFD for the 5-vane stage for an understanding of the contribution of the efficiencies. The contribution of the mechanical efficiency is pretty small. The volumetric efficiencies have been predicted through the leak flow calculations. Due to leak flows, the flow through the runner is less than the operating flow rate. Hence, the hydraulic efficiencies also change according to the flow rate. Since the hydraulic efficiencies are obtained from CFD, a qualitative explanation could also be given for the deviation of the model at extremely low flow rates. At these flow rates, the efficiencies of the runner are quite low. Due to unsteady

flow behavior, as mentioned above, the efficiencies predicted by the steady state simulations are not reliable. Also the blade incidence consideration magnifies the deviation of the prediction from the test results at low flow rates.

We can conclude that the results indeed prove that the turbine operates with better efficiencies at higher flow rates than that of the pump. The model which incorporates the incidence correction at the inlet to the blade gives better and closer results to the test measurements than the normal Euler method. Hence this consideration could be a suitable 1D approximation in determining the performance of the PRT. The 1D tool thus predicts the multistage performance within 7-7.5 % deviation in the operating range, which would be useful to obtain the PRT mode operation of a pump setup.

5.4. Transient simulation

As the last step a transient simulation was performed to see understand its influence on the performance parameters. Due to time constraint, the unsteady simulation was performed only for one operating point for the design configuration at $Q = 165 m^3/hr$. The simulations was performed for 10 revolutions of the runner. Dependable results can be attained with 120-250 time steps per revolution [40]. A time step of 0.0001s was set for the runner rotation speed of 2980 rpm, such that it was ensured that there were 200 time steps per revolution. The average Courant number was 3-4 for the chosen time step. The solution was performed with the steady state simulation values as the initial solution. A comparison of the steady state and the transient results for the design configuration at a flow rate of $Q = 165 m^3/hr$ is shown in table 5.2.

	Steady State	**Transient**
Head (m)	195.49	192.48
Efficiency (%)	82.91	83.29
Inlet Tangential Velocity (m/s)	33.21	32.80

Table 5.2: Comparison of Steady State and Transient Results

	Outlet Swirl (m/s)		
	Steady State	**Transient**	**1D**
Large	3.18	NA	6.18
Design	4.36	5.47	
Small	5.31	NA	

Table 5.3: Comparison of outlet swirl velocities $Q = 165 m^3/hr$.

It can be seen from table 5.2 that the steady state and the transient results are quite close to each other, with less than 2% deviation for the head, efficiency and the tangential velocity predictions. The efficiencies predicted by the transient simulations are higher than that of the steady state as observed in the pumps. But the transient simulation predicts a higher swirl velocity at the outlet compared to the steady state simulation. This would explain well the difference between the head values obtained from the two results. It can also be seen from table 5.3 that the outlet swirl predicted by the transient simulation is lot closer to the 1D prediction, which proves that the 1D model can indeed give closer results to the actual phenomena at the outlet. This means that at lower values of the inlet tangential velocity, the

over-prediction inflicts a greater impact on the head, whereas at higher tangential velocities, the effect is minimal. This effect is also a contribution to the deviation seen in the performance curves, from the test results.

Therefore the 1D tool predicts the performance closer to the actual phenomena, as the results are closer when compared with the transient simulation. Yet, from an overall perspective, steady state simulation results are reliable in the operating range and hence can be used considering the advantage of lower computational time and resources.

5.5. Pump empirical relations

One of the common problems in industry, is the cost and time involved in testing of the hydraulic machines. Since the performance of the PRT cannot be predicted for a successful outcome, naturally, less investment and effort is put towards testing pumps as PRTs. Hence it would be beneficial to derive the performance of the PRT from known pump performance data, so that a quick and educated decision can be made, on whether it would be useful to operate the pump as a PRT. This section contains a comparison of the results obtained from the PRT model with the pump test data. Some validation of empirical relations from literature, between pump data and PRT data are also discussed. Preliminary empirical relations are derived for the PRT performance from the pump data itself, which provide a good insight into future research work. The test results are available for the pump mode, only for the configuration with the larger cross sectional throat area. The comparison with the corresponding PRT results is shown in figures 5.8 and 5.9. It is seen that the flow rate of the pump is lower than that of the PRT at BEP.

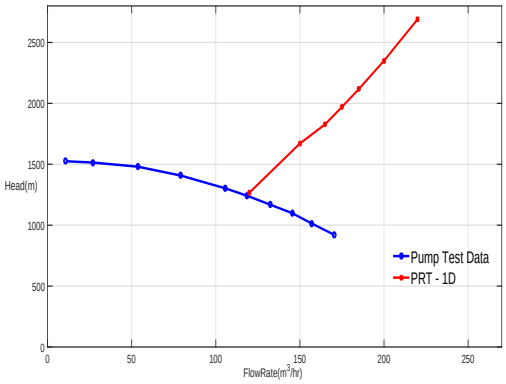

Figure 5.8: Head curve comparison wih pump curve

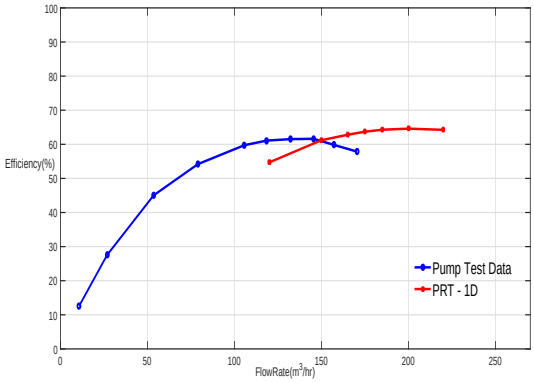

Figure 5.9: Efficiency curve comparison wih pump curve

Stepanoff [7] compares the performance parameters of the pump and the turbine modes, with a number of test results. He gives empirical relations stating that the head ratio H_P/H_T will equal the efficiency of the pump, while the flow ratio Q_P/Q_T will equal the square of the efficiency. Here Q_P, H_P are the flow rate and the head in the pump mode, while Q_T, H_T are the flow rate and the head in the turbine mode. Gopalakrishnan [6] also plotted the head and flow ratios, from the test results of a number of pumps. He stated from his results that the actual performance varies substantially from the existing correlations to relate the two modes of operation.

On these grounds, the results from the 1D model were also compared with the test data obtained for the two modes of operation. The flow ratios have been calculated for the pump, with both the 1D

and test results for the PRTs, and have been plotted against the pump efficiencies. The comparison is shown in figure 5.10. We try to derive empirical relations between the pump and the PRT performance, and correspond them to similar relations in literature. Thereby, the PRT performance is tried to be estimated from the known pump performance. Initially the flow ratios were compared with the efficiency line of the pmp indicated by eta_P in the figure. It is found then, using trial and error that the 1D predictions correspond well with the $1.05\sqrt{(\eta_P)}$ line whereas the test flow ratios correspond well to the $0.9\eta_P$ line. Hence the 1D model flow ratio $(\frac{Q_P}{Q_T})_{1D}$ is initially calculated using the tool, and the $(\frac{Q_P}{Q_T})_{actual}$ is calculated from the known pump efficiency using the expression,

$$(\frac{Q_P}{Q_T})_{actual} = \frac{0.9\,\eta_P\,(\frac{Q_P}{Q_T})_{1D}}{1.05\sqrt{\eta_P}} = 0.86\,\sqrt{\eta}_P\,(\frac{Q_P}{Q_T})_{1D} \tag{5.24}$$

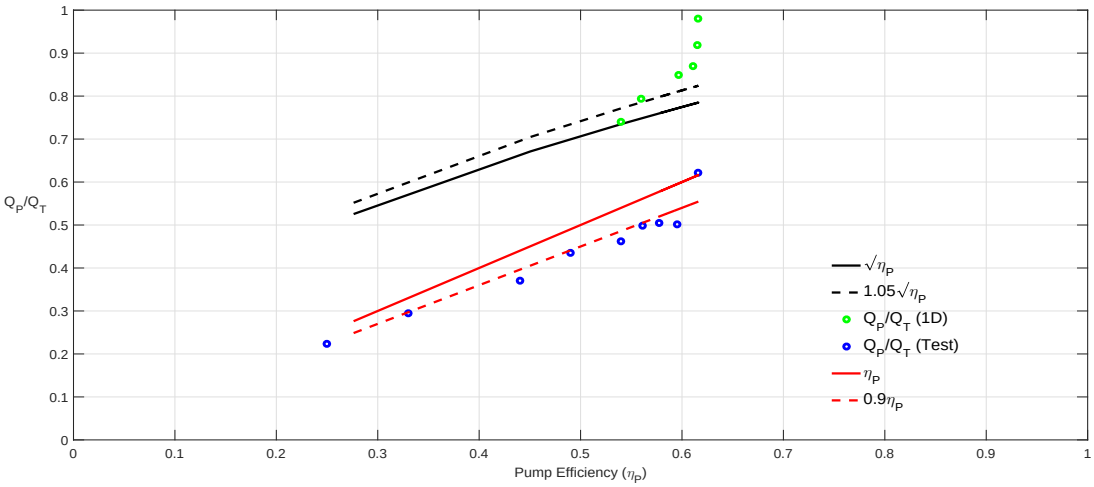

Figure 5.10: Flow ratio comparison

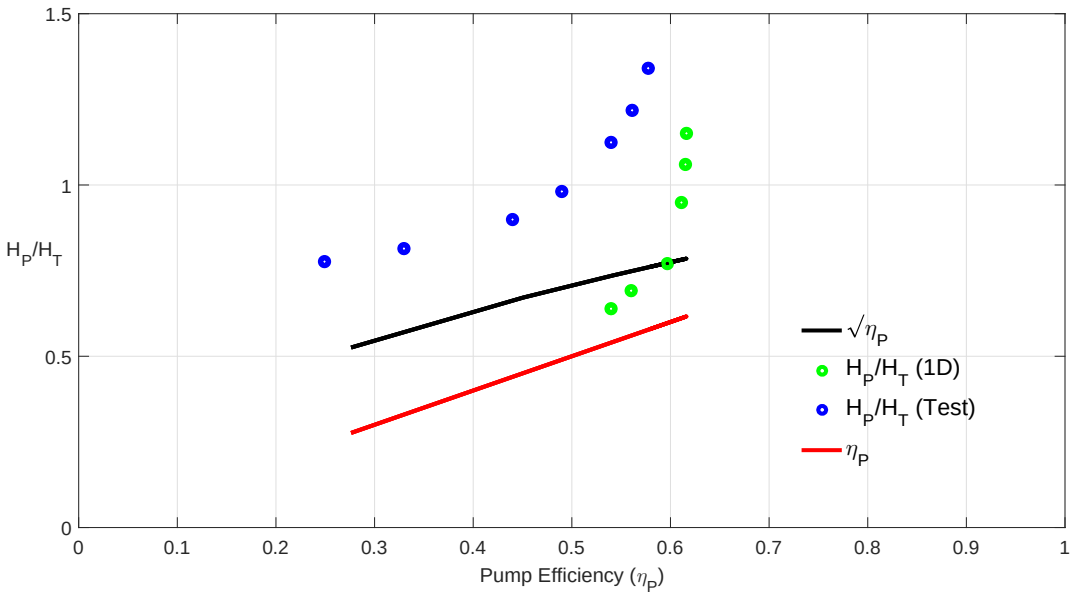

Figure 5.11: Head ratio comparison

But figure 5.11 shows that the empirical prediction of the head ratio, is not as as easy or straightforward as the flow ratio. The linear empirical relations with the pump efficiencies do not correspond well to the results from the model or with the test data. Hence, in accordance with Gopalakrishnan [6], empirical relations are not enough to predict the entire performance of the PRT from pump test data. Even for the flow ratio, the relation given by equation 5.5 represents the behavior well until around the BEP of the PRT. But beyond the BEP, the PRT efficiency curve is flat, and hence the flow ratio value overshoots the linear behavior. Though the relation gives a good estimate of the performance of the PRT from the pump data, it can be concluded, that more test results are needed for PRT in the same specific speed, to generalize the applicability of the empirical relation. The coefficients 0.9 and 1.5 used in equation 5.5 are also subject to change depending on the throat area configuration of the PRT. Hence with corresponding pump mode test results, empirical relations could be obtained for all different configurations to determine the flow through the PRT at a particular pump efficiency (η_P). This would lead to a generalized relation to estimate the PRT mode performance from the pump data itself, if design modifications are considered the way forward in PRT technology.

With the current method, the performance of the PRT for a single operating point can be obtained from the pump data as follows. The flow through the PRT can be obtained from the pump efficiency using relation 5.5. The 1D model can then be used with flow rate and other input conditions to predict the performance parameters of the PRT.

In this chapter, the results for the combined 1D tool have been validated against the test results. They are found to be in good agreement with the results from testing. The two models with and without considering the blade incidence have been compared and reasons for the deviation have been discussed. The transient simulation is performed for one operating point and has been compared with the steady state and the 1D results. The steady state simulation give a relatively good picture of the performance in the operating range, given their advantages in terms of computation time. A preliminary effort has also been made towards deriving PRT performance from known pump performance.

6

Conclusions and Recommendations

6.1. Summary

The thesis work presents a methodology for the modeling of a hydraulic multistage Power Recovery Turbine (PRT). A 1D method, combined with CFD, to estimate the performance parameters has been derived out of this study. A full 1D methodology is not sufficient to model the 3D flow phenomena observed in a PRT. Hence, CFD simulations have been carried out with the ANSYS CFX software. The results for the complicated flow regions, such as the throat, and the hydraulic efficiency have been obtained from CFD, and combined with the 1D performance model. The 1D model has been derived for water, under steady state, adiabatic flow conditions. It is based on the geometry of the PRT, the fluid properties and the inlet flow rate. The operating range of the PRT is 150-200 m^3/hr. The method requires models for the crossover, the throat-volute interface, the runner and the leak flows. Models have been derived for the crossover, from pipe flow equations, and for the runner, from the 1D velocity triangles. The leak flows happening within a single stage of the pump (intra-stage leaks), and between stages(inter-stage leaks) are estimated based on literature. They have a considerable effect on the total head drop obtained from the PRT. The novelty of the work is the method used to determine the Total Differential Head (TDH) and the efficiency of the PRT, by combining the intra-stage and the inter-stage leaks. The overall calculations are done for three different configurations of the PRT, based on different throat areas, and are validated with the test results obtained from Flowserve. The work also proposes a preliminary empirical approximation for determining the PRT flow from the pump flow using the pump efficiency.

6.2. Conclusions

6.2.1. Stage Modeling

- The crossover contributes only 3-4% to the total head drop across a single stage. This is estimated within a 6% deviation by 1D calculations using pipe flow equations.
- Since the throat, volute and the interface to the runner are difficult to be modeled completely with 1D models, suitable 1D models are used to represent them along with the runner, and are corrected with the hydraulic efficiencies obtained from CFD.
- The runner modeled with the 1D velocity triangles, considering the incidence of the fluid on the blade and its influence. The model gives good results within 6% deviation in the operating range of $150 - 200 m^3/hr$. The deviation is due to the deviation of the model past the cutwater, in the volute-runner interface. Hence a more detailed volute interface model to capture the 3D flow can give a more accurate prediction.
- The estimation of the leak flows has been done using an appropriate iterative model. The leak flows within a single stage decrease with an increase in cross sectional area of the throat. The percentage leak flows are lower for higher flow rates in the PRT, indicating a higher volumetric efficiency.

6.2.2. Multistage Modeling

- The multistage performance parameters, the Total Differential Head (TDH) and the efficiency of the PRT are obtained by combining the single stage models. The leak between stages (inter-stage leaks), play a significant role in determining the performance. Hence a sequential iterative scheme is implemented to estimate the leaks. The inter-stage leaks are found to show the same behavior as the leaks within a stage.
- The multistage performance parameters thus obtained are compared with the test results. We obtain a really good estimate of the TDH for the design configuration of the stages according to the hydraulic drawing. There is a deviation of 6-7% for the configuration with a smaller cross sectional area of the throat, and an 8% deviation for the configuration with the larger throat. This deviation can be attributed to the deviation in prediction at the volute interface.
- The efficiency curves obtained from the 1D model do not show much of deviation between configurations. But they follow the expected behavior as seen from the test results. The overall efficiency of the PRT is composed of the hydraulic, volumetric efficiencies. The individual efficiency comparisons show that the volumetric efficiency results for the different configurations are close to each other. The volumetric efficiency, determined by the leaks, is governed by the tangential velocity of the fluid at the interface. Hence the deviation of the efficiency curves and their closeness for different configurations could also be attributed to the model at the interface.

Overall, the 1D model supported by CFD, gives a really good performance prediction of the multistage PRT. With this model, the performance parameters of can be estimated from the pump geometry, and the general input conditions, which are the flow rate and the rotation speed. As a last step,

a attempt is made to derive empirical relations between the pump mode performance and the corresponding PRT mode performance, validating them with test data. It can be seen that an approximate empirical relation can be derived for the flow ratio between the pump and the PRT for given values of pump efficiency, at least until the Best Efficiency Point (BEP). The flow rate required through a PRT to produce the same efficiency as the pump can be known. Using this flow rate as the input tool into the 1D tool, the other performance parameters of the PRT can be well determined. Though the empirical relation needs more test results for validation, it gives a good picture of where future research can be focused.

6.3. Recommendations

- The deviation in the model is mostly attributed to the velocity predictions at the throat and the interface. Hence more detailed study on the the volute interface would lead to a more accurate prediction of the performance. The hydraulic efficiencies should also be determined by 1D methods. An accurate method for both these parts would establish a full 1D model, without the use of CFD.
- The CFD simulations and the 1D methods assume uniform velocity conditions at the inlet of every stage. Simulations coupling 2 or 3 stages will also incorporate the outlet swirl at the end of every stage. Hence simulations and modeling with correct inlet pre-swirl is a scope for future work.
- The 1D results show closer results when validated against transient simulations. Hence transient simulations can be performed given the time factor, for select PRT operating points close to BEP for a better estimate of the hydraulic efficiency.
- The velocity triangles in the 1D tool can be reworked for future modifications in the runner and the changes can be easily adapted in the model.
- More test measurements at the side chambers and leak paths, such as balance sleeve would be beneficial for validation of the leak flow models.
- It would be interesting to see how much the friction resistances and the lengths of the axial seals can be increased, as much as possible within the design limitations, to reduce the leak flows. A decreased side chamber width would also be beneficial to reduce leaks, keeping in mind the axial thrust considerations.
- More comparison between test data for pump and PRT modes of operation for the change in cross section area of throat would give an insight on whether the proposed empirical relations can be generalized between the pump and PRT modes of operation.

A

Discretization error

In this section, the method used to determine the discretization error discussed by Celik [41] is discussed in detail This is according the the Richardson extrapolation method. Three different mesh sizes are chosen and are compared to select the best mesh to estimate the discretization error.

As the first step, the mesh or grid size h is determined. The grid size h is given by,

$$h = \left[\frac{1}{N} \sum_{i=1}^{N} V_{domain} \right]. \tag{A.1}$$

where N denotes the number of elements and V_{domain} is the total volume of the computational domain.

The three meshes are assessed using the key parameters or the output (ϕ) that we obtain from the system. In the case of the PRT, the head and the efficiency are the parameters. With the grid sizes h_1<h_2<h_3, the refinement is chosen systematically and are given by $r_{21} = h_2/h_1$ and $r_{32} = h_3/h_2$. The r values should preferably b greater than 1.3 according to Celik [41]. From these values, the apparent order,p is calculated. It is given by,

$$p = \frac{1}{\ln(r_{21})} \left| \ln|r_{32} - r_{31}| + q(p) \right| \tag{A.2}$$

ANSYS CFX uses a second order high discretization scheme. A difference between the apparent order and the discretization scheme used by CFX is not a sign of unsatisfactory calculations [41]. The extrapolated values according to the Richardson extrapolation are then calculated from p. If the refinement between the grids is not constant, q(p) needs to be solved iteratively. If not q(p) = 0. q(p) though has very less influence on the results for smaller values of refinement. q(p) is given by,

$$q(p) = \ln\left(\frac{r_{21}^{p} - s}{r_{32}^{p} - s}\right), \tag{A.3}$$

$$s = 1.sgn\left(\frac{\epsilon_{32}}{\epsilon_{21}}\right), \tag{A.4}$$

where s is sign function with either 1or -1 as its value. ϵ is the difference between the parameters of interest given by,

$$\epsilon_{21} = \phi_2 - \phi_1, \tag{A.5}$$

$$\epsilon_{32} = \phi_3 - \phi_2. \tag{A.6}$$

We then find the extrapolated value (ϕ_{ext}^{21}), which represents the parameter value, when the cell size tends to zero, given by,

$$\phi_{ext}^{21} = \frac{(r_{21}\phi_2 - \phi_2)}{(r_{21} - 1)}, \tag{A.7}$$

The approximate relative error (e_a^{21}) is given as,

$$e_a^{21} = \left|\frac{\phi_1 - \phi_2}{\phi_2}\right|. \tag{A.8}$$

The extrapolated relative error ($e_{ext}^{2}1$) is therefore estimated as,

$$e_{ext}^{21} = \left|\frac{\phi_{ext}^{21} - \phi_1}{\phi_{ext}^{21}}\right|. \tag{A.9}$$

The Grid Convergence Index (GCI) is then estimated, which gives a measure of how close the solutions from the grid are to each other. A combination of two grids with a smaller value of GCI indicates that the CFD results have only a small deviation, and hence the coarser grid of the two could be chosen, to save on computational time and resources. The GCI is given by the expression,

$$GCI_{21} = \frac{1.25e_a^{21}}{r_{21}^{p} - 1}. \tag{A.10}$$

The GCI of the other combination of grids can also be found in a similar fashion.

The method is first applied to the runner alone simulations to find the best economical mesh settings for the runner. Then the mesh sensitivity is carried out for the crossover and volute, with three different grids, in combination with the runner mesh chosen from the previous step. The refinement factor could not always be greater than 1.3, while using ANSYS meshing due to limitations in the license. The results for the grid sensitivity study to determine the discretization error are shown in tables

B

Theoroms and Coefficients

B.1. Leibniz rule

The Leibniz rule is an expression for the differentiating of definite integral, which has limits that are the functions of another variable. Since we encounter a similar situation in equations 2.52 and 2.53, the Leibniz rule is used. It is used here to integrate equations 2.52 and 2.53 in the axial z-direction with limits z_1 and z_2.

Let f(r,z) be a function such that both f(r,z) and its partial derivative $\frac{\partial f(r,z)}{\partial r}$ are continuous in z and r in some region of the (r,z)-plane, including $z_1 \leq z \leq z_2$, $r_1 \leq r \leq r_2$. Also suppose that the functions $z_1(r)$ and $z_2(r)$ are both continuous and both have continuous derivatives for $r_1 \leq r \leq r_2$. Then for $r_1 \leq r \leq r_2$ [42] :

$$\int_{z=z_2}^{z=z_1} \frac{\partial f(r,z)}{\partial r} dz = \frac{\partial}{\partial r}\left(\int_{z=z_2}^{z=z_1} f(r,z)dz\right) + \frac{\partial z_1}{\partial r} f(r,z_1) - \frac{\partial z_2}{\partial r} f(r,z_2). \tag{B.1}$$

The Leibniz rule is also sometimes called as differentiation under an integral sign.

B.2. Friction coefficients

The pressure losses in the pipes can be classified into major and minor losses. The major losses in pipes are due to friction, while the minor losses are due to change in velocity across the pie due to bends, valves and other components. We can see from equation 2.10, that the first term is the major head loss, while the second gives us the minor head loss.

$$H_{curv} = \frac{1}{2g} f_s u^2 \pi \frac{R_b}{D_e} \frac{\theta}{180^\circ} + \frac{1}{2} k_b \rho u^2. \tag{2.10}$$

The major head loss depends on pipe or duct length, the flow velocity, the pipe diameter, the Reynolds number of the flow (whether the flow is laminar or turbulent) and a friction factor based on the roughness of the pipe (denoted by f_s in equation 2.10). If l is the length of the pipe and d_h is the hydraulic diameter, the general equation for major head loss is given by,

$$H_{major} = \lambda \frac{l}{d_h} \frac{\rho v^2}{2} \tag{B.2}$$

where λ is the friction coefficient, which depends on whether the flow is laminar or turbulent. If the flow is laminar, $\lambda = 64/Re$. If the flow is transient, $2300 \leq Re \leq 4000$, λ cannot be determined. For turbulent flow, $\lambda = f(Re, k/d_h)$, where k is the absolute roughness of the pipe, and k/d_h is the relative roughness of the pipe. The roughness of the pipes are determined by experiments. The friction coefficient, λ can be determined by the Colebrook-White equation, shown by equation 2.11, which can be solved iteratively. The Colebrook-White equation is solved and represented in the Moody chart. From the chart, the friction coefficient can be determined, if the Reynolds number and the relative roughness are known. The Moody diagram is shown in figure B.1.

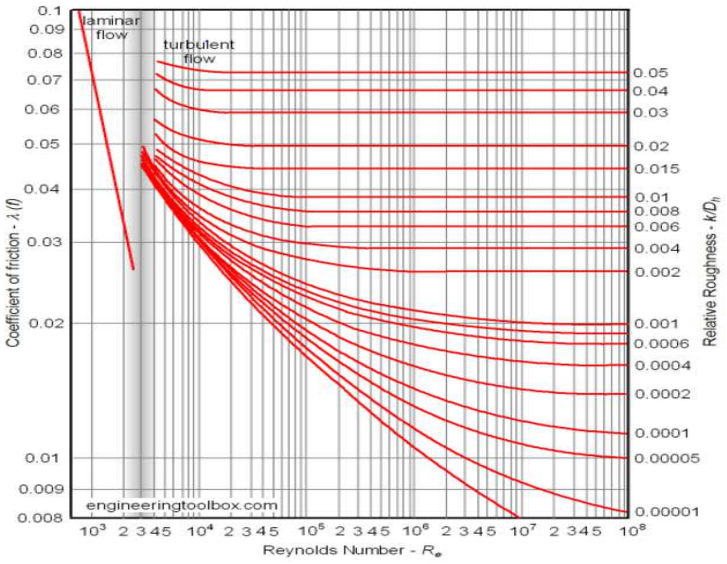

Figure B.1: Moody diagram for friction coefficient (λ)

The minor losses on the other hand, as shown by the second term in equation 2.10, depend on a coefficient given according to the geometry of the pipe. They are determined using a bend coefficient which depends on the angle of the bend, the radius of curvature of the bend and the diameter of the pipe. The bend loss coefficients have been chosen according to [15].

C

MATLAB codes

This sections shows some of the MATLAB codes and models used for the calculations.

Runner 1D Calculations :

```
% Throat and Volute clearance calculations
Q_m=Q/2;
A1 = 0.000706;
V_th = Q_m/A1;
alpha1 = 1.8;
C_uth = V_th*cosd(alpha1);
r_h = 0.1611;
r_z = 0.16193;
e = 0.00318;
k_t = 0.25;
a_t = 0.02223;
r_zeff = r_z+e+(k_t*a_t);
C_u2 = C_uth*r_zeff/r_h;


% Outlet Calculations
D2 = 0.3223; Z = 5; t2 = 0.00397; b2 = 0.011;
beta2 = 20;
A2 = (3.14*D2 - (Z*t2/sind(beta2)))*b2;
C_m2 = Q_m/A2;
C_w2 = C_m2/tand(beta2);
U2 = omega*D2/2;
C_u2e = U2-C_w2;                    % Tangential velocity at the inlet
```

```
% Inlet Calculations with two point at hub and shroud
D11 = 0.11113; D12 = 0.11589;
D1 = 0.11509; t1 = 0.003175; b1 = 0.0167;
beta11 = 22; beta12 = 20;
A11 = (3.14*D11 - (Z*t1/sind(beta11)))*b1;
A12 = (3.14*D12 - (Z*t1/sind(beta12)))*b1;
C_m11 = Q_m/A11;
C_m12 = Q_m/A12;
C_w11 = C_m11/tand(beta11);
C_w12 = C_m12/tand(beta12);
U1 = omega*D1/2;
U11 = omega*D11/2;
U12 = omega*D12/2;
C_u11 = U11 - C_w11;
C_u12 = U12 - C_w12;
C_u1 = (C_u11 + C_u12)/2;


L1 = (D2-D1)/2;


% Runner Head
HeadS1 = ((C_u2-C_w2)*U2 - (U1)*C_u1)/(9.81*Eff);
```

Side Chamber Leak Calculation :

```
G = t_f/r2;
q_dl = q_f/(pi*omega*(r2^3));
t1 = (r2+agap)/r2;
t2 = r1/r2;
k_f0 = 1/(1+sqrt((t1^5 - t2^5 + 5*G*t1^4)/(1 - t2^5 + 5*G*t2^4)))
Re_0 = omega*r2^2/kinvisc;


% Loop for the radial direction in the side chamber h = -(r2/r2 - r_wf/r2)/5000;
r = r2/r2:h:r_wf/r2;
rad = r*r2;
ra = length(r);
term = 0 ;


for i=1:ra-1;


V_u(i) = V_u0;
k_f(i) = V_u(i)/(rad(i)*omega);
int = real(k_f(i))*real(k_f(i))*rad(i)*(r2-r_wf)/length(r);
term = term + int;
```

```
% Multi-stage Runge-Kutta Method to solve for entrainment coefficient

k1(i) = circumvelocityfront(q_dl,Re_0,r(i),k_f0,k_f(i));
k2(i) = circumvelocityfront(q_dl,Re_0,r(i)+h/2,k_f0,k_f(i)+((k1(i)*h)/2));
k3(i) = circumvelocityfront(q_dl,Re_0,r(i)+h/2,k_f0,k_f(i)+((k2(i)*h)/2));
k4(i) = circumvelocityfront(q_dl,Re_0,r(i)+h,k_f0,k_f(i)+(k3(i)*h));
delk_f(i) = (k1(i)+(2*k2(i))+(2*k3(i))+k4(i))/6;
k_f(i+1)= k_f(i) + h*delk_f(i);
V_u(i+1)= k_f(i+1)*rad(i+1)*omega;
V_u0 = V_u(i+1);

end

term = term + real(k_f(end))*real(k_f(end))*rad(end)*(r2-r_wf)/length(r);

% Pressure Calculation - Contributions of different terms

dp_corerot = rho*(omega^2)*term;                    % Contribution of core-rotation
dp_leakage = q_f^2/(8*pi^2*t_f^2)*(1/r_wf^2 - 1/r2^2);   % Contribution of Leakage Flow
DP_sidechamber = dp_corerot + dp_leakage;           % Total side chamber pressure drop

% Function circumvelocity front gives the variation of core rotation coefficient with radius

dkf_dr = 0.079*(r^(8/5))/(q_dl*Re_0^(1/5))*(((1-k_f0)*k_f/k_f0)^(7/4) - abs((1-k_f)^(7/4))) - 2*k_f/r;
```

Wear-ring calculation :

```
% Yamada wear ring flow loss calculation

A_wr = pi*((r_wf+s)^2 - r_wf^2);      % Wear-ring area
v_m = q_f/A_wr;                       % mean velocity of axial flow
u1 = r1*omega;                        % peripheral velocity of impeller
Re = v_m*s/kinvisc;                   % Flow Reynolds number
Re_omega = u1*s/kinvisc;              % Rotating Reynolds number

% Calculating resistance coefficient lambda = 0.26*(Re^-0.24)*(1+(7/8)^2*(Re_omega/(2*Re))^2)^0.38;
dp_yamada = (lambda*l/2/s*rho/2)*v_m^2;

% Inlet and Exit Loss - Wear Ring
dp_inout = 1.5*rho*v_m^2/2;
DP_wearring = dp_yamada + dp_inout;
```

Bibliography

[1] N. Baines, K. Oliphant, H. Kimmel, and G. Habets, "Cfd analysis and test of a fluid machine operating as a pump and turbine," in *IMechE Seminar Publication, CFD in Fluid Machinery*, vol. 15, 1998.

[2] "Pump types guide." `http://www.pumpscout.com/articles-scout-guide/pump-types-guide-aid100.html`. Accessed: 2016-04-05.

[3] "Multistage pump." `http://www.hubluxe.com/multistage.html`. Accessed: 2016-09-02.

[4] H. Nautiyal, V. Varun, A. Kumar, and S. Y. S. Yadav, "Experimental investigation of centrifugal pump working as turbine for small hydropower systems," *Energy Science and technology*, vol. 1, no. 1, pp. 79–86, 2011.

[5] L. Nelik and P. Cooper, "Performance of multi-stage, radial-inflow hydraulic power recovery turbines," *ASME Paper*, no. 84-WA, 1984.

[6] S. Gopalakrishnan, "Power recovery turbines for the process industry," in *Proceedings of the Third International Pump Symposium*, pp. 3–11, 1986.

[7] A. J. Stepanoff, "Centrifugal and axial flow pumps," 1948.

[8] J. F. Gülich, *Centrifugal pumps*. Springer, 2008.

[9] E. Kenneth and P. Nichols, "How to select turbomachinery for your application," *Barber-Nichols Inc*, pp. 5–6, 2012.

[10] I. J. Karassik, J. P. Messina, C. C. Heald, and P. Cooper, *Pump handbook*, vol. 3. McGraw-Hill, 1976.

[11] S. L. Dixon and C. Hall, *Fluid mechanics and thermodynamics of turbomachinery*. Butterworth-Heinemann, 2013.

[12] P. Drtina and M. Sallaberger, "Hydraulic turbines—basic principles and state-of-the-art computational fluid dynamics applications," *Proceedings of the Institution of Mechanical Engineers, Part C: Journal of Mechanical Engineering Science*, vol. 213, no. 1, pp. 85–102, 1999.

[13] I. E. Idelchik and E. Fried, "Handbook of hydraulic resistance," 1986.

[14] "Bends, flow and pressure drop." `http://www.thermopedia.com/content/577/`. Accessed: 2016-06-17.

[15] "Minor loss coefficients in pipes and tubes components." `http://www.engineeringtoolbox.com/minor-loss-coefficients-pipes-d_626.html`. Accessed: 2016-06-18.

[16] O. E. Turgut, M. Asker, and M. T. Coban, "A review of non iterative friction factor correlations for the calculation of pressure drop in pipes," *Bitlis Eren University Journal of Science and Technology*, vol. 4, no. 1, 2014.

[17] S. Venkateshan, *Mechanical measurements*. John Wiley & Sons, 2015.

[18] B.-C. Will, *Theoretical, Numerical and Experimental Investigation of the Flow in Rotor-Stator Cavities With Application to a Centrifugal Pump*. PhD thesis, Universität Duisburg-Essen, Fakultät für Ingenieurwissenschaften» Maschinenbau und Verfahrenstechnik» Institut für Energie-und Umweltverfahrenstechnik, 2011.

[19] G. K. Batchelor, "Note on a class of solutions of the navier-stokes equations representing steady rotationally-symmetric flow," *The Quarterly Journal of Mechanics and Applied Mathematics*, vol. 4, no. 1, pp. 29–41, 1951.

[20] J. W. Daily and R. E. Nece, "Chamber dimension effects on induced flow and frictional resistance of enclosed rotating disks," *Journal of basic engineering*, vol. 82, no. 1, pp. 217–230, 1960.

[21] W. Li, "Model of flow in the side chambers of an industrial centrifugal pump for delivering viscous oil," *Journal of Fluids Engineering*, vol. 135, no. 5, p. 051201, 2013.

[22] Y. Yamada, "Resistance of a flow through an annulus with an inner rotating cylinder," *Bulletin of JSME*, vol. 5, no. 18, pp. 302–310, 1962.

[23] "Marine hydrodynamics - lecture 17." `http://web.mit.edu/13.021/demos/lectures/lecture17.pdf`. Accessed: 2016-05-12.

[24] J. H. Ferziger and M. Peric, *Computational methods for fluid dynamics*. Springer Science & Business Media, 2012.

[25] H. Keck and M. Sick, "Thirty years of numerical flow simulation in hydraulic turbomachines," *Acta Mechanica*, vol. 201, no. 1-4, pp. 211–229, 2008.

[26] S. B. Pope, "Turbulent flows," 2001.

[27] G. Tryggvason, "Classical turbulence modelling," 2011.

[28] "Best practice guidelines for turbomachinery cfd." `http://www.cfd-online.com/Wiki/Best_practice_guidelines_for_turbomachinery_CFD`. Accessed: 2016-05-05.

[29] W. Vieser, T. Esch, and F. Menter, "Heat transfer predictions using advanced two-equation turbulence models," *CFX Validation Report, Report No. CFX-VAL*, vol. 10, p. 0602, 2002.

[30] "Ansys turbogrid." `http://www.ansys.com/Products/Fluids/ANSYS-TurboGrid`. Accessed: 2016-07-21.

[31] E. Bacharoudis, A. Filios, M. Mentzos, and D. Margaris, "Parametric study of a centrifugal pump impeller by varying the outlet blade angle," *Open Mechanical Engineering Journal*, vol. 2, no. 5, pp. 75–83, 2008.

[32] F. A. Muggli, P. Holbein, and P. Dupont, "Cfd calculation of a mixed flow pump characteristic from shutoff to maximum flow," *Journal of fluids engineering*, vol. 124, no. 3, pp. 798–802, 2002.

[33] K. Anup, B. Thapa, and Y.-H. Lee, "Transient numerical analysis of rotor–stator interaction in a francis turbine," *Renewable Energy*, vol. 65, pp. 227–235, 2014.

[34] C. Ansys, "Solver theory guide," *Ansys CFX Release*, vol. 11, pp. 1996–2006, 2006.

[35] T. S. Phillips and C. J. Roy, "Richardson extrapolation-based discretization uncertainty estimation for computational fluid dynamics," *Journal of Fluids Engineering*, vol. 136, no. 12, p. 121401, 2014.

[36] "American petroleum institute standard 610, centrifugal pumps for petroleum petrochemical and natural gas industries," *ISO 13709:2009*, 2010.

[37] J. Kurokawa, M. Sakuma, *et al.*, "Flow in a narrow gap along an enclosed rotating disk with through-flow," 1988.

[38] B.-C. Will, F.-K. Benra, and H.-J. Dohmen, "Investigation of the flow in the impeller side clearances of a centrifugal pump with volute casing," *Journal of Thermal Science*, vol. 21, no. 3, pp. 197–208, 2012.

[39] B.-C. Will and F.-K. Benra, "Investigation of the fluid flow in a rotor-stator cavity with inward through-flow," in *ASME 2009 Fluids Engineering Division Summer Meeting*, pp. 207–218, American Society of Mechanical Engineers, 2009.

[40] R. Spence and J. Amaral-Teixeira, "A cfd parametric study of geometrical variations on the pressure pulsations and performance characteristics of a centrifugal pump," *Computers & Fluids*, vol. 38, no. 6, pp. 1243–1257, 2009.

[41] I. B. Celik, U. Ghia, P. J. Roache, *et al.*, "Procedure for estimation and reporting of uncertainty due to discretization in {CFD} applications," *Journal of fluids {Engineering-Transactions} of the {ASME}*, vol. 130, no. 7, 2008.

[42] "Leibniz integral rule." `http://mathworld.wolfram.com/LeibnizIntegralRule.html`. Accessed: 2016-05-09.